HIERARCHICAL ZEOLITES: NOVEL SUPPORTS FOR HYDROCRACKING CATALYSTS

by

MONAMA WINNIE

DISSERTATION

Submitted in fulfilment of the requirements for the degree of

MASTER OF SCIENCE

in

CHEMISTRY

in the

FACULTY OF SCIENCE AND AGRICULTURE

(School of Physical and Mineral Sciences)

at the

UNIVERSITY OF LIMPOPO

SUPERVISOR: Prof. M. P. Mokhonoana

2016

DEDICATION

To my brother Bethuel Malose Monama and family.

DECLARATION

I declare that the dissertation hereby submitted to the University of Limpopo, for the degree of Master of Science in Chemistry has not previously been submitted by me for a degree at this or any other university; that it is my work in design and in execution, and that all material contained herein has been duly acknowledged.

…….. ……..

Monama, W. (Ms) **Date**

ACKNOWLEDGEMENTS

I humbly thank my supervisor, Prof. M. P. Mokhonoana, for giving me courage to pursue my MSc, his support, guidance and enduring patience during the course of this work. I would also like to thank the following people and institutions for every help they offered, without them it was going to be very difficult for this work to be completed successfully:

- Prof. R. Ryoo and his MSc. student, J. Changbum, for providing me with preliminary polyquaternary ammonium surfactants and the synthesis routes.
- The Geology department for XRD analysis.
- Mr T. N. Phahlaamohlaka at University of Witwatersrand Chemistry Department (Catomat) for BET surface area measurements.
- Dr. P. B. Ramatsetse at the University of Pretoria for SEM micrographs.
- The University of Cape Town and in particular the Department of Chemical Engineering for a warm welcome and allowing me to use their facilities during my one month visit to do the catalytic tests. Dr. R. Brosius for helping me carry-out the catalytic activity experiments.
- DST-NRF centre of excellence in catalysis (C*change) for financial support.
- Mr. N. M. Chauke for technical support.
- Dr. M. S. Thomas (HOD) for encouragement and support.
- The Chemistry Department at The University of Limpopo for offering me an opportunity to do a post-graduate degree at their institution.
- I would also like to thank my colleagues in the Inorganic Porous Materials Research Group for academic and social support.
- My family for the support and encouragement.
- Above all, I would like to thank God for the strength and endurance to complete this dissertation.

ABSTRACT

In this study, the use of synthetic hierarchical MFI zeolites as supports for palladium hydrocracking catalysts was investigated. Hierarchical zeolites were synthesised through two different routes, *viz*., (i) the indirect and (ii) direct routes. In (i) pristine ZSM-5 zeolites with different SiO_2/Al_2O_3 ratios (SARs) were synthesised hydrothermally using tetrapropylammonium bromide as structure-directing agent (SDA), followed by a brief desilication of its calcined form in 0.2 M NaOH solution at 65 °C for 0.5 h. Procedure (ii) involved prior synthesis of three polyquaternary ammonium surfactants (containing 2 - 4 ammonium centres), followed by their use as SDAs in the hydrothermal synthesis of hierarchical MFI zeolites. The resulting materials were characterised by XRD, FT-IR, SEM and N_2 adsorption isotherms (including BET surface area measurements). Successful synthesis of different classes of the hierarchical MFI zeolites was confirmed by XRD patterns, while successful synthesis of polyquaternary ammonium surfactants was confirmed by both their ^1H NMR spectra and their ability to direct the MFI structure. On the basis of IR, peak intensities in the OH region between 3500 and 3800 cm^{-1}, the surfactant-templated zeolites were inferred to be more acidic than zeolites prepared through the desilication route. Significant changes in crystal morphology were observed upon desilication of ZSM-5(50), while the ZSM-5(77) and ZSM-5(100) retained their agglomerated morphology upon a similar treatment. The micrograph pristine of ZSM-5(50) showed a predominant morphology of large and small spheroids, together with some ill-defined cubic shapes. After desilication, the zeolite did not retain the original morphology entirely, showing hexagonal prismatic crystals with twinning occurring in other areas and large spheroids “hatching” to reveal their contents upon treatment. Desilicated zeolites exhibited improved textural properties (*i.e*., increased S_{BET}, pore volumes and pore diameters) and minor structural readjustments compared to their pristine counterparts. Textural properties of surfactant-templated zeolites were superior to those of desilicated zeolites, and improved with increasing number of quaternary ammonium centres in the surfactant template. These materials were generally more crystalline than the conventional zeolites. Hydrocracking catalysts containing 0.9 wt.% Pd loading on different MFI supports were prepared by the incipient wetness impregnation method. The *n*-

hexadecane hydrocracking conditions used were typical of LTFT process (*i.e.,* Temperature = 215 - 310 °C, WHSV = 1 h^{-1}, Pressure = 20 bar, in addition to the H_2 /*n*-C_{16} ratio of 10). The catalytic activity in all catalyst systems increased with increasing reactor temperature and displayed C_4/C_{12} ratios ≠ 1, evidence of the occurrence of secondary cracking (*i.e*., a non-ideal hydrocracking behaviour). This was also supported by the shapes of their product distribution profiles, which showed dominant C_3 - C_7 *n*-paraffins. Co-feeding H_2O with *n*-C_{16} into the reactor was found to be detrimental to *n*-C_{16} conversion, but promoted the selectivity to *iso*-paraffins in the product spectrum. Simultaneous introduction of CO and H_2O aggravated secondary cracking. Amongst the pristine ZSM-5 zeolite-based catalysts, Pd/P-ZSM-5(77) showed the best catalytic performance. Upon desilication, the performance order changed to favour Pd/D-ZSM-5(50*). For the surfactant-templated supports, Pd/HSZ(N_4) showed the most superior hydrocracking performance. Comparison of catalytic activities of the best performing catalyst systems derived from the conventional and surfactant-templated zeolites in the hydrocracking of *n*-hexadecane, follow the order Pd/D-ZSM-5(50*) > Pd/P-ZSM-5(77) > Pd/HSZ(N_4). That is, the pristine and desilicated zeolite-based catalysts performed better than their surfactant-templated zeolite-based counterparts. Therefore, the post-synthesis generation of mesoporosity through desilicating ZSM-5 with a SAR of 50 has proven beneficial for the resulting catalyst system. One of the possible reasons for the relatively inferior hydrocracking performance of the Pd/HSZ(N_4) catalyst may be the aluminium-richness of the support (SAR = 40) compared to the conventional ZSM-5-based supports. In summary, catalysts Pd/D-ZSM-5(50*), Pd/P-ZSM-5(77) and Pd/HSZ(N_4) are promising for diesel-selective catalysis and need further refinements and exploration.

TABLE OF CONTENTS

LIST OF FIGURES

CHAPTER 2

CHAPTER 3

CHAPTER 4

LIST OF TABLES

Chapter 3

Chapter 4

LIST OF ABBREVIATIONS

BET	Brunauer-Emmett-Teller
S_{BET}	Brunauer-Emmett-Teller surface area
FAU	Faujasite
FT	Fischer-Tropsch
FTIR	Fourier-transform infrared
FTS	Fischer-Tropsch Synthesis
HTFT	High-Temperature Fischer-Tropsch
i-C_{16}	Isomerised hexadecane
IUPAC	International Union of Pure and Applied Chemistry
IWI	Incipient wetness impregnation
IZA	International zeolite association
LTA	Linde type A
LTFT	Low-Temperature Fischer-Tropsch
MCM	Mobil Composition of Matter
MFI	Mobil Five
n-C_{16}	*n*-hexadecane
SAR	Silica-to-alumina ratio
SDA	Structure-directing agent
SEM	Scanning electron microscopy
NH_3-TPD	Temperature-Programmed Desorption of ammonia
TEM	Transmission electron microscopy
TPA	Tetrapropylammonium

WHSV	Weight hourly space velocity
XLT	X-to-Liquids, with X = natural gas, biomass or coal
XRD	X-ray diffraction
ZSM	Zeolite Socony Mobil
^{1}H NMR	Proton nuclear magnetic resonance

CHAPTER 1

Introduction

1.1 Rationale of the study

A large amount (~ 60%) of the country's liquid fuels consumption is imported as crude oil for local refining [1]. The remainder is produced from coal by SASOL and from natural gas by PetroSA. Crude oil contains relatively high quantities of sulphur, nitrogen and aromatics, which produce unwanted emissions during combustion [1 - 5]. Transportation fuels such as diesel, whose demand continues to increase with the growing population, must meet lower limits on these contaminants. One of the major technologies currently producing high quality oil products (*i.e*., virtually free of sulphur, nitrogen and aromatics) operated in South Africa is the Fischer-Tropsch Synthesis (FTS) [4]. This technology is operated in the low- and high-temperature modes termed Low-Temperature Fischer-Tropsch (LTFT) and High-Temperature Fischer-Tropsch (HTFT), respectively [3, 4]. The LTFT process produces approximately 40% of diesel fuels and a large amount of low-value wax products (*i.e.,* a mixture of high molecular weight *n*-paraffins: C_{20} - C_{60}) [5]. These *n*-paraffin mixtures are excellent feedstocks for the hydrocracking process, which can produce high quality products that are less harmful to the environment. Combining the LTFT and hydrocracking units can produce up to 80% diesel fuels, which is double the yield produced by the LTFT unit alone [6].

The hydrocracking process has been developed to convert heavy feedstock to lighter transportation fuel products, using a bifunctional catalyst based on a noble metal supported on an acidic support [7]. Though there have been a variety of studies on the development of hydrocracking catalysts, incentives still exist to develop or optimise the catalysts for hydrocracking Fischer-Tropsch wax [8]. A hydrocracking

catalyst that uses microporous zeolites as acid supports for the processing of linear waxes would undesirably result in secondary cracking of products [9]. Hence, it is desirable to investigate whether the presence of mesopores, in addition to micropores, in hierarchical zeolites would increase the diffusivity of products (from metal to acid sites), while at the same time displaying ideal hydrocracking of the feed. Scherzer *et al.* [10] reported that it is important to have a rapid molecular transfer between the acid and metal sites to avoid secondary cracking reactions which produce short chain *n*-parrafins.

1.2 Research problem

This research is driven by the world's high demand for clean diesel fuels. Diesel fuels are traditionally produced by the fluidised catalytic cracking of the heavy fraction of petroleum. In recent years, a number of concerns have been raised in association with petroleum-derived fuels [2]. These include, among others, the following:

(i) high sulphur content, which is responsible for environmentally-unacceptable amounts of sulphur oxides during combustion,

(ii) unprecedented high price of crude oil, and

(iii) diminishing oil reserves.

Therefore, there is a global search for alternative sources of energy [2, 5, 6, 8]. The FTS is an alternative technology that is capable of producing ultra-low sulphur diesel (ULSD) fuels [5], though the process is poorly selective. A key element of the FTS is the development of active catalysts with high wax selectivity [2 - 9]. This project focuses on developing solid acid catalyst supports with hierarchical porosity in order to upgrade the Fischer-Tropsch (FT) waxes into clean transportation fuels through the hydrocracking process. The hydrocarbon *n*-hexadecane will be used as feedstock to model LTFT wax, because its hydrocracked product spectrum can easily be analysed by online gas chromatography.

1.3 Motivation

Fischer-Tropsch synthesis is a major part of XTL (X-to-Liquids, with X = natural gas, biomass or coal) technologies, which convert the syngas derived from each raw material (X) into hydrocarbon fuels (distillate fuels) [11]. The primary benefit of this technology is the production of high quality fuels (containing no aromatics, sulphur, and nitrogen or heavy metal contaminants). South Africa is currently holding a leadership position in the FT technology, which produces a large amount of wax amongst its product spectrum. The FT waxy products can selectively be hydrocracked to yield hydrocarbons in the diesel (C_{10}-C_{20}) or gasoline (C_5-C_{11}) range [12]. Therefore, this study explores hierarchical zeolites as supports for Pd catalysts for the beneficiation of the LTFT wax into value-added diesel fuels.

1.4 Aim and objectives

The aim of the study was to screen synthetic hierarchical Mobil Five (MFI) zeolites as potential catalyst supports in the diesel-selective hydrocracking of *n*-hexadecane as a model component of LTFT wax. The objectives of the study were to:

(i) synthesise polyquaternary ammonium surfactants and use them as organic structure-directing agents in the direct hydrothermal synthesis of hierarchical MFI-type zeolites, for comparison with hierarchical zeolites synthesised *via* alkaline desilication of pristine ZSM-5 zeolites,

(ii) characterise hierarchical zeolites using X-ray powder diffraction (XRD), Fourier-transform infrared spectroscopy (FTIR), scanning electron microscopy (SEM) and N_2 adsorption, including Brunauer-Emmett-Teller (BET) surface area measurements, and lastly

(iii) prepare hydrocracking catalysts by loading Pd onto the hierarchical zeolite supports *via* the incipient wetness impregnation (IWI) method, followed by evaluation of their catalytic efficiency in the hydrocracking of *n*-hexadecane as a model waxy feedstock.

1.5 Dissertation structure

This dissertation consists of five chapters, where the rationale for carrying out this study is given in Chapter 1. Chapter 2 includes a detailed review of the literature on relevant works and pertinent information required for this study. Chapter 3 presents the details of the methodology and experimental procedures on the synthesis of surfactant templates, supports, physicochemical characterisation, preparation of hydrocracking catalysts and the reactor studies. Chapter 4 presents and discusses the results obtained in this research. Note that the references are given per chapter to avoid repetitions and confusion. Lastly, the summary and conclusions drawn from this work are presented in Chapter 5 together with recommendations for future work.

1.6 References

[1] C. J. Cooper, Energy and transport issues for Gauteng, South Africa, *Journal of Energy in Southern Africa,* **18** (2007) 1 - 5.

[2] U. M. Teles, F. A. N. Fernandes, Hydrocracking of Fischer-Tropsch products, *Engenharia Térmica* (*Thermal Engineering*), **6** (2007) 14 - 18.

[3] T. N. Kalnes, Combination hydrocracking process for the production of ultra-low sulfur diesel, US Patent 7591940 B2, (2009).

[4] D. Leckel, M. Liwanga-Ehumbu, Diesel-selective hydrocracking of an iron-based Fischer-Tropsch wax fraction (C_{15} - C_{45}) using a MoO_3-modified noble metal catalyst, *Energy and Fuels*, **20** (2006) 2330 - 2336.

[5] G. Pölczmann, J. Valyon, J. Hancsók, Investigation of catalytic conversion of Fischer-Tropsch wax on Pt/AlSBA-15 and Pt/BETA zeolite catalysts, *Hungarian Journal of Industrial Chemistry Veszprém*, **39** (2011) 375 - 379.

[6] C. Bouchy, G. Hastoy, E. Guillon, J. A. Martens, Fischer-Tropsch waxes upgrading via hydrocracking and selective hydroisomerization, *Oil and Gas Science and Technology - Rev. IFP*, **64** (2009) 91 - 112.

[7] A. Halim, A-K Mohammed, K. K. Esgair, Fluid catalytic cracking of petroleum fraction (vacuum gas oil) to produce gasoline, *Iraqi Journal of Chemical and Petroleum Engineering*, **11** (2010) 33 - 45.

[8] P. Šimacek, D. Kubick, M. Pospišil, V. Rubaš, L. Hora, G. Šebor, Fischer–Tropsch product as a co-feed for refinery hydrocracking unit, *Fuel*, **105** (2013) 432 - 439.

[9] G. Pölczmann, Á. Szegedi, J. Valyon, A. Wollmann, J. Hancsók, Catalytic conversion of Fischer-Tropsch waxes, *Chemical Engineering Transactions,* **21** (2010) 1315 - 1320.

[10] Scherzer, J. Gruia, A., Hydrocracking Science and Technology, Chapter 3. Marcel Dekker Inc., New York, 1st edition (1996).

[11] A. Di Fronzo, Biomass to Liquid Process: New kind of cobalt and iron based catalysts for the Fischer-Tropsch Synthesis (Settori Scientifico Disciplinari: ING-IND/25; CHIM/04), PhD Thesis, The University of Milan, Italy (2012/2013).

[12] F. A. N. Fernandes, U. M. Teles, Modeling and optimization of Fischer-Tropsch products hydrocracking, *Fuel Processing Technology*, **88** (2007) 207 - 214.

CHAPTER 2

Literature Review

2.1 Petroleum-derived fuels

South Africa relies heavily (over 90%) on imported crude oil for liquid fuels production [1]. Its dependence on outside sources leaves it vulnerable to oil price shocks [2]. Oil prices have fluctuated with time, and the trend has been ever-increasing, leading to a high cost of liquid fuels. Fuel specifications caused by stringent government regulations promote replacement of blending conventional fuels with contaminant-free products (*i.e.*, fuels must comply with the environmental requirements) [3]. This has included banning the use of heavy metal additives to increase the octane number of petrol, and imposing tougher restrictions on the presence of sulphur or aromatics in distillate fuels such as diesel and jet fuels [4]. Crude oil is a complex mixture of materials consisting of hydrocarbons, as well as variable amounts of sulphur, nitrogen and oxygen [3, 5], which produce unwanted emissions during combustion. These noxious emissions place a strain not only on the refiner, but also research centres, catalyst manufacturers and process designers, who are required to design future technologies to convert and upgrade heavy feeds. Petroleum reserves are diminishing, and in view of the expected increase in global demand for clean transportation fuels, more rapid progress in alternative technologies is required [3]. Some of the new technologies include the transesterification process that uses oil, hydrogenation of bio-oils, biodiesel fuels and Fischer-Tropsch synthesis that uses syngas obtained by gasification of biomass [6]. The work in this dissertation focuses on the downstream processing of the well-known and established catalytic chemical process called Fischer-Tropsch synthesis [6, 7]. This technology is operated in South Africa at Sasol and PetroSA.

2.2 Fischer-Tropsch process for transportation fuels

2.2.1 History of the Fischer-Tropsch process

In the 1920s, Germany had virtually no petroleum reserves and relied on crude oil imports, though it possessed abundant coal reserves [8]. This drove many German scientists and engineers to invent and develop processes that enabled them to produce liquid fuels from their country's abundant coal. In 1923, two scientists, Franz Fischer and Hans Tropsch at Kaiser Wilhelm institute (*currently known as Max Planck Institute*), discovered a catalytic process capable of converting a mixture of carbon monoxide and hydrogen to hydrocarbons using an iron catalyst [9]. This process was named after them, *i.e*., the Fischer-Tropsch (FT) process. The process allowed Germany to alleviate the oil shortage during World War II, as it lacked access to sufficient crude oil [10]. However, after World War II, the vast oil fields of Arabia made it uneconomical for most free nations to pursue the technology [9].

The FT process was subsequently commercialised by South Africa's apartheid regime in the 1950s using coal as raw material to produce fuels [11, 12]. In 1955, the first large-scale plant (Known as Sasol I), went on-stream under the auspices of the South African Coal, Oil and Gas Corporation's (SASOL) at Sasolburg [12]. This plant is operated on fixed-bed Arge technology reactors, using a precipitated iron-based catalyst. To increase fuel production and off-set the country's increasing reliance on imported crude oil, two more plants were built in 1980 and 1982 (known as Sasol II and Sasol III) at Secunda [13]. Sasol II and Sasol III operated on circulating fluidised-bed (CFB) reactors. In 1992, two other FT plants were also built in South Africa (Mossgas plant, presently PetroSA in Mossel Bay) and Malaysia (Shell Bintulu plant) [14]. Other four FT plants include a joint venture between Sasol and ExxonMobil, Syntroleum, BP, Nigeria National Petroleum Company and Qatar petroleum [12, 14]. The FT process is now a well-established and developing technology in South Africa, and still finds more advances for the 21st century.

2.2.2 The FT process

The FT process is an industrial process in which high-quality liquid fuels are produced catalytically from synthesis gas or syngas (*i.e*., a mixture of CO and H_2) as

a feedstock [9, 12]. It consists of two main regimes, known as low-temperature Fischer-Tropsch (LTFT) and high-temperature Fischer-Tropsch (HTFT) [15]. The HTFT synthesis uses an iron-based catalyst at reaction temperatures ≥320 ºC and a pressure of 20 bar (*used by the two Sasol plants in Secunda, South Africa*), and is used for the production of gasoline and linear low molecular mass olefins [16]. On the other hand, LTFT synthesis uses a cobalt-based catalyst at reaction temperatures ≤250 ºC and produces middle distillates and essentially high molecular weight hydrocarbons, mostly waxes, for which product upgrading is required to obtain maximum efficiency of the overall process [16, 17].

A major challenge in the area of the FT process is selectivity [16 - 18]. The product distribution obtained from FTS follows a well-established Anderson-Schulz-Flory (ASF) model, irrespective of the process conditions used [19]. In this model, the FT reaction is modelled as an addition polymerisation reaction with the chain growth probability, α, which determines the hydrocarbon chain length distribution [20]. This ASF product distribution kinetic model is shown in equation 2.1:

$$M_n = (1 - \alpha)^2 \alpha^{n-1} \qquad (2.1),$$

where M_n is the mass fraction of the hydrocarbon with chain length n. Figure 2.1 shows a graphical representation of the FT product distributions as predicted by the ASF kinetic model.

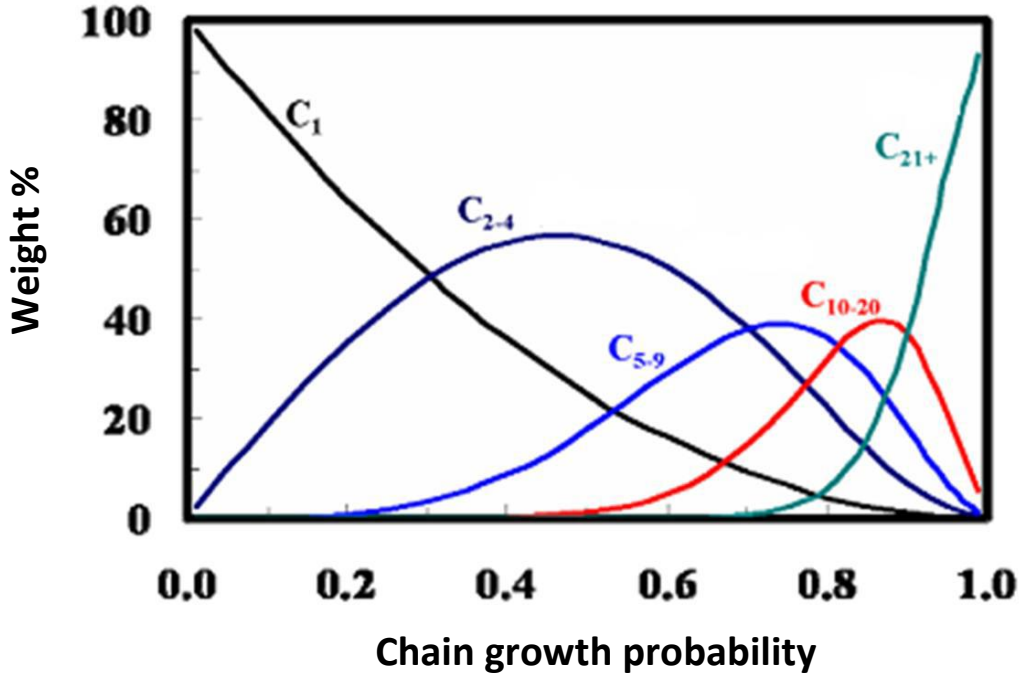

Figure 2.1 FTS product distribution as predicted by the ASF kinetic model [21].

As illustrated in Figure 2.1, the ASF kinetic model limits the amount of diesel fuels (C_{10} - C_{20}) that can be produced through straight-run FTS to approximately 40 wt.%. This is very low to be of realistic economic feasibility to meet the high demand of transportation fuels. It can be seen that when the α value approaches 1, a vast amount of wax is produced with high selectivity (>90 wt.%). In order to increase the liquid fuel production, the excessively-produced FT waxes can form the perfect feedstock to be hydrocracked into the required distillate fuel range using bifunctional catalysts (see Figure 2.2) [22]. Theoretically, if the production of heavy paraffins in the Fischer-Tropsch unit is integrated with an “ideal hydrocracking” unit, the production of up to 80% middle distillates could be achieved [23]. This makes the hydrocracking process a significant step to accompany the FT process. As an innovative step towards diesel-selective FTS, this project seeks to investigate zeolite-based hydrocracking catalysts in an attempt to beneficiate the LTFT wax into diesel fuels, by using *n*-hexadecane as model reactant. The overall FT process, incorporating downstream processes for value addition is illustrated in Figure 2.2.

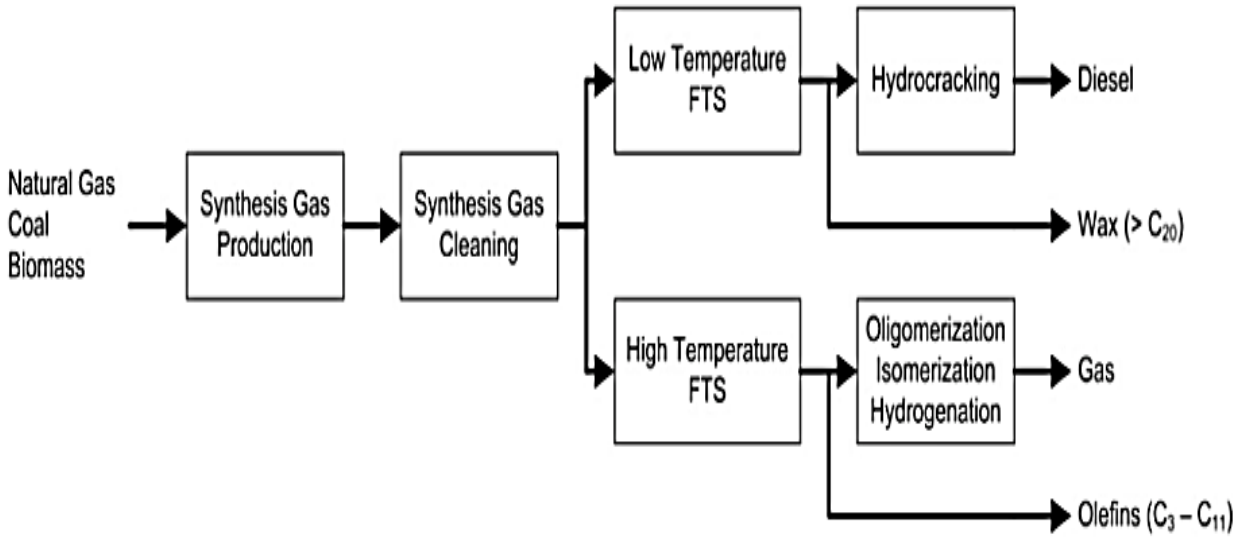

Figure 2.2 The overall process for production of liquid fuels by FT synthesis with downstream processes [24].

2.3 The hydrocracking process

Hydrocracking is an oil refinery process which has been developed to convert heavy oil fractions into lighter transportation fuel products [22 - 24]. It is accomplished by contacting a hydrocarbon feedstock with a bifunctional catalyst in an appropriate reactor vessel [25]. Suitable hydrocracking conditions include elevated temperatures (*e.g.,* 230 °C to 455 °C), elevated pressures (*e.g.,* 40 to 350 bar), and the presence of hydrogen [25]. Usually, the process is practised in a single reaction vessel or several reaction vessels in series utilising a single catalyst [26]. Hansen *et al.* [27] disclosed different types of reaction vessels that are used in carrying out the process. Most hydrocracking reactions are carried out in trickle-bed reactors, where the gas-liquid phase flow is concurrently downward through a fixed-bed of catalyst particles [28]. The downflow mode is the most commonly used in industrial practice due to its relatively low pressure-drop and also the absence of flooding [29]. A schematic representation of a trickle-bed reactor used in this project is shown elsewhere [30]. The mechanism of the hydrocracking reaction is outlined in Section 2.4, and the description of the hydrocracking catalyst will be discussed later in this chapter.

2.4 The hydrocracking mechanism

A number of mechanisms operating in the hydrocracking of *n*-paraffinic feedstocks have been reported in the literature [31, 32]. These mechanisms include the bifunctional mechanism, hydrogenolysis, thermal cracking, and the Haag-Dessau mechanism [32]. A brief description of each mechanism is as follows:

(i) Hydrogenolysis mechanism: This mechanism involves the carbon-carbon bond cleavage followed by hydrogenation of the fragments on the metal (*i.e., occurring on a monofunctional catalyst*).
(ii) Haag-Dessau mechanism: Involves the cracking of *n*-paraffins on the monofunctional acidic catalyst.
(iii) Thermal cracking: The mechanism occurs in the absence of a catalyst at high temperatures and high H_2 pressures. It proceeds through a chain reaction involving radicals as intermediates.
(iv) Bifunctional hydrocracking: This mechanism is based on the use of a bifunctional catalyst, comprising a noble metal and a Brønsted acid component.

Since this dissertation seeks to explore hierarchical zeolites as potential supports for Pd in the hydrocracking on *n*-hexadecane, the bifunctional hydrocracking mechanism is the most suitable and described below. This mechanism is the most widely-accepted in hydrocracking [32]. In this mechanism, the saturated hydrocarbons dehydrogenate on the metal sites into olefins, which subsequently diffuse to the Brønsted acid sites, where they are protonated to produce carbenium ion intermediates. The resulting carbenium ion then undergoes skeletal rearrangement to produce an alkylcarbenium ion, which undergoes a cracking reaction (at a bond β to the carbenium ion charge), with the consequent desorption of the hydrogenated product from the catalyst. This hydrocracking mechanism is schematically shown in the Scheme 2.1 for a representative hydrocarbon.

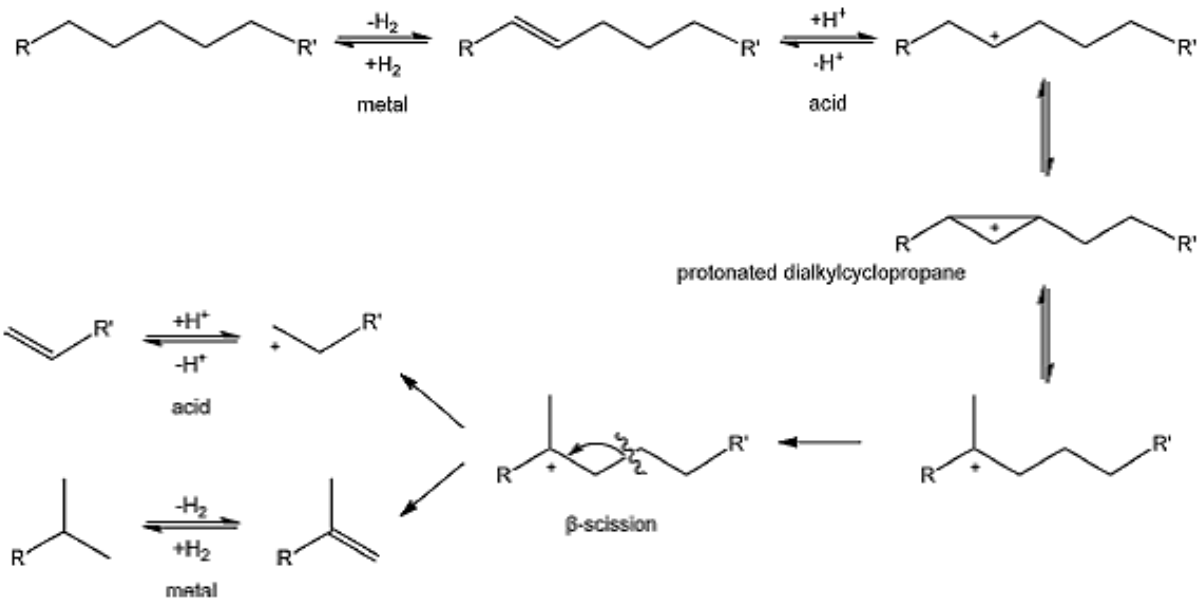

Scheme 2.1 Representation of a typical paraffin hydrocracking reaction mechanism over a bifunctional catalyst [33].

More mechanistic views of the ideal hydrocracking of long-chain *n*-alkanes, with their pertinent discussion, can be found in Weitkamp *et al.* [32]. This concept is further discussed in Section 2.5 below.

2.5 "Ideal" hydrocracking of paraffinic feedstocks

The term "ideal" hydrocracking is the term used to explain a situation where successive cracking of the primary cracked hydrocarbon products already present in the feedstock is minimised [34, 35]. In other words, only one cracking step takes place. The catalyst allows an alkene intermediate only one acid-catalysed transformation before the alkene is hydrogenated to an alkane [32]. This means that most primary cracked hydrocarbon products are rapidly hydrogenated and diffuse away to avoid successive (secondary) cracking of products [35]. The catalyst is then able to selectively convert the heavy paraffins into middle distillates [34]. Such hydrocracking behaviour is typified by a symmetric carbon number distribution around the average carbon number of the feed. Thybaut *et al*. [35] reported that the balance between the number and the strength of the metal and acid sites on the catalyst play a key role in the product selectivity. This means that the metal function should be strong enough to balance the acidic function in order to feed the acid sites with a maximal amount of intermediate alkenes to generate the carbenium ions and

quickly hydrogenate the cracked alkene intermediates [23, 35]. The key features of ideal hydrocracking of *n*-hexadecane as a feed are:

(i) only pure primary cracking is allowed,
(ii) there should be equal molar amounts of fragments between C_4 and C_{12} centred around C_8, and
(iii) no formation of C_1, C_2, C_{14} or C_{15} [23].

The shape of the product distribution curve can distinguish between "ideal" and "non-ideal" hydrocracking. Figure 2.3 shows the ideal and non-ideal product carbon number distribution obtained from the hydrocracking of *n*-hexadecane over Pt/CaY and Co-Mo-S/SiO_2-Al_2O_3 catalysts [23].

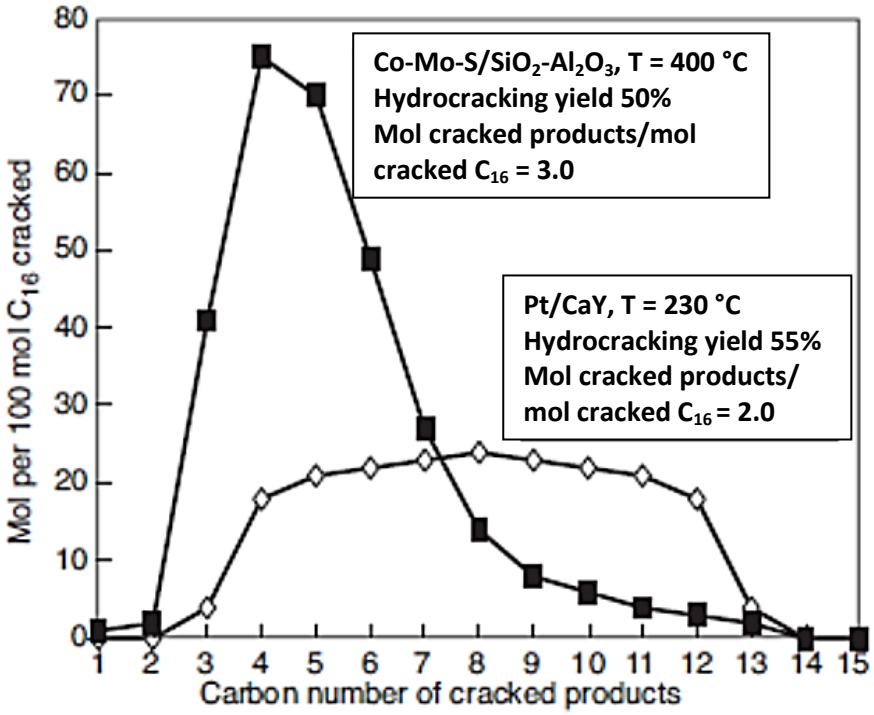

Figure 2.3 Molar carbon number distributions of *n*-C_{16} hydrocracking products over different catalysts at 50% conversion [23].

In ideal hydrocracking, the carbon number distribution of cracked products is symmetrical about C_8, revealing Gaussian type of distribution. This ideal hydrocracking behaviour is depicted over the Pt/CaY catalyst in Figure 2.3. On the other hand, the non-ideal behaviour is evidenced by the majority of cracked products being skewed to lighter hydrocarbons, thus peaking around C_4. The product

distribution for the non-ideal hydrocracking of *n*-C_{16} is illustrated over the Co-Mo-S/SiO_2-Al_2O_3 catalyst. This dissertation will use the C_4/C_{12} ratio criterion to deduce the ideal or non-ideal behaviour of the bifunctional catalyst, where the former will be defined by C_4/C_{12} ratio = 1 and the latter by C_4/C_{12} ratio ≠ 1 [30, 36]. Although ideal hydrocracking also requires appropriate hydrocracking conditions, the development of an ideal hydrocracking catalyst to achieve maximum diesel yields requires more attention [22]. In order to achieve ideal hydrocracking, the catalyst must have, among others, the following attributes:

(i) high activity at low hydrocracking reaction temperatures,
(ii) the production of high yields of *iso*-paraffins, and
(iii) the tendency of pure primary cracking, as well as exhibit a flat and symmetrical carbon number product distribution [23].

2.6 Hydrocracking catalyst

Morden hydrocracking processes are catalysed by bifunctional catalysts, consisting of a metal component supported on an acidic component [37 - 39]. These two compounds are discussed separately below.

2.6.1 The support component

The cracking function of the hydrocracking catalyst is provided by the acidic support of the Brønsted type [39]. Generally, strong acidity favours cracking, while moderate acidity shows higher selectivity for isomerisation [40]. Different kinds of acidic supports have been used to formulate hydrocracking catalysts. These include:

(i) amorphous oxides, *e.g.*, silica-alumina,
(ii) crystalline zeolites, mostly ultra-stable Y-zeolites (USY), ZSM-5 and a binder, *e.g.*, alumina, or
(iii) hybrid supports consisting of a mixture of zeolite and amorphous oxides [41].

The above-mentioned classes of supports are essentially microporous in the context of the IUPAC classification (*see section 2.6.1.1*). It would therefore be a relevant scientific endeavour to explore potential supports in the larger-pore regime. Other factors to consider in identifying a hydrocracking catalyst support are (hydro)thermal stability and BET surface area [40, 41]. In line with the quest to explore larger-pore

supports, this research considers support materials containing a combination of micro- and meso-pores.

2.6.1.1 Zeolite-based hydrocracking supports

In the field of heterogeneous catalysis, zeolites occupy more than 40% of the entire solid catalysts [42]. This is based on their catalytic properties related to their physicochemical properties such as acidity, topology, morphology, chemical composition, surface area, the ability to separate reactants from products, and high adsorption capacity [43]. According to the International Union of Pure and Applied Chemistry, porous materials are classified into three types, namely, microporous (<2 nm), mesoporous (2 - 50 nm) and macroporous (> 50 nm) [44]. Zeolites are defined as crystalline microporous aluminosilicates, whose structures consist of a regular array of uniform pores with molecular dimensions [44]. They were first discovered in 1756 by the Swedish mineralogist, Axel Fredrik Cronstedt, upon observation that a natural mineral, stilbite, visibly lost water when heated in a blow-pipe [45, 46]. The first zeolites to be commercialised were A (LTA), X and Y (FAU), for applications as desiccants and for gas drying [47]. A widely used MFI-type zeolite, ZSM-5 (Zeolite Socony Mobil-5), was discovered by Landolt and Argauer (Mobil Oil Company) in 1972 [48], and has since developed a reputation as an industrial catalyst in processes involving the transformation of hydrocarbons.

Constrained pore sizes of zeolites impose diffusion limitations in catalytic applications [49]. The diffusion limitations associated with zeolites led many researchers to design materials with larger pore dimensions, *i.e.*, pore diameters >2 nm [50]. Advances in the search for larger pore zeolites led researchers at Mobil Oil Corporation to the discovery of mesoporous materials, when they discovered a family of silicate/aluminosilicate materials with exceptionally large and uniform pore structures [50, 51]. This family is designated M41S, and its members are MCM-41, MCM-48 and MCM-50. Some mesoporous materials such as MCM-41 and SBA-15 with good mass transfer have been explored in catalytic applications [51, 52]. However, due to their amorphous character, poor hydrothermal stability and low acidity, these materials have limited catalytic applications [53]. In hydrocracking, supports such as MCM-41 and SAPO-34 showed potential to favour hydroisomerisation reactions over cracking [54]. On the other hand, zeolites offer

advantages compared to amorphous supports due to their well-defined pore structure and high density of acid sites, which result in higher hydrocracking activity [55]. As a result, much research effort is still dedicated to the development of zeolite-based hydrocracking catalyst and the work presented in this dissertation marks a contribution to this development by using hierarchical zeolite catalyst supports. Section 2.6.1.2 describes the general structure and composition of zeolites, a class of materials with potential as supports in hydrocracking catalysts.

2.6.1.2 Structure and composition of zeolites

The primary building units of zeolites are $[SiO_4]^{4-}$ and $[AlO_4]^{5-}$ tetrahedra, which link together to produce secondary building units [46, 56]. This linking of adjacent tetrahedra takes place through the sharing of corners *via* common oxygen atoms [46]. Lowenstein's rule precludes that two adjacent tetrahedra contain aluminium in tetrahedral positions, *i.e*., Al-O-Al linkages are forbidden, while Si-O-Si are allowed [57]. When the oxygen atom is connected to a tetravalent silicon atom and a trivalent aluminium atom, an exchangeable counter-cation needs to be present to compensate the net negative charge of the tetrahedron (resulting from the anionic aluminium) (Figure 2.4) [58]. If the counter-cation is a proton (H^+), strong Brønsted acidic properties are induced. Figure 2.4 shows links between the TO_4 (T = Al or Si) tetrahedra through one oxygen atom.

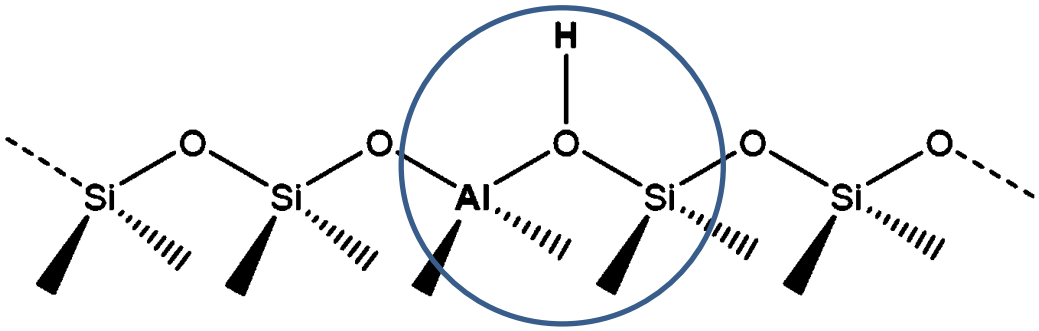

Figure 2.4 The representative chain structure of a zeolite in the H-form [58].

The Na-form zeolite is normally ion-exchanged with ammonium salts to first generate the NH_4^+-form, and subsequently calcined to produce the H-from, *i.e*., the Brønsted acidic form [58]. Of importance are the acid properties of zeolites, which make them useful in acid catalysis. In catalytic reactions, activity and selectivity depend on the number of acid sites available in the zeolite [34, 35]. For instance, in the

hydrocracking reactions, the metal-to-acid sites balance play a key role in achieving an ideal hydrocracking catalyst. Giannetto *et al.* [59] has also revealed the role of zeolite acidity in the hydrocracking and hydroisomerisation of *n*-heptane over Pt/H-Y zeolites, wherein they observed lower activity at a higher SiO_2/Al_2O_3 ratio (SAR). Interestingly, the measure of acidity in zeolites can be controlled by fine-tuning the SAR [44].

Figure 2.5 shows how secondary building units are linked together to produce the ZSM-5 zeolite structure.

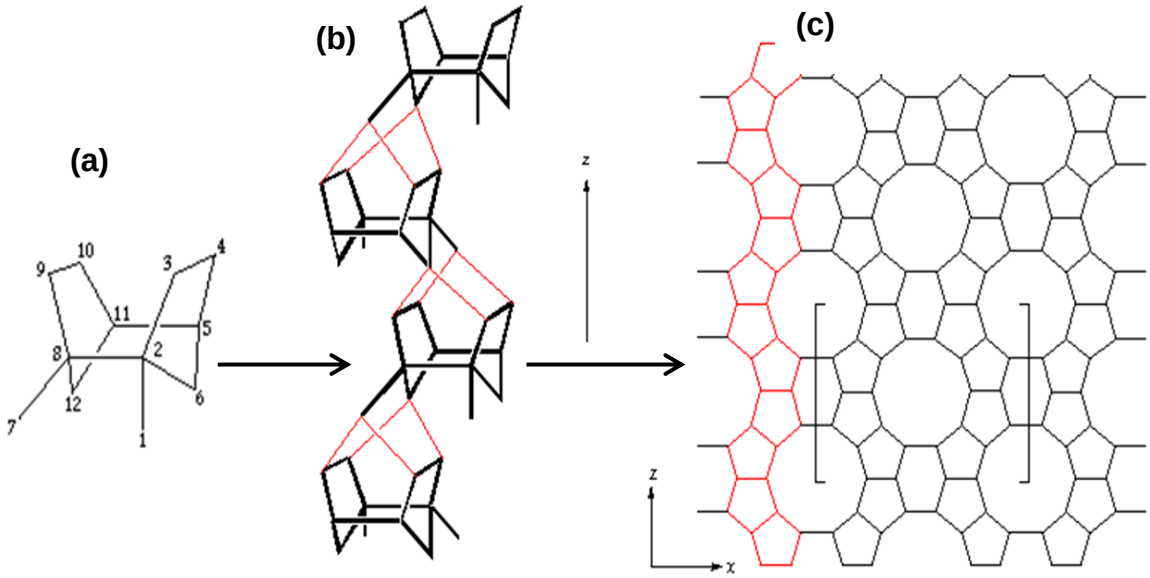

Figure 2.5 Structure of ZSM-5 zeolite composed of pentasil units [57].

The ZSM-5 zeolite structure is built from pentasil secondary building units. These individual pentasil units (a) combine to form long chains (b) which then join together to form ZSM-5 layers (c). There are over 40 natural zeolites and 213 synthetic zeolites, as reported by the structure commission of International Zeolite Association (IZA) [60]. Each zeolite has its unique structure. Since both micropores and mesopores are involved in support materials selected for this study, the next sections will give a brief account of each porosity regime.

2.6.1.3 General synthesis of microporous zeolite

Zeolite synthesis occurs *via* a hydrothermal process using reagents such as silica source, an alumina source, a mineralising agent and quaternary ammonium salts as structure-directing templates [61 - 65]. These reagents are mixed to form a gel. The

sequence of mixing these reagents to obtain a synthesis gel is carefully controlled to give the desired zeolite [62]. Also, synthesis parameters such as reaction temperature, stirring, gel pH, and crystallisation period are carefully considered for a specific zeolite [64]. The resulting synthesis gel is usually heated in a sealed autoclave at temperatures above 100 °C [63]. The uniqueness of the zeolites is characterised by the type of templates used since the zeolite structure appears to form around them [65]. In the case of a ZSM-5 zeolite, the tetrapropylammonium cation is commonly used as template since it promotes the synthesis of MFI topology over a wide range of compositions, and is also entrapped in the channels of the zeolite. [66]. Templates can be removed from the structure, usually by calcination at elevated temperatures around 500 °C, to produce the open-pore materials for use in sorption and catalysis. Figure 2.6 summarises general steps followed for the synthesis of ZSM-5 [66].

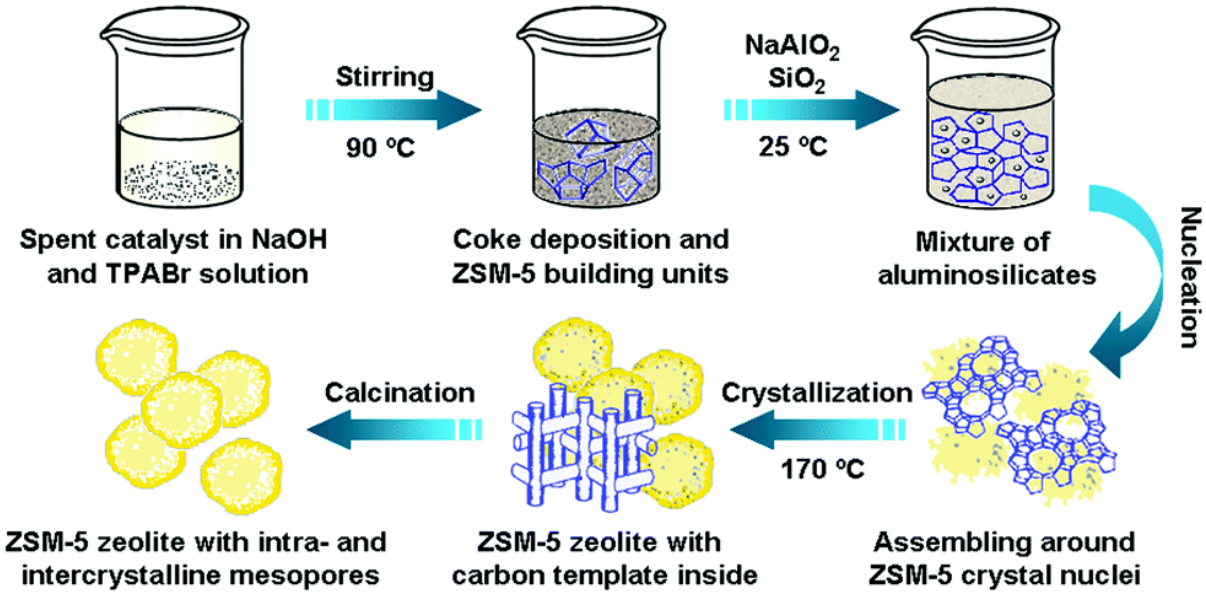

Figure 2.6 Typical steps proposed for the hydrothermal synthesis procedure of ZSM-5 [66].

This dissertation contributes to the development of the MFI-type zeolite supports by incorporating both micropores and mesopores in systems referred to hierarchical structures.

2.6.2 Hierarchically-structured zeolites

Improved performance of zeolite catalysts can be envisioned by enhanced accessibility to the active sites in the micropores [67, 68]. To alleviate diffusion

limitations in catalytic reactions, a possible method is to introduce interconnected larger pores in the zeolite structure, generating “hierarchical zeolites” [67 - 70]. Hierarchical zeolites have a bimodal distribution of pores, where the micropores provide a shape-selective catalytic process for guest molecules, while the mesopores provide a facile diffusion pathway to and from catalytic sites in the zeolitic pores [71]. The use of hierarchical zeolites as catalysts in various reactions has demonstrated their large potential and interesting catalytic properties [69]. They are of interest in petroleum refining processes since conventional zeolite catalysts cannot refine about 20% of petroleum due to the steric hindrance posed by bulky molecules [70, 71]. They have been tested in reactions involving aldol condensations of benzaldehyde, esterification of benzyl alcohol with hexanoic acid and Friedel-Crafts acylation of aromatic compounds [71]. In the hydrocracking reactions, hierarchical zeolites have also found great potential as catalyst supports. Christensen *et al.* [72] observed a significant increase in activity in *n*-hexadecane cracking over a mesoporous ZSM-5 material (52%) than that of conventional ZSM-5 (17%). Also, a fourfold increase in *iso*-paraffins over the “mesoporous ZSM-5” was obtained. Zhu *et al.* [73] explained that the shorter the retention time of the substrates in the zeolite crystals with mesoporosity, the lesser the secondary cracking and the more the isomerisation activity. This dissertation aims to explore MFI-type hierarchical zeolites as supports for Pd in the hydrocracking of *n*-hexadecane.

Several synthesis approaches to produce zeolites with enhanced transport properties are reported in the literature [67, 74 - 76]. These approaches can be classified into three groups, *viz*., the synthesis of non-hierarchically structured zeolites, preparation of hierarchically-structured single-phase mesoporous zeolites and synthesis of hierarchically-structured zeolite composites [75]. Figure 2.7 summarises these different approaches.

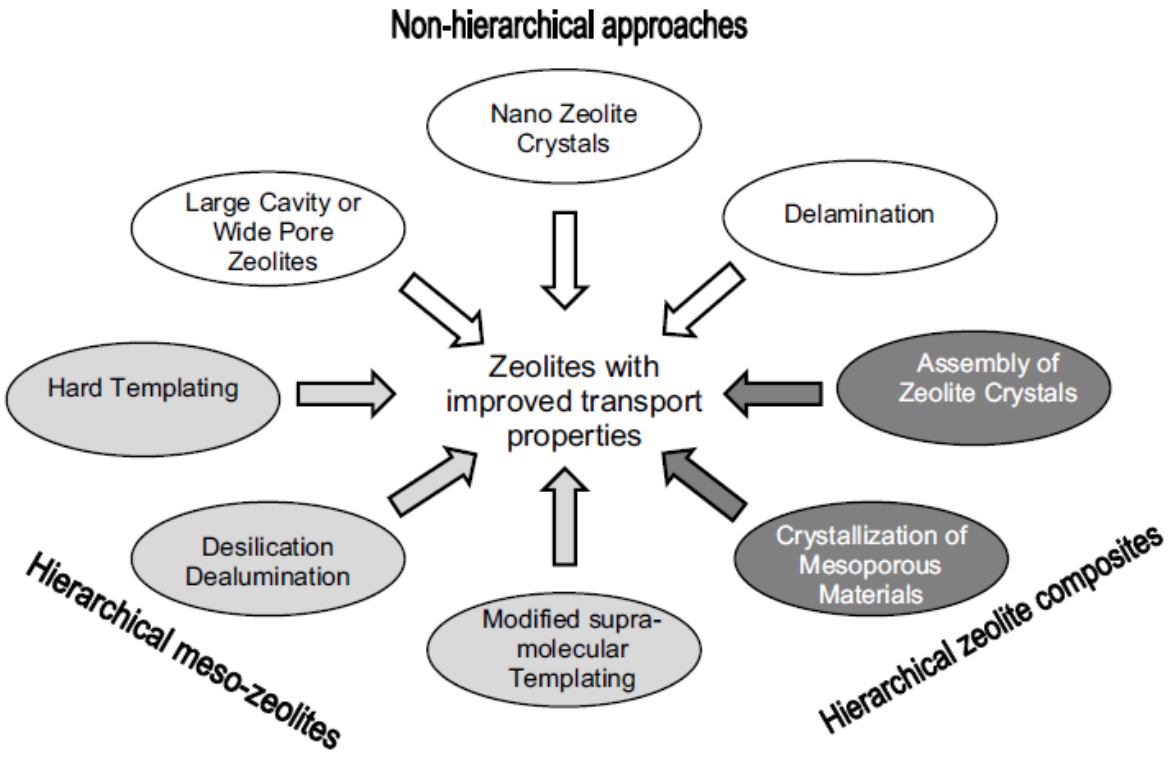

Figure 2.7 Various synthesis approaches to zeolites with improved transport properties [75].

This dissertation focuses particularly on the synthesis of hierarchical zeolites through desilication and dual-functional surfactant approach, both of which fall under the hierarchical meso-zeolites class in the above figure. Therefore, a description of these two preparation methods is given in sections below.

2.6.2.1 Desilication approach

One of the approaches of generating mesopores through post-synthesis treatment is the desilication of a conventional zeolite framework by treatment with an aqueous alkaline solution [77 - 80]. This method was first reported in the open literature in 1992, when it was shown that alkaline treatment of conventional zeolite crystals resulted in the selective extraction of Si from the framework [78]. The desilication method can be used effectively to produce mesoporous zeolite crystals when the Si/Al ratio of the starting material is in a certain range (see Figure 2.7) [79, 80]. An optimal Si/Al range of 25 - 50 has been found to lead to a well-controlled mesopore formation. When the Si/Al ratio of the pristine zeolite is higher (*i.e.*, > 50), excessive Si extraction takes place and result in formation of large pores [81]. Groen *et al*. [82] demonstrated the role of aluminium as a pore-directing agent in the hierarchical porosity development in MFI zeolites by desilication. Through their research, the

framework aluminium was found to control the process of framework silicon extraction and to make desilication selective towards intracrystalline mesopore formation. An important finding in this area is that template-containing (uncalcined) zeolites are practically inert to Si extraction [82]. Successful production of hierarchical porous zeolites can be achieved by variation of the time and temperature of the alkaline treatment [83 - 86]. Highly concentrated alkaline media and prolonged treatment on MFI zeolites destroy the zeolite structure [84]. However, to control the process of mesopore formation in the zeolite, mild conditions are required, *i.e*., low concentrations of the base and short contact times (*e.g., concentrations < 0.5 M NaOH solution and contact times < 1 h*) [82]. Groen *et al*. [84] have established the optimal desilication of ZSM-5 to be achieved in 0.5 h using 0.2 M NaOH at a temperature of 65 ºC. Figure 2.8 shows how the Si/Al ratio dictates the formation of mesopores in the zeolite.

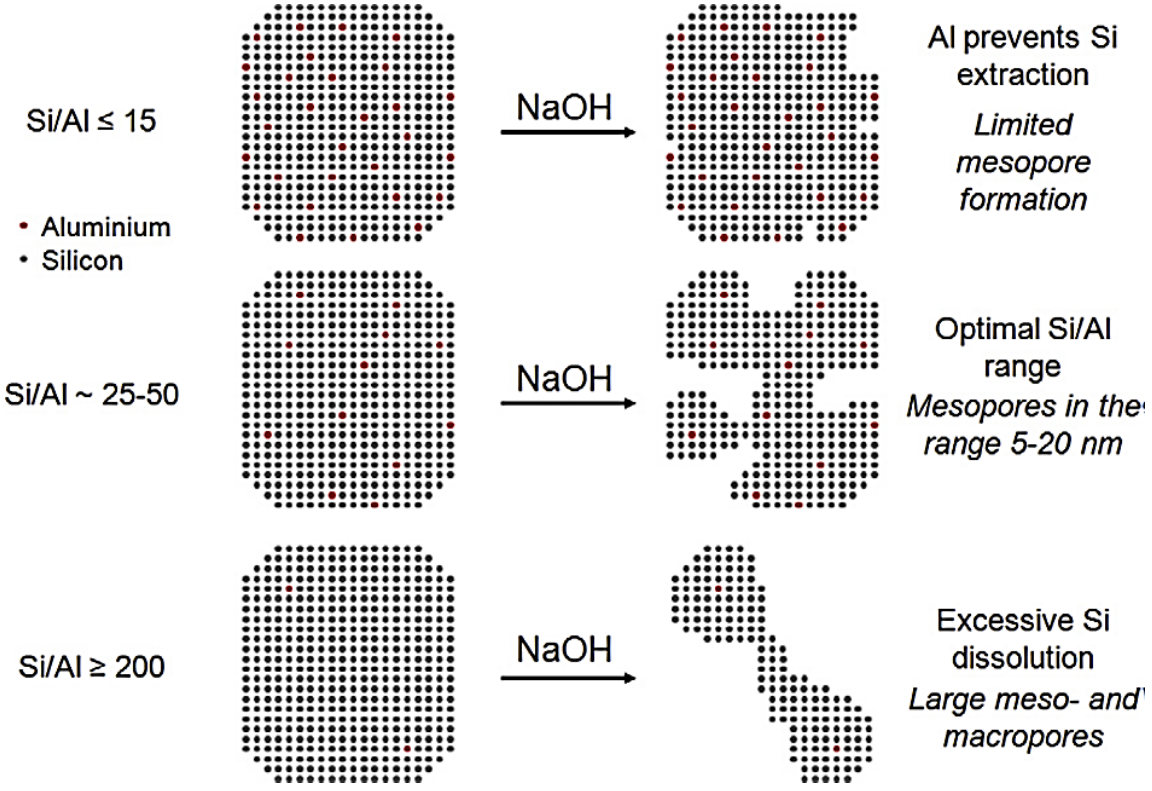

Figure 2.8 Schematic representation of MFI desilication by NaOH treatment, how Si/Al ratio dictates the formation of mesopore sizes [68].

It is evident that hierarchically-structured MFI zeolites can be optimally produced when the Si/Al ratio of the pristine zeolite lies in the range 25 - 50 (Figure 2.7). Therefore, this dissertation will explore pristine ZSM-5 zeolites with Si/Al ratios in the

range 25 - 50, or equivalently SiO_2/Al_2O_3 ratios in the range 50 - 100 (*see Chapter 3 and beyond*) and their subsequent desilication, using the reported optimal conditions [84], to generate hierarchically-structured derivatives.

2.6.2.2 Polyquaternary ammonium surfactant-templated approach

Since the development of MCM-41, the focus of many researchers shifted towards the design of surfactant templates that can simultaneously generate MCM-41-like mesopores and zeolite-like microporous walls in a direct-synthesis route [52, 68, 87 - 90]. This has recently led to significant progress in the synthesis of zeolites with ordered mesopores by using soft templates strategy. Ryoo's group [67, 68] designed a few kinds of surfactants which are composed of a zeolite structure-directing functionality covalently joined to a hydrophobic alkyl tail, *i.e.,* mesopore generating functionality. Kim *et al.* [80] also reported on the syntheses of organic surfactants, as well as their use in tailoring zeolite structures into hierarchically nanoporous architectures and zeolite nanosheets. Figure 2.9 shows the molecular structures of the different bifunctional cationic surfactants produced [90].

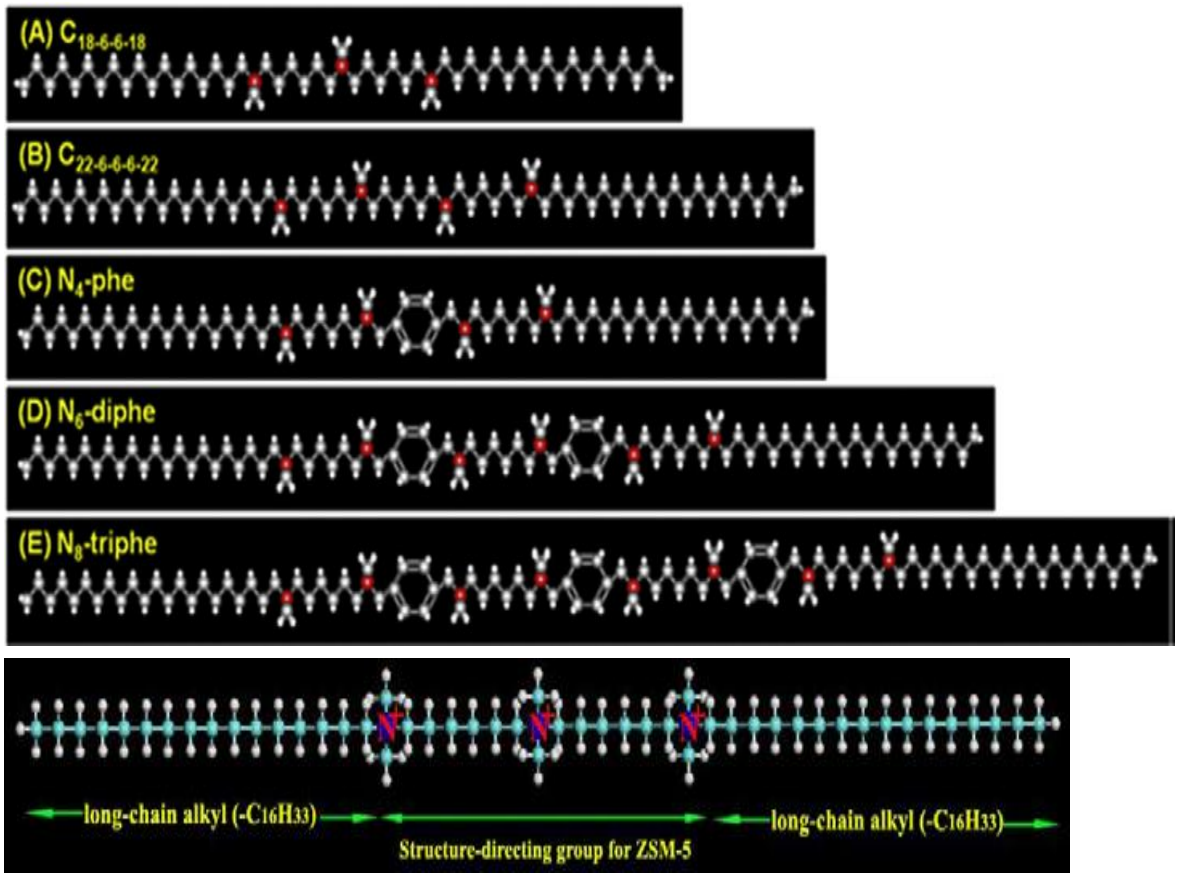

Figure 2.9 Molecular structures of different bifunctional cationic surfactants [90].

During hydrothermal synthesis, the head-group (quaternary ammonium) of the surfactant becomes the “zeolite-directing” functionality, while the long-chain alkyl tail assembles into a micelle, directing the structure to a specific meso-range [87, 90]. These types of surfactants have a zeolite-directing head-group composed of 2 or more quaternary ammonium centres connected with alkyl spacers and two hydrophobic tails. The spacers are adjustable polymethylene units which allow flexibility in the relative position and distance of quaternary ammonium head-groups from each other [91]. This is unlike the supramolecular templating mechanism of the formation of MCM-41, which uses cetyltrimethylammonium bromide as a porogen to synthesise ordered mesoporous materials [87, 88]. As opposed to traditional templates used for the synthesis of zeolites, these polyquaternary ammonium surfactants are not commercially available and need to be synthesised prior to their use as structure-directing agents (SDAs).

2.6.3 The metal component of the hydrocracking catalyst

There are various metals used as the hydrogenation functionality in the hydrocracking of *n*-paraffins. They include noble metals (*e.g*., palladium and platinum), or non-noble metal sulphides from Group VIB (*e.g*., molybdenum, tungsten) and Group VIIIB (*e.g*., cobalt and nickel) [92, 93]. The non-noble metal sulphides are resistant to sulphur and nitrogen compounds and are mostly used in the hydrocracking of heavy fractions from crude oil [94]. On the other hand, FT waxes do not contain sulphur or nitrogen compounds and noble metals are used as catalysts for their processing. In the literature, it has been reported that hydrogenation strength of the different classes of metals in the hydrocracking of *n*-paraffins decreases in the order: noble metals > sulphided transition metals > sulphided noble metals [94]. The use of noble metals is also reported to be promising catalytic components essential in the hydrocracking of LTFT wax, while non-noble metal hydrocracking catalysts display less or no activity below 350 °C [37, 94]. In general, the noble metal content of the hydrocracking catalysts is usually 1 wt.% or less, while for non-noble metals *(e.g.,* Co and Ni) it is 3 - 8 wt.% and 10 - 30 wt.% for Mo and W [94, 95]. The low loading of the noble metal-based catalysts is informed by the high cost of the metals.

2.6.4 Hydrocracking catalyst preparation

There are a number of methods used to prepare hydrocracking catalysts, *viz*., ion exchange, homogeneous deposition-precipitation, grafting and impregnation [96]. The preferred and most reported method to prepare bifunctional catalysts is the incipient wetness impregnation (IWI) [95]. This method provides a uniform metal dispersion on the support. In the method, the metal active phase is added in a solution to the dry powdered support in a controlled addition manner (until it is incipient wet, *i.e*., contains just enough solvent to fill the pores) [96]. The pore volume and surface area of the support determine the volume of the solution that can be adsorbed. The metal precursor needs to have a high solubility in the solvent and at the same time provide diffusion in the pores of the support. The resulting catalyst is allowed to dry and then calcined to drive off any volatile components and to stabilise the metal on the support [97 - 100].

2.7 Catalyst deactivation

Catalytic reactions involving the transformation of organic compounds over solid catalysts always form heavy side products, either in the pores, on the outer surface or in both locations of the catalyst [101 - 103]. The formation of these non-desorbable products is the most frequent cause of catalyst deactivation in industrial processes [102, 103]. Coke is a generic name for a mixture of heavy, strongly adsorbed organic side products formed on the surface of solid catalysts during organic catalytic reactions [104]. It consists of a large number of non-volatile, low-boiling point and low hydrogen-content components [101, 104]. Due to the potential for the combination of the FT synthesis and hydrocracking, this dissertation will investigate hydrocracking under conditions relevant to LTFT, including catalytic behaviour in the presence of CO and H_2O. Some poisoning or evidence of deactivation through these complex reactions will be explored.

The effect of CO on the hydrocracking catalyst has been reported to be detrimental to selectivity, resulting in extensive secondary cracking [31, 32]. This is based on fact that CO adsorption limits the supply of activated hydrogen to the acid sites, resulting in both reduced adsorption of the feed paraffins as carbenium ions on the acid sites, and saturation of the cracking fragments prior to desorption from the acid sites [101]. Also, the co-feeding of H_2O into the reactor has been shown to either activate or deactivate the hydrocracking catalyst, depending on the type of catalyst [104, 105]. Yan [106] demonstrated that the addition of water is beneficial for Pd/REX catalysts, but detrimental to Pt/HY catalysts in the hydrocracking of blend gas oils.

2.8 Characterisation of zeolites

Once the synthetic zeolite-related materials are produced, they are characterised by physicochemical methods to determine if they have the desired properties [107]. Important properties of zeolites are structure, crystallinity, morphology, pore size/volume, surface area, acidity, *etc*. Typical physicochemical characterisation techniques used to study zeolites and related materials are briefly described below.

2.8.1 X-ray powder diffraction (XRD)

X-ray powder diffraction is used as a routine characterisation technique to verify the identity and purity of the phase(s) present in zeolitic materials. After synthesis, the XRD pattern of the anticipated material is compared with a reference diffraction pattern. Crystallite sizes can be estimated using the Scherrer analysis and the relative % crystallinity can be determined from intensities of the characteristic peaks [108 - 110]. In this dissertation, X-ray powder diffraction was used to confirm the MFI framework structure of the zeolitic samples and determine their crystallinity and crystallites sizes.

2.8.2 Fourier-transform infrared (FTIR) spectroscopy

Zeolite acidity and framework vibrational bands can be characterised by using the FTIR spectroscopy. The IR framework vibrational region of zeolites is situated in the region 400 - 1200 cm^{-1}. Also, vibrational modes of surface hydroxyl groups can also be detected in the region 3800 - 2500 cm^{-1} [111,112]. The FTIR analysis performed in this dissertation was without the use of probe molecules. This allowed Brønsted acidity in these materials to be qualitatively rationalised based on the appearance of the hydroxyl peaks.

2.8.3 Temperature-programmed desorption of ammonia (NH_3-TPD)

The acidity of zeolites can also be effectively analysed by using NH_3-TPD. This method involves interacting the zeolite with gaseous NH_3 at a specific temperature. The resulting NH_3 desorption profile as a function of temperature provides information about acid strength distribution. Weak acidity corresponds to low NH_3 desorption temperatures, whereas strong acidity corresponds to high NH_3 desorption temperatures. The acid site strength distribution on the resulting TPD profile can therefore be categorised as:

(i) Weak : <200 °C,
(ii) Medium : 200 - 400 °C, and
(iii) Strong : >400 °C [113, 114].

However, this technique was not used in this study.

2.8.4 Scanning electron microscopy (SEM) and transmission electron microscopy (TEM)

Electron microscopic imaging of the individual crystals of a mesoporous zeolite material reveals more information about the morphology of the sample. In particular, TEM is used to study the porosity of zeolites and provides a direct and visual image of the individual crystals, while SEM provides morphological information (appearance, size and shape) of the individual zeolite crystals [115, 116]. Only SEM was accessible to study zeolitic materials in this dissertation.

2.8.5 N_2 adsorption isotherms and BET surface are measurements

Physisorption measurements are typically conducted using N_2 as adsorbate to probe the pore characteristics of porous materials. The measurements reveal information about the textural properties of porous materials (both microporous and mesoporous), which include surface areas, pore volumes and pore diameters. The IUPAC classification of adsorption isotherms for different porous materials is presented in Figure 2.10 [117].

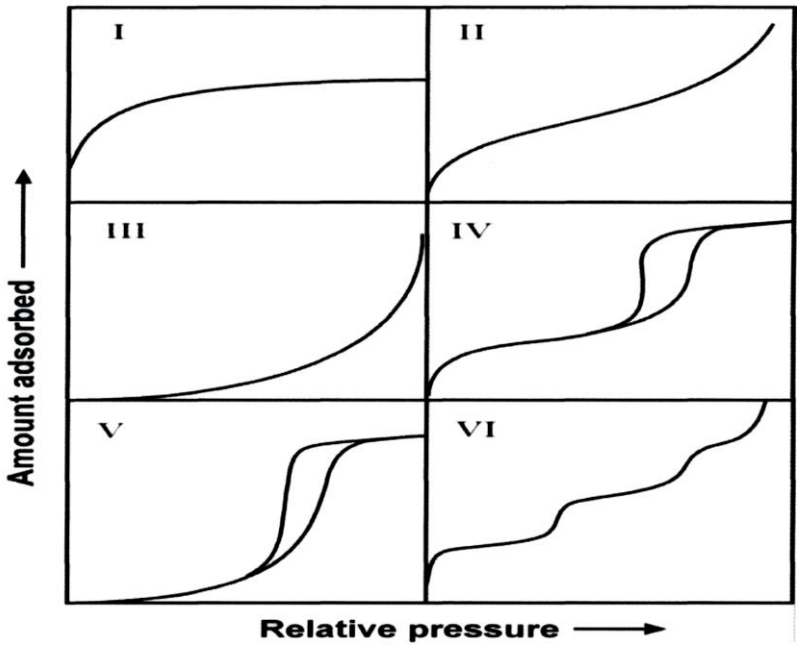

Figure 2.10 The IUPAC classification for adsorption isotherms [117].

The shape of the adsorption isotherm depends on the porous texture of the solid material. Only four of the six types of isotherms shown in Figure 2.10 are usually found in catalyst characterisation. A Type I adsorption isotherm characterises

microporous adsorbents, where adsorption takes place at very low relative pressures (P/P_o), and exhibit a plateau at higher P/P_o. Type II, III and VI are usually for macroporous solids, while Type IV and V correspond to mesoporous adsorbents. The BET analysis provides the specific surface area, in m^2/g, from N_2 adsorption measured as a function of P/P_o [117 - 119]. This technique was used to determine the surface areas of the MFI-type materials prepared in this dissertation. Also, the nitrogen adsorption isotherms were plotted and the shape of the isotherm helped to confirm the porous nature of the zeolite-based materials used.

2.9 References

[1] J. C. Nkomo, Energy security and liquid fuels in South Africa, *Journal of Energy in Southern Africa,* **20** (2009) 20 - 24.

[2] J. C. Nkomo, Crude oil price hikes and issues for energy security for Southern Africa, *Journal of Energy in Southern Africa,* **21** (2010) 12 - 16.

[3] D. Duissenov, Production and processing of sour crude and natural gas challenges due to increasing stringent regulations, MSc. Thesis, Norwegian University of Science and Technology, Norway (2013).

[4] J. G. Speight, Heavy Oil Production Processes, Elsevier, New York, (2013) 4 - 5.

[5] W. R. Niessen, Combustion and incineration processes, *Third Edition, Revised and Expanded,* Marcel Dekker, New York, (2002) 106 - 108.

[6] A. M. Ahmed-Alsobaai, Development of NiW-Zeolite-based catalysts for hydrocracking of gas oil: Synthesis, Characterization, activity and kinetics studies, PhD Thesis, Universiti Sains Malaysia, Malaysia (2007).

[7] Alternative Transport Fuels - Courtesy of AIP, *World Petroleum Council*, *www.world-petroleum.org*, (2009), Accessed 02/02/2015.

[8] A. N. Stranges, Germany's synthetic fuel industry *1927 - 1945, Energeia,* **12** (2001) 1 - 6.

[9] H. Schulz, Short history and present trends of Fischer-Tropsch synthesis, *Applied Catalysis A: General*, **186** (1999) 3 - 12.

[10] J. L. Casci, C. M. Loka, M. D. Shannon, Fischer-Tropsch catalysis: The basis for an emerging industry with origins in the early 20th Century, *Catalysis Today*, **145** (2009) 38 - 44.

[11] T. majozi, P. Veldhuizen, The chemicals South Africa, *American Institute of Chemical Engineers*, (2015) 46 - 51.

[12] M. E. Dry, Sasol route to fuels, **12** (1982) 744 - 750.

[13] E. van Steen, M. Claeys, Fischer-Tropsch Catalysts for the Biomass-to-Liquid (BTL)-Process, *Chemical Engineering and Technology,* **31** (2008) 655 - 656

[14] A. de Klerk, Fischer-Tropsch refining, PhD Thesis, University of Pretoria, South Africa (2008).

[15] E. F. Sousa-Aguiar, F. B. Noronhac, A. Faro Jr., The main catalytic challenges in GTL (gas-to-liquids) processes, *Catalysis Science and Technology*, **1** (2011) 698 - 713.

[16] S. Kresnyak, Enhancement of Fischer-Tropsch process for hydrocarbon fuel formulation in a GTL environment, WO 2013166583 A1 (2013).

[17] A. H. Choudhury, V. S. Moholkar, Synthesis of liquid hydrocarbons by Fischer–Tropsch process using industrial iron catalyst, *International Journal of Innovative Research in Science, Engineering and Technology (ISO 3297*: *2007 Certified Organization)*, **2** (2013) 1 - 7.

[18] M. E. Dry, The Fischer-Tropsch process: 1950 - 2000, *Journal of Chemical Technology and Biotechnology*, **71** (2002) 227 - 241.

[19] H. Schulz, M. Claeys, Kinetic modelling of Fischer-Tropsch product distributions, *Applied Catalysis A: General*, **186** (1999) 91 - 107.

[20] A. N. Pour, Y. Zamani, A. Tavasoli, S. M. K. Shahri, S. A. Taheri, Study on products distribution of iron and iron-zeolite catalysts in Fischer-Tropsch synthesis, *Fuel*, **87** (2008) 2004 - 2012.

[21] T. T. Phadi, Titanium dioxide-carbon spheres composites for use as supports in cobalt Fischer-Tropsch synthesis, MSc. Thesis, University of the Witwatersrand, South Africa (2008).

[22] F. Regali, L. F. Liotta, A. M. Venezia, V. Montes, M. Boutonnet, S. Järas, Effect of metal loading on activity, selectivity and deactivation behaviour of Pd/silica-alumina catalysts in the hydroconversion of n-hexadecane, *Catalysis Today*, **214** (2013) 12-18. Supporting information.

[23] C. Bouchy, G. Hastoy, E. Guillon, J. A. Martens, Fischer-Tropsch waxes upgrading via hydrocracking and selective hydroisomerization, *Oil and Gas Science and Technology - Rev. IFP*, **64** (2009) 91 - 112.

[24] R. S. París, Noble metal catalysts for the hydrocracking of FT waxes, PhD Thesis, KTH - Royal Institute of Technology Sweden, Sweden (2012).

[25] J. J. W. Ward, Hydrocracking processes and catalysts, *Fuel Processing Technology*, **35** (1993) 55 - 85.

[26] J. A. Hansen, N. J. Blom, J. W. Ward, Hydrocracking process, US 7749373 B2, (2010).

[27] J. A. Hansen, N. J. Blom, J. W. Ward, Two-catalyst hydrocracking process, CA 2601982 C, (2013).

[28] K. M Ng, C. F. Chu, Trickle-bed reactors, *Chemical Engineering Process*, **83** (1987) 65 - 68.

[29] V. V. Ranade, R. Chaudhari, P. R. Gunjal, Trickle Bed Reactors: Reactor engineering and applications, Elsevier, (2011) 77 - 78.

[30] C. Ndimande, Ideal hydrocracking catalysts for the conversion of FT wax to diesel, MSc. thesis, University of Cape Town, South Africa (2012).

[31] H. L. Coonradt, W. E. Garwood, Mechanism of hydrocracking reactions of paraffins and olefins, *Industrial and Engineering Chemistry Process Design and Development*, **3** (1964) 38 - 45.

[32] J. Weitkamp, Catalytic Hydrocracking-Mechanisms and Versatility of the Process, *ChemCatChem*, **4**, (2012) 292 - 306.

[33] S. Sartipi, M. Makkee, F. Kapteijn, J. Gascon, Catalysis engineering of bifunctional solids for the one-step synthesis of liquid fuels from syngas: A review, *Catalysis Science and Technology*, **4** (2014) 893 - 907.

[34] R. Brosius, J. C. Q. Fletcher, Hydrocracking under Fischer–Tropsch conditions; the effect of CO on the mass transfer resistance by metal clusters, *Journal of Catalysis*, **317** (2014) 318 - 325.

[35] J. W. Thybaut, C. S. L. Narasimhan, J. F. Denayer, G. V. Baron, P. A. Jacobs, J. A. Martens, G. B. Marin, Acid-Metal balance of a hydrocracking catalyst: Ideal versus nonideal behavior, *Industrial and Engineering Chemistry Research,* **44** (2005) 5159 - 5169.

[36] J. Binneman, The hydrocracking of long chain *n*-paraffins under Fischer-Tropsch conditions, MSc. dissertation, University of Cape Town, South Africa (2012).

[37] M. J. Girgis, Y. P. Tsao, Impact of Catalyst Metal-Acid Balance in n-Hexadecane Hydroisomerization and Hydrocracking, *Industrial and Engineering Chemistry Research,* **35** (1996) 386 - 39.

[38] E. J. Creyghton, C. Ouwehand, Hydrocracking catalyst, US 2004/0152587 A1, (2004).

[39] R. A. Flinn, O. A. Larson, H. Beuther, The mechanism of catalytic hydrocracking, *Industrial and Engineering Chemistry*, **52** (1960) 153 - 157.

[40] I. Rossetti, C. Gambaro, V. Calemma, Hydrocracking of long chain linear paraffins, *Chemical Engineering Journal*,**154** (2009) 295 - 301.

[41] I. E. de la Fuente, Noble metal catalysts for the hydrocracking of Fischer-Tropsch waxes: Characterization and testing, MSc. Thesis, KTH-Royal Institute of Technology Stockholm, Sweden (2012).

[42] K. Na, S. Alayoglu, R. Ye, G. A. Somorjai, Effect of acidic properties of mesoporous zeolites supporting Pt nanoparticles on hydrogenative conversion of methylcyclopentane, *Journal of the American Chemical Society*, **136** (2014) 17207 - 17212.

[43] T. F. F. Lopes, Synthesis and evaluation of bifunctional catalysts for biofuels production, PhD Thesis, Technical University of Lisbon, Portugal (2009).

[44] C. Colella, W. S. Wise, The IZA handbook of natural zeolites: A tool of knowledge on the most important family of porous minerals, Original Research Article, *Microporous and Mesoporous Materials*, **189** (2014) 4 - 10.

[45] C. Colella, Natural zeolites, Original Research Article, *Studies in Surface Science and Catalysis*, **157** (2005) 13 - 40.

[46] J. Weitkamp, Zeolite and catalysis, *Solid State,* **131** (2000) 175 - 188.

[47] D. W. Breck, W. G. Eversole, R. M. Milton, T. B. Reed, T. L. Thomas, Crystalline zeolites. I. The properties of a new synthetic zeolite, Type **A**, *Journal of the American Chemical Society,* **78** (1956).

[48] R. J. Argauer, G. R. Landolt, Crystalline zeolite HZSM-5 and method of preparing the same, US Patent 3702886 (1972).

[49] T. C. Keller, S. Isabettini, D. Verboekend, E. G. Rodrigues, J. Pérez-Ramírez, Hierarchical high-silica zeolites as superior base catalysts, *Chemical Science*, **5** (2014) 677 - 684

[50] S. S. Bhoware and A .P. Singh, Characterization and catalytic activity of cobalt containing MCM-41 prepared by direct hydrothermal, grafting and immobilization methods*. Journal of Molecular Catalysis A: Chemical*, **266** (2007) 118 - 130.

[51] C. T. Kresge, M. E. Leonowicz, W. J. Roth, J. C. Vartuli, Nature, **359** (1992) 710 - 712.

[52] M. S. Holm, E. Taarning, K. Egeblad, C. H. Christensen, Catalysis with hierarchical zeolites, *Catalysis Today*, **168** (2011) 3 - 16.

[53] F. Zhang, Y. Yan, H. Yang , Y. Meng, C. Yu, B. Tu, D. Zhao, Understanding effect of wall structure on the hydrothermal stability of mesostructured silica SBA-15, *The Journal of Physical Chemistry B*, **109** (2005) 8723 - 8732.

[54] T. F. Degnan, Recent progress in the development of zeolitic catalysts for the petroleum refining and petrochemical manufacturing industries, *Studies in Surface Science and Catalysis*, **170** (2007) 54 - 65.

[55] C. Woltz, Kinetic studies on alkane hydroisomerization, over bifunctional catalysts, PhD Thesis, Technische Universität München, Germany (2005).

[56] R. Xu, W. Pang, J. Yu, Q. Huo, J. Chen, Chemistry of zeolites and related porous materials: Synthesis and structure, John Wiley and Sons (2009) 361 - 362.

[57] E. M. Flanigen, Chapter 2: Zeolites and molecular sieves on historical perspective, *Studies in Surface Science and Catalysis*, **58** (1991) 13 - 34.

[58] M. A. Rahman, M. A. K. Azad, S. Ahsan, S. Islam, M. A. Motin, M. Asadullah, Measurement of Brønsted acidity of silica-alumina solid catalyst by base exchange method, *Journal of Surface Science and Technology*, **22** (2006) 25 - 33.

[59] G. E. Giannetto, G. R. Perot, M. R. Guisnet, Hydroisomerization and hydrocracking of *n*-alkanes. 1. Ideal hydroisomerization PtHY catalysts, *Industrial & Engineering Chemistry: Product Research and Development*, **25** (1986) 481 - 490.

[60] C. Baerlocher, L. B. McCusker, D. H. Olson, Structure Commission of the International Zeolite Association, (2013).

[61] J. P. Brunelle, B. Delmon, P. Grange, P. A. Jacobs, G. Poncelet (Eds), Preparation of calalysts, Elsevier, Amsterdam, **11** (1979) 21- 24.

[62] R. Xu, W. Pang, J. Yu, Q. Huo, M. Chen, Chemistry of zeolites and related porous materials, synthesis and structure, John Wiley and Sons, (2007).

[63] G. T. Kerr, Kokotailo G. T, Sodium zeolite ZK-4, a new synthetic crystalline aluminosilicate, *Journal of the American Chemical Society*, **83** (1961) 4675 - 4676.

[64] D. Georgiev, B. Bogdanov, K. Angelova, I. Markovska, Y. Hristov, Synthetic zeolites - structure, classification, current trends in zeolite synthesis: Review,

International Science conference, Stara Zagora, Bulgaria, 4th - 5th June (2009).

[65] C. S. Cundy, P. A. Cox, The hydrothermal synthesis of zeolites: History and development from the earliest days to the present time, *Chemical Reviews*, **103** (2003) 663 - 701.

[66] Q. Zhang, S. Hu, L. Zhang, Z. Wu, Y. Gong, T. Duo, Facile fabrication of mesopore-containing ZSM-5 zeolite from spent zeolite catalyst for methanol to propylene reaction, *Green Chemistry*, **16** (2014) 77 - 81.

[67] K. Cho, Zeolites with multi-level pore hierarchy: Synthesis, characterisation of diffusion property and catalytic investigation, PhD Thesis, KAIST, South Korea, (2012).

[68] K. Na, M. Choi, R. Ryoo, Recent advances in the synthesis of hierarchically nanoporous zeolites, *Microporous and Mesoporous Materials*, **166** (2013) 3 - 19.

[69] D. P. Serrano, J. Aguado, J. M. Escola, Hierarchical zeolites: materials with improved accessibility and enhanced catalytic activity, *Catalysis*, **23** (2010) 253 - 283.

[70] K. Li, J. Valla, J. Garcia-Martinez, Realizing the commercial potential of hierarchical zeolites: New opportunities in catalytic cracking, *ChemCatChem,* (2013) 1 - 22. *Review.*

[71] K. Egeblad, C. H. Christensen, M. Kustova, C. H. Christensen, Templating Mesoporous Zeolites, *Chemistry of Materials*, **20** (2008) 946 - 960. *Review.*

[72] C. H. Christensen, I. Schmidt, Improved performance of mesoporous zeolite single crystals in catalytic cracking and isomerization of *n*-hexadecane, *Catalysis Communications*, **5** (2004) 43 -546.

[73] J. Zhu, X. Meng, F. Xiao, Mesoporous zeolites as efficient catalysts for oil refining and natural gas conversion, *Frontiers of Chemical Science and Engineering,* **7** (2013) 233 - 248.

[74] Y. Tao, H. Karoh, K. Kaneko, Synthesis of hierarchical zeolites, US Patent 6998104 B2 (2006).

[75] J. Wang, Synthesis of Zeolite Composites with Hierarchical Porosity, PhD Thesis, Delft University of Technology, Netherlands (2008).

[76] F. Ocampo, H.S. Yun, M. M. Pereira, J. P. Tessonnier, B. Louis, Design of MFI zeolite-based composites with hierarchical pore structure: a new generation of structured catalysts, *Crystal Growth and Design*, **9** (2009) 3721 - 3729.

[77] S. Mitchell, A. Bonilla, J. Pérez-Ramírez, Preparation of organic-functionalized mesoporous ZSM-5 zeolites by consecutive desilication and silanization, *Materials Chemistry and Physics*, **127** (2011) 278 - 284.

[78] D. Tzoulaki, A. Jentys, J. Pérez-Ramírez, K. Egeblad, J. A. Lercher, On the location, strength and accessibility of Brønsted acid sites in hierarchical ZSM-5 particles, *Catalysis Today*, **198** (2012) 3 - 11.

[79] F. Schmidt, M. R. Lohe, B. Büchner, F. Giordanino, F. Bonino, S. Kaskel, Improved catalytic performance of hierarchical ZSM-5 synthesized by desilication with surfactants, *Microporous and Mesoporous Materials*, **165** (2013) 148 - 157.

[80] D. Verboekend, J. Pérez-Ramírez, Design of hierarchical zeolite catalyst by desilication, *Catalysis Science and Technology*, **1** (2011) 879 - 890.

[81] R. M. Dessau, E. W. Valyocsik, N. H. Goeke, Aluminium zoning in ZSM-5 as revealed by selective silica removal, *Zeolites*, **12** (1992) 776 - 779.

[82] J. C. Groen, L. A. A. Peffer, J. A. Moulijn, J. Pérez-Ramírez, Mechanism of hierarchical porosity development in MFI zeolites by desilication: The role of Aluminium as a pore-directing agent, *Chemistry - A European Journal*, **11** (2005) 4983 - 4994.

[83] D. Verboekend, S. Mitchell, M. Milina, J. C. Groen, J. Pérez-Ramírez; Full compositional flexibility in the preparation of mesoporous MFI zeolites by desilication, *Journal of Physical Chemistry*, **115** (2011) 14193 - 14203.

[84] J. C. Groen, J. A Moulijn, J. Pérez-Ramírez, Desilication on the controlled generation of mesoporosity in MFI zeolites, *Journal of Materials Chemistry*, **16** (2006) 2121 - 2132.

[85] J. Pérez-Ramírez, S. Abelló, A. Bonilla, J. C. Groen, Tailored mesoporosity development in zeolite crystals by partial detemplation and desilication, *Advanced Functional Materials*, **19** (2009) 164 - 172.

[86] M. Ogura, S. Shinomiya, J. Tateno, Y. Nara, E. Kikuchi, M. Matsukata, Formation of uniform mesopores in ZSM-5 zeolite through treatment in alkaline solution, *Chemistry Letters*, (2000) 882 - 883.

[87] B. Liu, C. Li, Y. Ren, Y. Tan, H. Xi, Y. Qian, Direct synthesis of mesoporous ZSM-5 zeolite by a dual-functional surfactant approach, *Chemical Engineering Journal*, **210** (2012) 96 - 102.

[88] X. Li, M. Sun, J. C. Rooke, L. Chen, B. L Su, Synthesis and applications of hierarchically porous catalysts, *Chinese Journal of Catalysis*, **34** (2013) 22 - 47.

[89] J. Kim, W. Park, R. Ryoo, Surfactant-directed zeolite nanosheets: A high-performance catalyst for gas-phase Beckmann rearrangement, *Catalysis*, **1** (2011) 337 - 341.

[90] L. Emdadi, Y. Wu, G. Zhu, C-C. Chang, W. Fan, T. Pham, R. F. Lobo, D. Liu, Dual template synthesis of meso- and microporous MFI zeolite nanosheet assemblies with tailored activity in catalytic reactions, *Chemistry of Materials,* **26** (2014) 1345 - 1355.

[91] K. Cho, K. Na, J. Kim, O. Terasaki, R. Ryoo, Zeolite synthesis using hierarchical structure-directing surfactants: retaining porous structure of initial synthesis gel and precursors, *Chemistry of Materials*, **24** (2012) 2733 - 2738.

[92] Y. Han, Y. Wang, Aggregation behavior of gemini surfactants and their interaction with macromolecules in aqueous solution, *Physical Chemistry Chemical Physics,* **13 (**2011) 1939 - 1956.

[93] D. Leckel, M. Liwanga-Ehumbu, Diesel-selective hydrocracking of an iron-based Fischer-Tropsch wax fraction (C_{15}-C_{45}) Using a MoO_3-modified noble metal catalyst, *Energy and Fuels*, **20** (2006) 2330 - 2336.

[94] P. D. T. Wynne, The effect of metal type and loading on n-paraffin hydrocracking conversion and selectivity, MSc. Dissertation, University of Cape Town, South Africa (2013).

[95] J. Scherzer, A. Gruia, Hydrocracking Science and Technology, Chapter 3. Marcel Dekker Inc., New York, 1st edition (1996).

[96] R. Sahu, B. J. Song, J. S. Im, Y-P. Jeon, C. W. Lee, A review of recent advances in catalytic hydrocracking of heavy residues: Review article, *Journal of Industrial and Engineering Chemistry*, **27** (2015) 12 - 24.

[97] U. Ghosh, K. Kulkarni, A. D. Kulkarni, P. L. Chaudhari, Review – hydrocracking using different catalysts, *Chemical and Process Engineering Research,* **34** (2015) 1 - 6.

[98] J. W. Ward, Design and preparation of hydrocracking catalysts, *Studies in Surface Science and Catalysis,* **16** (1983) 587 - 618.

[99] L. Jiao, J. R. Regalbuto, The synthesis of highly dispersed noble and base metals on silica via strong electrostatic adsorption: I. Amorphous silica, *Journal of Catalysis*, **26** (2008) 329 - 341.

[100] F. J. Derbyshire, P. Varghese, Hydrocracking of heavy feeds with dispersed dual function catalyst, US 4604189 A (1986).

[101] B. Wang, Zeolite deactivation during hydrocarbon reactions: Characterisation of coke precursors and acidity product distribution, PhD Thesis, University College London, London (2007).

[102] C. H. Bartholomew, Mechanisms of catalyst deactivation, *Applied Catalysis A: General*, **212**, (2001) 17 - 60.

[103] M. D. Argyle, C. H. Bartholomew, Heterogeneous catalyst deactivation and regeneration: A review, *Catalysts*, **5** (2015) 145 - 269.

[104] W. G. Appleby, J. W. Gibson, G. M. Good, Coke formation in catalytic cracking, *I and Ec Process Design And Development*, **1** (1962) 103 - 110.

[105] R. Valoyi, Modelling water removal from Fischer-Tropsch products using glycerol, MSc. Dissertation, University of the Witwatersrand, South Africa (2011).

[106] T. Y. Yan, N. J. Pitrnan, Hydrocracking activity and selectivity of a rare earth crystalline zeolite, US 3546100 (1970).

[107] J. Haber, J. H. Block, B. Delmon, Manual of methods and procedures for catalyst characterization, *International Union Of Pure And Applied Chemistry Pure*, **67** (2005) 1257 - 1306.

[108] H. van Koningsveld, J.M. Bennett, Zeolite structure determination from X-Ray Diffraction, *Molecular Sieves*, **2** (1999) 1 - 29.

[109] M. Thommes, Chapter 15: Textural characterization of zeolites and ordered mesoporous materials by physical adsorption, *Studies in Surface Science and Catalysis*, **168** (2007) 495 - 523.

[110] S. Naumov, Hysteresis phenomena in mesoporous materials, PhD Thesis, Leipzig University, Germany (2009). M. Khatamiana, M. Irania, Preparation and characterization of nanosized ZSM-5 zeolite using Kaolin and investigation of Kaolin content, crystallization time and temperature changes on the size and crystallinity of products, *Journal of the Iranian Chemical Society*, **6** (2009) 187 - 194

[111] A. G. Ashton, S. Batmanian, D. M. Clark, J. Dwyer, F. R. Fitch, A. Hinchcliffe, F.J. Machado, Acidity in zeolites, *Studies in Surface Science and Catalysis*, **20** (1985) 101 - 109.

[112] L. Sandoval-Díaz, J. González-Amaya, C. Trujillo, General aspects of zeolite acidity characterization: Review Article, *Microporous and Mesoporous Materials*, **215** (2015) 229 - 243.

[113] M. Niwa, N. Katada Measurements of acidic property of zeolites by temperature programmed desorption of ammonia, *Catalysis Surveys from Japan,* **1** (1997) 215 - 226.

[114] V. Dondur, V. Raki, L. Damjanovi, A. Auroux, Comparative study of the active sites in zeolites by different probe molecules, *Journal of the Serbian Chemical Society,* **70** (2005) 457 - 474.

[115] C. I. Round, S. J. Hill, K. Latham, C. D. Williams, The crystal morphology of zeolite A. The effects of the source of the reagents, *Microporous Materials,* **11** (1997) 213 - 225.

[116] T. O. Drews, M. Tsapatsis, Progress in manipulating zeolite morphology and related applications, *Current Opinion in Colloid and Interface Science*, **10** (2005) 233 - 238.

[117] Z. A. ALOthman, A Review: Fundamental aspects of silicate mesoporous materials, *Materials,* **5** (2012) 2874 - 2902.

[118] M. Thommes, Chapter 15: Textural characterization of zeolites and ordered mesoporous materials by physical adsorption, *Studies in Surface Science and Catalysis*, **168** (2007) 495 - 523.

[119] S. Naumov, Hysteresis phenomena in mesoporous materials, PhD Thesis, Leipzig University, Germany (2009).

CHAPTER 3

Methodology and Experimental Procedures

3.1 Introduction

This chapter describes, in detail, the methods and experimental procedures for the synthesis of hierarchical ZSM-5 zeolites, their characterisation using different physicochemical techniques, their use in preparing hydrocracking catalysts and lastly the catalytic activity testing of these catalysts in the hydrocracking of *n*-hexadecane as model LTFT wax component. Two synthesis approaches for the production of hierarchical zeolites are presented with their pertinent details, *viz*., (i) the indirect route and (ii) the direct route. The indirect route involves prior synthesis of bulk ZSM-5 zeolites, followed by NaOH-assisted desilication. The direct synthesis route involves prior synthesis of three polyquaternary ammonium surfactants using synthetic organic chemistry approaches, followed by their incorporation into synthesis gel mixtures to function as structure-directing agents for the production of multi-porous zeolites. The formulae and abbreviations of the surfactants synthesised and used in this study are given below:

(i) $[C_{18}H_{37}\text{-}N^{+}(CH_3)_2\text{-}C_6H_{12}\text{-}N^{+}(CH_3)_2\text{-}C_6H_{13}][Br^{-}]_2$, designated 18-$N_2$

(ii) $[C_{18}H_{37}\text{-}N^{+}(CH_3)_2\text{-}C_6H_{12}\text{-}N^{+}(CH_3)_2\text{-}C_6H_{12}\text{-}N^{+}(CH_3)_2\text{-}C_{18}H_{37}][Br^{-}]_3$, designated

18-N_3-18

(iii) $[C_{18}H_{37}\text{-}N^{+}(CH_3)_2\text{-}C_6H_{12}\text{-}N^{+}(CH_3)_2\text{-}C_6H_{12}\text{-}N^{+}(CH_3)_2\text{-}C_6H_{12}\text{-}N^{+}(CH_3)_2\text{-}C_{18}H_{37}][Br^{-}]_4$, designated 18-$N_4$-18

3.2 Synthesis of zeolites

All chemicals and reagents used in the synthesis procedures reported in this chapter are summarised in Table 3.1. The zeolites were synthesised hydrothermally using a high pressure reactor, *viz.*, 1 L Parr 4848 autoclave. This reactor has operating pressures up to 5000 psi (345 bar) and temperatures up to 500 °C. It is fitted with a magnetic drive and a turbine-type impeller, which allow overhead stirring of the synthesis mixture.

Table 3.1 Chemicals, reagents and their composition

Materials	**Supplier**	**Assay (%)**
Methanol-d_4	Sigma-Aldrich	99.8 atom % D
N,N,N',N'-tetramethyl-1,6-diaminohexane	Sigma-Aldrich	99
N,N-dimethyloctadecylamine	ACROS Chemicals	85
Acetonitrile	Sigma-Aldrich	99
Toluene	Fisher Chemicals	99
Diethyl ether	Sigma-Aldrich	99
1-Bromohexane	Sigma-Aldrich	95
1,6-Dibromohexane (99%)	Sigma-Aldrich	99
Chloroform	Sigma-Aldrich	95
1-Bromooctadecane	Sigma-Aldrich	96
Tetraethylorthosilicate	Aldrich	95
Ethanol	LabChem	99.5
Sodium aluminate	Riedel de Haen	42.5 (Na_2O), 53 (Al_2O_3)
Tetrapropylammonium bromide	Aldrich	98
Sodium hydroxide	Rochelle Chemicals	99
Aerosil 200	Degussa	100
Ammonium nitrate	Sigma	98
Tetraaminepalladium (II) nitrate	Alfa Aesar	6.41
n-hexadecane	Sigma-Aldrich	99
Silver nitrate	Rochelle Chemicals	99.8

3.2.1 Synthesis of hierarchical zeolites via a desilication route

3.2.1.1 Synthesis of the bulk ZSM-5

The method reported by Nicolaides *et al.* [1] was used to synthesise bulk ZSM-5 zeolites with three silica-to-alumina ratios (SARs). The various amounts of silica used are represented by x in the gel molar composition given below:

$$x\ SiO_2 : Al_2O_3 : 13\ Na_2O : 3\ (TPA)_2O : 3978\ H_2O \quad \text{(where x = 50, 77 and 100)}$$

Sodium aluminate was dissolved in water and added to a silica slurry (containing Aerosil 200 and distilled water), followed by the addition of tetrapropylammonium bromide solution under vigorous stirring. The mixture was stirred until homogeneous. The final gel was transferred into an autoclave for hydrothermal treatment at 150 °C for 48 h under stirring. At the end of the synthesis, the autoclave was cooled and the solid product was recovered by filtration using a porcelain Buchner funnel. The product was washed with several litres of distilled water until free of Br^- ions. This was confirmed by the absence of a creamy AgBr precipitate after adding a dilute $AgNO_3$ solution to the filtrate. The zeolite product was then dried in an oven overnight at 120 °C and calcined at 550 °C for 5 h. The resulting materials will be designated P-ZSM-5(x), with P referring to the pristine zeolite and x representing its SAR.

3.2.1.2 Desilication of bulk ZSM-5 zeolites

The method of desilication has been adapted from previous works with slight modifications [2, 3]. Approximately 5 g of the ZSM-5 zeolite was added to 150 ml of a 0.2 M solution of NaOH in a round bottom flask and refluxed at 65 °C for 0.5 h. The round bottom flask was subsequently cooled down to room temperature and the contents were filtered to recover the solid product. The solid was further washed with distilled water until pH 7 and dried overnight at 100 °C. All the zeolite samples were converted into the NH_4^+-form using 0.5 M solution of NH_4NO_3, by a four-fold ion-exchange at 60 °C for 1 h. The resulting solids were washed, dried overnight at 100 °C in an oven and then converted to the H^+-form via calcination in static air at 550 °C for 5 h. The resulting materials will be designated D-ZSM-5(x*), with D referring to

the desilicated zeolite and x* representing its SAR (the asterisk emphasise the uncertainty in the SAR that is brought about by desilication).

3.2.2 Synthesis of polyquaternary ammonium surfactants

The various surfactants were synthesised and purified in the laboratory according to the method described in previous works with slight modification [4 - 6]. The final solid products were a confirmed by ^{1}H NMR spectroscopy (as MeOD solutions) using a Bruker 400 MHz Avance III HD spectrometer.

3.2.2.1 Synthesis of 18-N_2

An amount of 3.3 g 1-bromooctadecane and 17.2 g of N,N,N',N'-tetramethyl-1,6-diaminohexane were dissolved in 100 ml of acetonitrile/toluene mixture (1:1 v/v) and reacted under magnetic stirring at 60 °C for 10 h. After cooling to room temperature, the organic solvents were removed using a rotary evaporator. The rotary evaporator and its content were then cooled to room temperature and the subsequently precipitated product, $C_{18}H_{37}$-$N^{+}(CH_3)_2$-C_6H_{12}-$N(CH_3)_2(Br^{-})$, was washed with 200 ml of diethyl ether and dried in an oven at 50 °C to remove the organic solvent. Thereafter, 5.4 g of $C_{18}H_{37}$-$N^{+}(CH_3)_2$-C_6H_{12}-$N(CH_3)_2(Br^{-})$ and 2.5 g of 1-bromohexane were dissolved in 30 ml of acetonitrile and refluxed at 60 °C for 10 h. After cooling to room temperature, acetonitrile was removed using a rotary evaporator. The precipitated product (18-N_2) was filtered by suction filtration, washed with 200 ml diethyl ether in portions, and dried overnight in an oven at 50 °C.

3.2.2.2 Synthesis of 18-N_3-18

Two intermediates, $C_{18}H_{37}$-$N^{+}(CH_3)_2$-C_6H_{12}-$Br(Br^{-})$ (**A**) and $C_{18}H_{37}$-$N^{+}(CH_3)_2$-C_6H_{12}-$N^{+}(CH_3)_2$ (**B**) were prepared separately as starting materials for the preparation of the 18-N_3-18 surfactant.

For the synthesis of **A**, 0.034 mol N,N-dimethyloctadecylamine and 0.34 mol 1,6-dibromohexane were dissolved in 1000 ml acetonitrile/toluene mixture (1:1 v/v) in a round bottom flask, and heated at 60 °C for 12 h. After cooling to room temperature and subsequent solvent evaporation using rotary evaporator, the solid product was precipitated. The product was filtered, washed with 200 ml diethyl ether in portions, and dried in an oven at 50 °C for 2 h.

For the synthesis of **B**, 0.030 mol 1-bromooctadecane and 0.300 mol N,N,N',N'-tetramethyl-1,6-diaminohexane was dissolved in 600 ml of acetonitrile/toluene (1:1 v/v) mixture using a round bottom flask and heated at 60 °C for 12 h. After quenching in cold water, the product was filtered, washed with 200 ml diethyl ether in portions, and dried at room temperature for 12 h.

Finally, equimolar amounts of **A** and **B** were dissolved in 100 ml of acetonitrile in a round bottom flask and refluxed at 60 °C for 12 h. After solvent evaporation using a rotary evaporator, the precipitated product was filtered, washed with diethyl ether and dried in an oven at 50 °C to obtain the final product, the 18-N_3-18 surfactant.

3.2.2.3 Synthesis of 18-N_4-18

An amount of 5.4 g of $C_{18}H_{37}$-$N^+(CH_3)_2$-C_6H_{12}-$N(CH_3)_2$-$Br^-(Br^-)$, synthesised as in Section 3.2.2.1, was reacted with 1.22 g of 1,6-dibromohexane in 50 ml of chloroform in a round bottom flask under reflux at 60 °C for 24 h. After cooling to room temperature, chloroform was removed using a rotary evaporator. The precipitated product, 18-N_4-18 surfactant, was filtered, washed with 200 ml diethyl ether in portions and dried at room temperature.

3.2.3 Surfactant-templated synthesis of hierarchical ZSM-5 zeolites

The synthesis of hierarchical ZSM-5 zeolites was synthesised following the method reported in literature [6], with some modifications. In a typical synthesis a homogeneously mixed solution was first prepared from tetraethylorthosilicate (TEOS), the surfactant (18-N_2 or 18-N_3-18 or 18-N_4-18), $NaAlO_2$, NaOH, EtOH and H_2O with a gel molar composition:

$$6.67\ Na_2O:\ 0.75\ Al_2O_3:\ 30\ SiO_2:\ 1.5\ \text{surfactant}:\ 240\ \text{ethanol}:\ 2132\ H_2O$$

Firstly, a clear solution of the surfactant was obtained by dissolving the surfactant in distilled water under magnetic stirring at 50 °C. In a separate beaker, TEOS was hydrolysed by adding distilled water under vigorous stirring and subsequently added into the clear solution containing the surfactant. All the necessary reagents were then mixed and agitated under magnetic stirring at 60 °C for 6 h. The resulting gel was transferred to an autoclave and heated at 140 °C for 96 h. After crystallisation, the product was filtered, washed with several litres of distilled water until all Br^- ions

were removed, and dried in an oven at 120 °C for 12 h. The product was calcined at 550 °C for 4 h in order to remove the organic surfactants. The calcined product was converted into the NH_4^+-form with a four-fold exchange using 0.1 M NH_4NO_3 solution, washed with distilled water, dried overnight at 120 °C and then converted to the H^+-form via calcination in static air at 550 °C for 4 h. The designation HSZ(N_y), will be used throughout to represent surfactant-templated hierarchically-structured zeolite-based supports with a nominal SAR of 40, where y is the number of quaternary ammonium centres in the surfactant.

3.3 Characterisation techniques

3.3.1 XRD analysis

Approximately 1 g of the sample was ground to a fine powder using pestle and mortar and mounted on an acetone-cleaned aluminium plate sample-holder. In order to achieve sample flatness, a glass slide was used for removal of excess powder. It was then mounted in the sample chamber of the diffractometer. The X-ray diffraction patterns of the various zeolite samples were collected on Philips PW 1830 X-ray diffractometer using Cu-Kα radiation (λ = 1.5405 Å), operating at a voltage of 40 kV and a tube current of 40 mA. The scanning speed was 0.025°/s over the 2θ range of 2 - 63°. The XRD patterns were then recorded on the computer equipped with a PC-APD diffraction software and saved in Microsoft Excel 2010 format for analysis.

3.3.2 FT-IR analysis

The FT-IR spectroscopic analysis was carried out using Agilent Cary 600 series FT-IR spectrophotometer. Approximately 0.01 g of the zeolites was ground using pestle and mortar to a fine powder. The fine powdered sample was then placed onto a removable diamond crystal floor plate in the sample compartment. The spectra were recorded at room temperature in the wavenumber range 550 - 4000 cm^{-1} by collecting 140 scans at a resolution of 4 cm^{-1}.

3.3.3 SEM analysis

A 40.0 mm x 20.4 mm aluminium stub was covered with 12 mm double-sided carbon tape (S-05082-AB, SPI Supplies, USA). The carbon tape was attached to a

transparency paper, which was subsequently cut into small (12 mm x 3 mm) pieces to strengthen the carbon tape. These pieces were dipped into the sample resulting in small quantities (~ 0.1 mg) of powder attaching to the carbon tape. Several (6 - 8) of these small carbon tape pieces containing different samples were placed on the double-sided carbon tape that was attached to the aluminium stub. Excess powder was removed by using a single blast of compressed dry nitrogen gas. The samples were then coated with gold under argon gas using an Emitech K550X sputter coater (Ashford, England), viewed on a scanning electron microscope, JEOL JSM-5800LV (JEOL, Tokyo, Japan) and then imaged at 5 kV. The lower beam intensity was used to achieve the optimum resolution for a specific magnification.

3.3.4 N_2 adsorption analysis

Nitrogen adsorption experiments were carried out using a TriStar II 3020 version 2.00 Surface Area and Porosity Analyser (Micromeritics). For the sorption measurements, approximately 0.2 g of the sample was degassed at 120 °C for at least 12 h to ensure that the water inside the pores was completely removed and subsequently cooled to room temperature. The surface areas were measured from the adsorption and desorption isotherms of N_2 at -196 °C at relative pressures (P/P_0) in the range of 0.00 - 0.99.

3.4 Hydrocracking catalyst preparation

All the Pd/zeolite catalysts were prepared using the incipient wetness impregnation method using an aqueous solution of $[Pd(NH_3)_4](NO_3)_2$. The Pd loading of 0.9 wt.% was predominantly used, except a few cases where the loading was increased to 1.8 wt.%. The mass of Pd^{2+} solution required to impregnate the zeolite to incipient wetness was determined using equation 3.1.

$$M_m = M_z * W_m / W_s \quad \text{.....(3.1)}$$

The parameters in equation 3.1 are defined as follows:

M_m = mass of the Pd(ll) solution (g)

M_z = mass of the zeolite (g)

W_m = desired metal (Pd) loading (%)

W_s = Pd(ll) solution assay (%)

The amount of water required to incipient wet the zeolite was preliminarily determined using 1 g of the zeolite. Equation 2.2 shows how the total mass of water for each sample was determined

$M_{wt} = M_{wi} * M_z$……...(3.2),

where M_{wt} = mass of total water required (g) and M_{wi} = initial mass of water determined (g).

An amount of about 2.2 g of zeolite support was used for each loading. The Pd^{2+} solution (0.3088 g), water and the weighed zeolite were mixed in a small beaker until the zeolite was incipient wet. The prepared catalyst was left to dry overnight at room temperature. The dried catalyst was then was placed in stainless steel press dies and compressed to 5 tons using a hydraulic press for 5 minutes, thereby forming small “briquettes”. These “briquettes” were then carefully crushed and sieved to obtain particles with a size range of 500 - 800 µm. This process makes it easier to handle the catalyst during loading and immobilising within the isothermal zone of the reactor.

3.4.1 The reactor description

A trickle-bed reactor depicted in Figure 3.1 was used for the hydrocracking experiments. The reactor body is made of a stainless steel tube 500 mm in length, an internal diameter of approximately 15.75 mm, and wall thickness of 1.651 mm. The head of the reactor is designed as a separate, removable unit, facilitating the ease with which the catalyst may be loaded and unloaded.

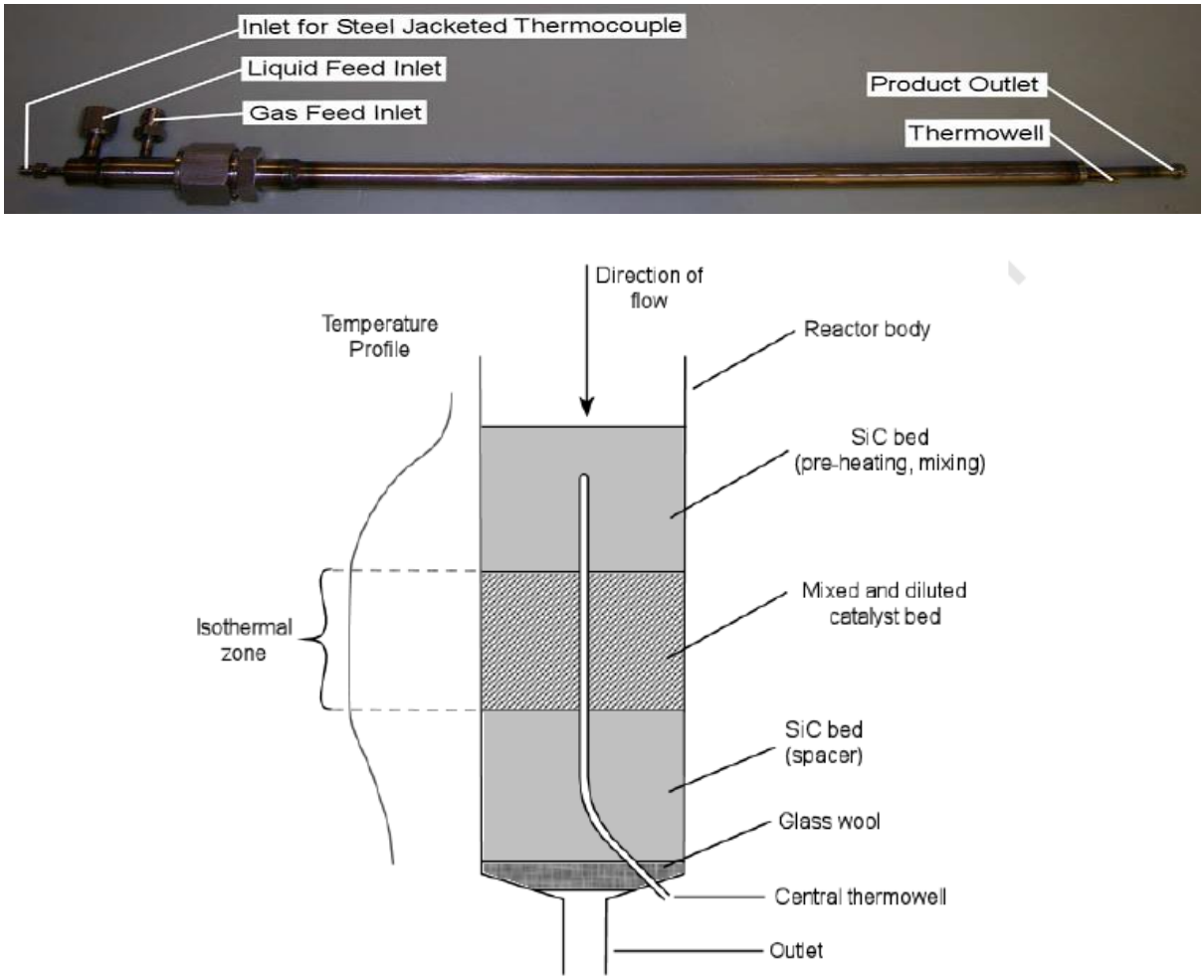

Figure 3.1 Schematic representation of (a) the reactor body, and (b) cross-sectional area view of the reactor [7].

3.4.2 Catalyst loading into the reactor

A stainless steel rod was used to help insert a small piece of glass wool-silane at the bottom of the reactor to prevent any particles from leaving the reactor. A measured 20 cm^3 silicon carbide (SiC) of 300 μm particle sizes was loaded, using a funnel, into the stainless steel tubular reactor as a support packing for the catalyst bed. A bed of SiC granules at the bottom allowed the position of the catalyst bed to be adjusted when loading. It was then followed by addition of 2 g of the pelletised catalyst, and finally adding extra SiC to fill the reactor above the catalyst bed, which afforded the zone for feed pre-heating and mixing. Silicon carbide was used because it exhibits a high thermal conductivity, high resistance towards oxidation, high mechanical strength, low specific weight, and chemical inertness [7].

3.5 Catalytic activity studies

Prior to the catalytic test runs, each catalyst was oxidised in oxygen at a flow rate of 120 ml/min, with temperature ramped from 25 to 350 °C at a heating rate 0.3 °C/min and keeping isothermal at 350 °C for 4 h. The reactor was then cooled to 225 °C under nitrogen flow prior to reduction. Reduction of the catalyst was performed overnight in 120 ml/min H_2 at a heating rate 0.4 °C/min up to 225 °C. Finally, the temperature was dropped to the desired reaction temperature (215 - 310 °C) in 48 ml/min H_2 flow, and subsequently the feed, *n*-C_{16}, was pumped into the reactor at 0.02 ml/min to commence catalytic test runs. During the course of the catalytic test runs, the reactor pressure was kept at 20 bar, WHSV = 1 h^{-1} and the H_2/*n*-C_{16} mole ratio of 10. Further experiments involved the co-feeding of CO and H_2O into the reactor as typical by-products of the FTS. This exercise was carried out to investigate the stability of these catalysts when coupled to an FT reactor. The co-feeding of H_2O and CO was performed after reaching a steady-state activity at a specific reactor temperature. These components were introduced in such a way that H_2/CO ratio = 2 and a H_2O flow rate of 0.02 ml/min.

The products were analysed using an online GC (Varian 3900) equipped with a non-polar column, a flame-ionisation detector, using H_2 gas as a carrier. The total *n*-C_{16} conversion (conversion *via* cracking and isomerisation) results were interpreted on a carbon basis and calculated using equation 3.3:

$$\text{Conversion}\ (\%) = 1 - \frac{\mathrm{A}_{n-\mathrm{C}_{16}}}{\sum_{i=\mathrm{C}_1}^{n-\mathrm{C}_{16}} \mathrm{A}_{\mathrm{C}_i}} \quad \text{.....(3.3),}$$

where $\mathrm{A}_{n-\mathrm{C}_{16}}$ is the peak area of unconverted *n*-C_{16}. The selectivity to cracking and isomerisation was obtained using equation 3.4:

$$\text{Selectivity} = \frac{\mathrm{A}_i \mathrm{C}_i}{\sum_{i=\mathrm{C}_1}^{n-\mathrm{C}_{16}} \mathrm{A}_{\mathrm{C}_i}} \quad \text{.....(3.4),}$$

where A_i is the peak area corresponding to the carbon species C_i.

The results of all experimental manoeuvres are presented and discussed in Chapter 4.

3.6 References

[1] C. P. Nicolaides, M. Waplennik, K. I. G. Weis, H. Van Der Akker, B. Van Zalk, P. Wielaard, Alkali metal cation exchange of ZSM-5 and the catalytic properties of alkylised zeolites, *Applied Catalysis*, **68** (1991) 31 - 39.

[2] S. Abelló, A. Bonilla, Mesoporous ZSM-5 zeolite catalysts prepared by desilication with organic hydroxides and comparison with NaOH leaching, *Applied Catalysis A: General*, **364** (2009) 191 - 198.

[3] J. C. Groen, L. A. A. Peffer, J. A. Moulijn, J. Pérez-Ramírez, Mechanism of hierarchical porosity development in MFI zeolites by desilication: The role of Aluminium as a pore-directing agent, *Chemistry - A European Journal*, Vol. **11** (2005) 4983 - 4994.

[4] X. Li, M. Sun, J. C. Rooke, L. Chen, B. L Su, Synthesis and applications of hierarchically porous catalysts, *Chinese Journal of Catalysis*, **34** (2013) 22 - 47.

[5] W. Park, D.Yu, K. Na, K.E. Jelfs, B. Slater, Y. Sakamoto, R. Ryoo, Hierarchically structure-directing effect of multi-ammonium surfactants for the generation of MFI zeolite nanosheets, *Chemistry of Materials*, **23** (2011) 513 - 5137: *Supporting information*.

[6] K. Na, C. Jo, J. Kim, K. Cho, J. Jung, Y. Seo, R. J. Messinger, B. F. Chmelka, R. Ryoo, Directing zeolite structures into hierarchically nanoporous architectures, *Science*, **333** (2011) 328 - 332.

[7] R. S. Kukard, The effect of zeolite type on the hydrocracking of long *n*-paraffins, MSc. Dissertation, University of Cape Town, South Africa (2008).

CHAPTER 4

Results and Discussion

4.1 Introduction

This chapter presents and discusses the results obtained upon physicochemical characterisation of the zeolitic materials synthesised in this work, as well as their catalytic performance in an industrially-relevant process, *viz*., the hydrocracking of LTFT wax using *n*-hexadecane as a representative hydrocarbon feedstock. Major characterisation techniques for zeolitic materials used in this work were XRD, FT-IR, SEM, N_2 adsorption isotherms and BET surface area measurements. The ^1H nuclear magnetic resonance spectroscopy was used to qualify the surfactant prepared in this work. Hierarchical zeolites used as acidic supports for hydrocracking catalyst systems were prepared using two different routes: (i) alkaline-desilication of tetrapropylammonium-templated ZSM-5 and (ii) direct polyquaternary ammonium-templated hydrothermal synthesis.

It is important to note that all zeolitic supports were characterised prior to impregnation with palladium and therefore, the observed catalytic performance of the catalysts will be rationalised in terms of the properties of the support. The silica-to-alumina ratio (SAR) assigned to each sample was determined from the gel composition, with no supporting physicochemical characterisation evidence, *i.e.,* the quoted values are nominal. This includes hierarchical zeolites prepared by desilication, which is clearly an over-simplification.

4.2 Characterisation

4.2.1 ^{1}HNMR spectroscopic study of surfactants

Polyquaternary ammonium surfactants were synthesised using procedures outlined in Chapter 3, and adapted from Na *et al.* [1]. These surfactants were characterised by ^{1}H NMR spectroscopy to confirm their purity. The structural formulas of polyquaternary ammonium surfactants used in this work and their designated codes are shown in Figure 4.1.

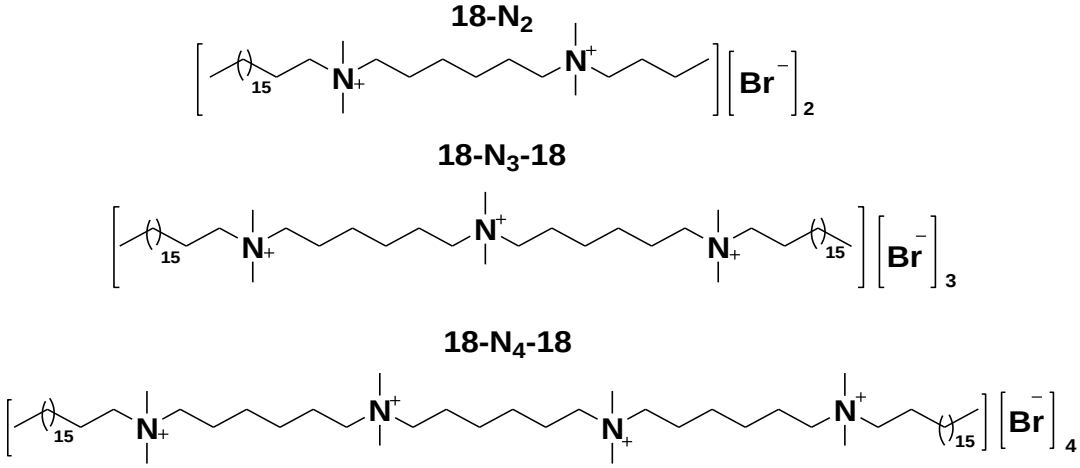

Figure 4.1 Structural formulas of polyquaternary-ammonium surfactants used as SDAs for the direct synthesis of hierarchical zeolites.

The ^{1}H NMR spectra of these surfactants are provided (see Appendices A1, A2 and A3). The chemical shifts obtained from ^{1}H NMR spectra of the surfactants abbreviated 18-N_2, 18-N_3-18 and 18-N_4-18 are shown below. For ease of analysis, the moieties responsible for the signals at the specific chemical shifts are given in bold.

(a) 18-N_2:

δ 0.9 (m, 6H, [**CH_3**-($C_{17}H_{34}$)], [**CH_3**-(CH_2)$_5$]); δ 1.3 - 1.5 (m, 40H, [CH_3-(**$C_{17}H_{34}$**)], [N^+-(CH_2)$_2$-(**CH_2**)$_2$-(CH_2)$_2$-N^+)], [CH_3-(**CH_2**)$_5$]); δ 1.8 (m, 8H, [-**CH_2**-(CH_2-N^+-CH_2)-**CH_2**]$_2$); δ 3 .1 (m, 12H, [N^+-(**CH_3**)$_2$]$_2$); and δ 3.3 (m, 8H, [N^+-(**CH_2**)$_2$]$_2$).

(b) 18-N_3-18:

δ 0.9 (t, 6H, [**CH_3**-($C_{17}H_{34}$)]$_2$); δ 1.3 - 1.5 (m, 66H, [CH_3-(**$C_{17}H_{34}$**)]$_2$,[N^+-(CH_2)$_2$-(**CH_2**)$_2$-(CH_2)$_2$-N^+)]$_2$); δ 1.8 (m, 12H, [CH_2-(**CH_2-N^+-CH_2**)-CH_2]$_3$); δ 3.1 (s, 18H, [N^+-(**CH_3**)$_2$]$_3$); δ 3.3 (m, 12H, [N^+-(**CH_2**)$_2$]$_3$).

(c) 18-N_4-18:

δ 0.9 (t, 6H, [**CH_3**-($C_{17}H_{34}$)]$_2$); δ 1.3 - 1.5 (m, 72H, [CH_3-(**$C_{17}H_{34}$**)]$_2$,[N^+-(CH_2)$_2$-(**CH_2**)$_2$-(CH_2)$_2$-N^+)]$_2$); δ 1.8 (m, 16H, [CH_2-(**CH_2-N^+-CH_2**)-CH_2]$_3$); δ 3.1 (s, 24H, [N^+-(**CH_3**)$_2$]$_3$); δ 3.3 (m, 16H, [N^+-(**CH_2**)$_2$]$_3$).

The ^{1}H NMR (400 MHz, MeOD) spectra exhibited peaks that are consistent with the above surfactant structures, suggesting successful synthesis of these templates.

4.2.2 X-ray powder diffraction

The phase purity of pristine ZSM-5, their desilicated derivatives and the surfactant-templated zeolites was examined using X-ray diffractometry. Figure 4.2 shows the XRD patterns of pristine ZSM-5 zeolites, with different SARs, synthesised at 150 °C for 48 h (using Aerosil 200 as silica source and TPA^+ as SDA).

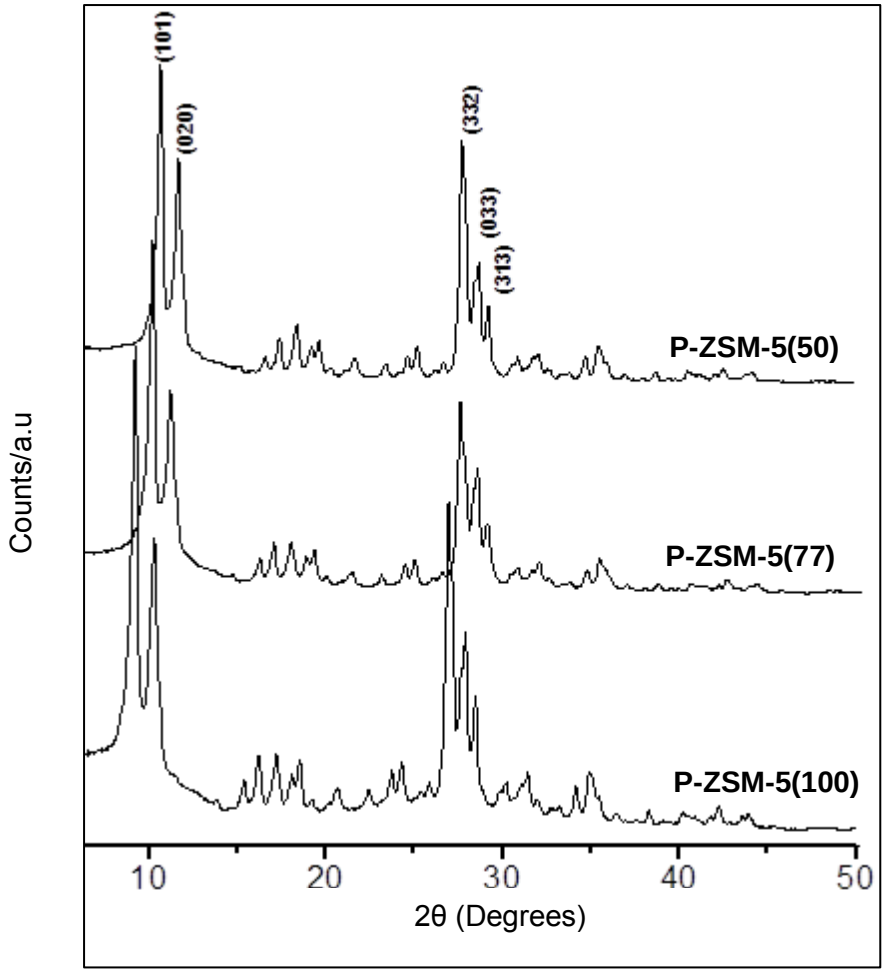

Figure 4.2 Powder XRD patterns of pristine ZSM-5 zeolites with different SARs synthesised at 150 °C for 48 h (using Aerosil 200 as silica source and TPA^+ as SDA).

As Figure 4.2 demonstrates, well-crystallised ZSM-5 zeolites were produced at three levels of SAR, *viz*., 50, 77, 100. This is evidenced by sets of intense peaks in ~ 7 - 12° and 25 - 30° 2θ ranges, which are characteristic of the MFI framework topology [2]. It is interesting to note that the peak intensities seem dependent on the SAR, increasing in the order 50 < 77 < 100. This observation suggests that the crystallinities of these materials increase with increasing SAR. There is a slight shift in peak positions to the left as the SAR of the zeolites increases, indicative of increased d-spacings (*i.e*., Braggs law). The following figure shows the XRD patterns of the desilicated ZSM-5 zeolites obtained by treatment of pristine ZSM-5 with 0.2 M NaOH at 65 °C for 30 minutes.

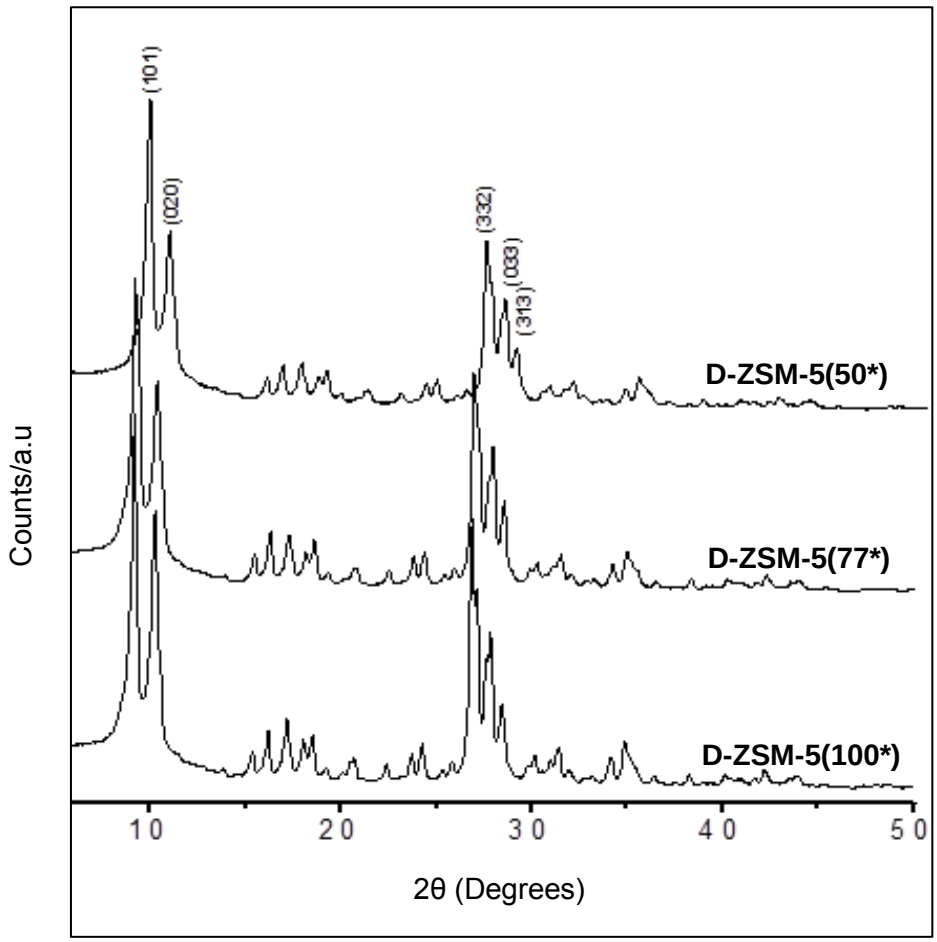

Figure 4.3 Powder XRD patterns of hierarchical zeolites obtained by desilicating pristine ZSM-5.

It can be seen in Figure 4.3 that after desilication, the pure ZSM-5 crystal structure is preserved. The peak positions of the characteristic peaks of the desilicated zeolites slightly shift to lower 2θ values as SAR increases. These peak positions are clearly summarised in the table provided in appendix A4. The observed shifts suggest minor structural readjustments in the materials. The relative % XRD crystallinity and crystallite sizes of both the pristine and desilicated zeolites are calculated as described below. The % crystallinity of the pristine and desilicated ZSM-5 materials is calculated by summing up the intensities of the characteristic peaks of ZSM-5 and dividing by the sum of the intensities of the corresponding peaks in the XRD pattern of the sample with the most intense peaks [3, 4]. That is, the P-ZSM-5(100) sample served as reference material or standard. Therefore, the formula in equation 4.1 [3] was adopted:

$$\%\ \text{Crystallinity} = \frac{\sum \text{intensities of characteristic peaks (sample)}}{\sum \text{intensities of characteristic peaks (reference)}} * 100 \quad \text{.....(4.1)}$$

The crystallite sizes of all samples were calculated using the Scherrer equation [4]:

$$L = \lambda / (\text{FWHM} * \text{Cos}\theta) \quad \text{.....(4.2),}$$

where L is the crystallite size, λ the wavelength of the X-ray radiation, FWHM is the full width at half maximum (in radians), and θ is the incident angle.

The calculated % crystallinity and crystallite size data for the investigated zeolites are given in Table 4.1.

Table 4.1 Influence of NaOH treatment on structural properties of ZSM-5 zeolites

Sample	% Crystallinity	Crystallite size (μm)
Pristine zeolites		
P-ZSM-5(50)	43	2.9
P-ZSM-5(77)	47	2.7
P-ZSM-5(100)	100	2.4
Desilicated zeolites		
D-ZSM-5(50*)	44	2.1
D-ZSM-5(77*)	47	2.2
D-ZSM-5(100*)	83	1.9

The % XRD crystallinity of both pristine and desilicated ZSM-5 materials increases as the SAR increases in the sequence 50 < 77 < 100. This may suggest that the increase in the siliceous character of zeolite materials as SAR increases, leads to an increase in % XRD crystallinity [5]. The pristine ZSM-5 materials with lower SARs (50 and 77) retained their % XRD crystallinity, while the zeolite with SAR of 100 undergoes a notable loss (17%) in crystallinity upon desilication. This decrease in the % XRD crystallinity upon desilication can be due to amorphisation of the zeolite, resulting in a loss of crystallinity [6]. Also shown in Table 4.1 are the average

crystallite sizes of both classes of zeolites. There is a slight decrease in crystallite size (*i.e.*, from 2.9 through 2.7 to 2.4 μm) as the SAR of the pristine zeolites increases. The information on the crystallite sizes of the desilicated zeolites shows a difference of 0.5 - 0.8 μm from their pristine counterparts, but stays constant within experimental error as SAR is varied from 50* to 100*.

The XRD analysis was also carried out on the three hierarchical zeolites synthesised at 150 °C for 96 h using polyquaternary ammonium surfactants. Figure 4.4 shows the XRD patterns of these zeolites.

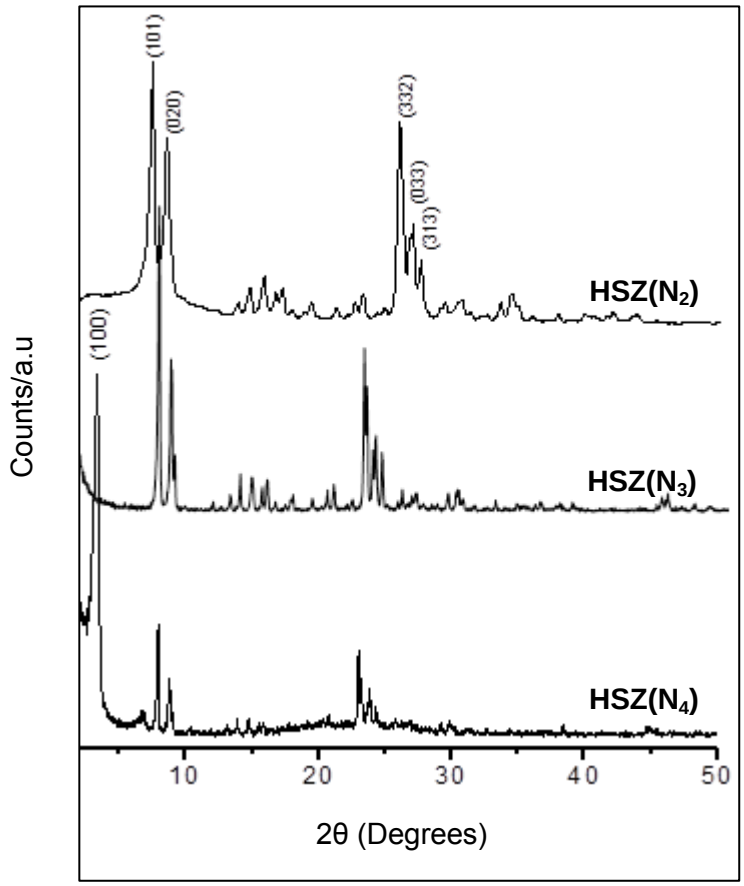

Figure 4.4 XRD patterns of hierarchical ZSM-5 zeolites synthesised at 150 °C for 96 h using different polyquaternary ammonium surfactants as templates.

The XRD patterns of the surfactant-templated zeolites contain intense reflections characteristic of the ZSM-5 crystal structure in the wide-angle XRD region (Figure 4.4), which confirms the successful synthesis of MFI-type zeolites. In the case of 18-N_2 as SDA, the XRD pattern of the resulting zeolite exhibits broader Bragg diffraction lines. Also, the peak positions are closely related to that of a typical pristine ZSM-5

shown in Figure 4.2. On the other hand, when 18-N_3-18 was used as the zeolite structure-directing agent, the XRD pattern of the resulting material shows reflections of very narrow lines compared to that produced using 18-N_2. The peaks also tend to shift to lower 2θ values, particularly those in the range 20° ≤ 2θ ≤ 30°. The two XRD patterns [Figure 4.4, HSZ(N_2) and HSZ(N_3)] only show pure MFI zeolitic materials with no evidence of mesoporous features. On the other hand the zeolite obtained using 18-N_4-18 surfactant as template shows an intense peak in the low-angle XRD region (2θ < 5°). The most intense low-angle peak at *ca.* 3º 2θ and indexed (100), corresponds to a mesoscale lattice of 2-D hexagonal symmetry, similar to that of the MCM-41 material [7]. The appearance of this peak together with the MFI characteristic peaks signals the co-existence of micro- and meso-pores in the zeolite produced by this surfactant template. Similar observations of the appearance of the (100) peak in the XRD patterns of hierarchical zeolites were reported by Lui *et al*. [8] and Na *et al.* [1], upon using different types of polyquaternary ammonium surfactants as structure-directing agents. The shifting of peak positions to lower 2θ is indicative of increased d-spacing. It can also be noted that as the number ammonium centres on the surfactant used increases, the XRD peaks tend to narrow, suggesting an increase in the crystallite sizes. To complement the XRD patterns in Figure 4.4 above, the calculated % crystallinity and crystallite size data for the investigated surfactant-templated hierarchical zeolites are given in Table 4.2.

Table 4.2 The relative % XRD crystallinity and average crystallite size data for the zeolites

Sample	% XRD Crystallinity*	Crystallite size (μm)
P-ZSM-5(100)	100	2.4
HSZ(N_2)	51	1.6
HSZ(N_3)	78	1.9
HSZ(N_4)	61	2.4

*Pristine ZSM-5(100) used as a reference material in calculating the relative crystallinity of the surfactant-templated hierarchical zeolites (through equation 4.1).

The relative % XRD crystallinity of the surfactant-templated zeolites is generally >50%, and seems to increase with the increase in the number of quaternary ammonium centres contained in the surfactant templates used. However, this increase does not correlate systematically with the number of ammonium centres in the surfactant frameworks, showing a breakdown from 3 ammonium centres. Notably, these relative % XRD crystallinities are generally greater than that of the pristine ZSM-5 materials, with the reference material, P-ZSM-5(100), being an exception. This might be due to longer crystallisation period used for these zeolite materials (*i.e.,* 96 h), in addition to the presence of multiple zeolite structure-directing quaternary ammonium groups in surfactant templates. The crystallite sizes of the three surfactant-templated zeolites increase as the number of ammonium centres in the surfactants increases. This agrees well with the observation made in their XRD patterns in Figure 4.4, showing narrower peaks upon increasing number of ammonium centres in the surfactant.

4.2.3 Fourier-transform infrared spectroscopy

Fourier transform infrared spectroscopy was used to study the protonated forms of pristine, desilicated and surfactant-templated zeolites in order to elucidate their acidic and structural properties. Since the XRD analysis has already confirmed the presence of the ZSM-5 framework topology for all materials prepared in this work [Figure 4.2 - 4.4], the FT-IR spectra of the samples were only recorded in the range between 550 and 4000 cm^{-1}. Figure 4.5 shows the FT-IR spectra of pristine ZSM-5 synthesised to three different nominal SARs.

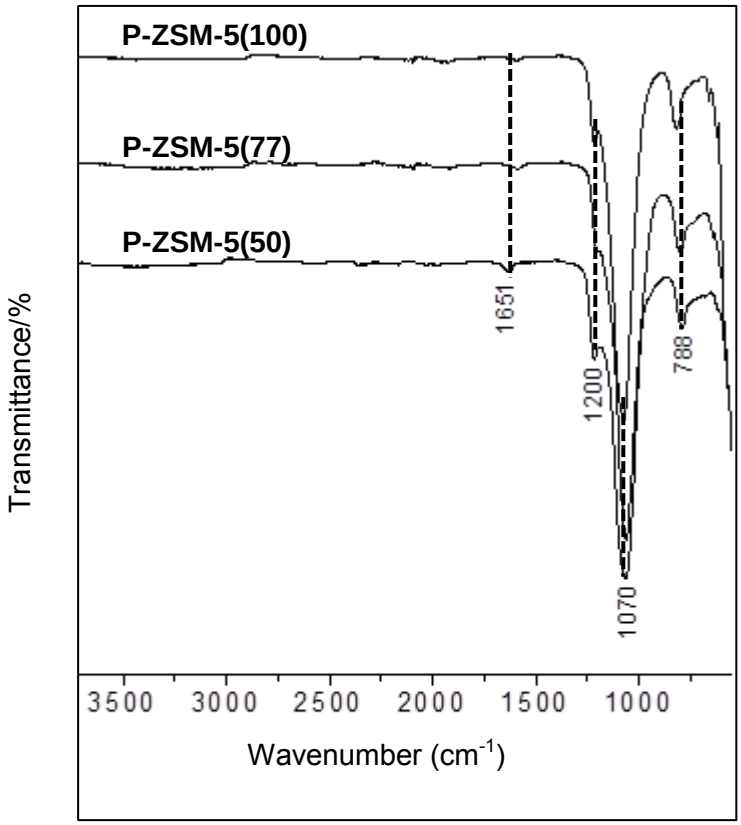

Figure 4.5 Infrared spectra of the pristine zeolites synthesised at 150 °C for 48 h (using Aerosil 200 as silica source and TPA^+ as SDA).

The spectra in Figure 4.5 show predominantly lattice vibrations characteristic of H-ZSM-5 zeolite in the range of 550 - 1200 cm^{-1} [9, 10]. All pristine H-ZSM-5 zeolites show a strong band around 1070 cm^{-1} with a pronounced shoulder at 1200 cm^{-1}, and assigned to the T-O-T (T = Si or Al) asymmetric stretching vibrational modes, with Al-O-Al linkages forbidden by Lowenstein rule [9 - 11]. Also observed in these three zeolites is a lower intensity peak at 788 cm^{-1}, which is due to the Si-O-Si symmetric stretching vibrational mode with a Si-O-Si in-plane bending character. It is surprising that all spectra in Figure 4.5 do not show peaks in the hydroxyl (OH) region, which is often an intrinsic characteristic of hydrated materials. An instrumental artefact can be ruled out because such peaks are observable on these materials upon alkaline treatment elsewhere in this section (see Figures 4.6 and 4.7]. The value of this spectral region in zeolite chemistry is that it allows elucidation of Brønsted acidity associated with structural OH groups [12 - 17]. The absence of these peaks in the figure above may suggest little or no Brønsted acidity in the original materials

prepared in this work, though the hydrocracking results in section 4.3.1 suggest otherwise.

Figure 4.6 shows FT-IR spectra of H-ZSM-5 zeolites prepared by desilicating the pristine materials discussed above through an alkaline treatment method.

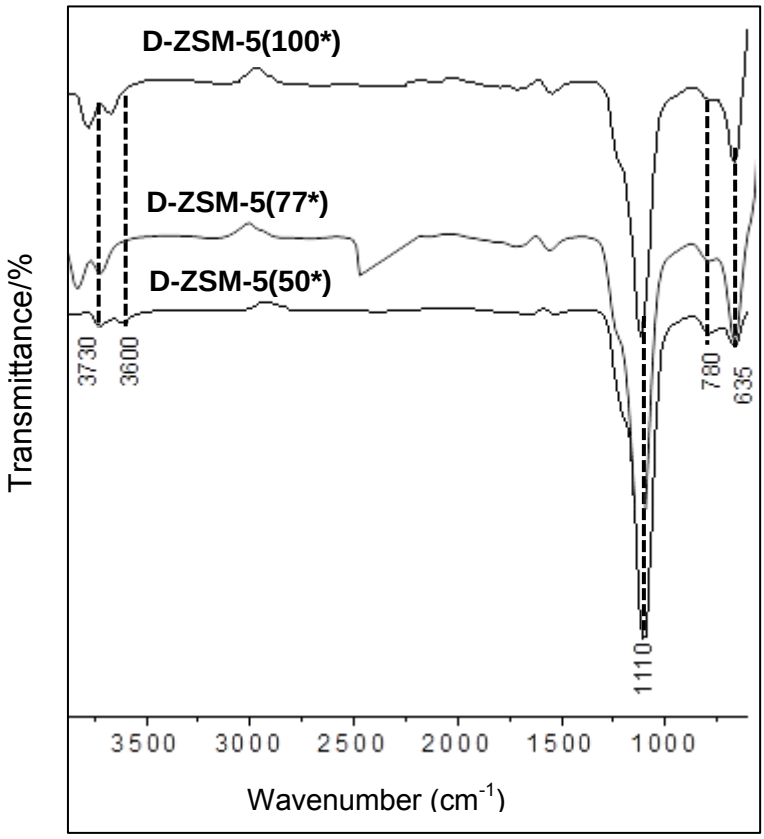

Figure 4.6 Infrared spectra of ZSM-5 zeolites prepared by desilication of pristine versions.

Similarly with the pristine counterparts of these zeolites, the lattice vibrations are present in the IR spectra. The strong band around 1110 cm^{-1} slightly shifts to higher wavenumbers (1121 and 1132 cm^{-1}) as the SAR increases from 50* to 100* due to different Al content in the zeolites. In agreement with this statement, it has been reported that the maximum of the T-O-T asymmetric stretching band in silica-based materials is sensitive to the Al content in the framework and is shifts to higher wavenumbers when the Al content increases [13]. Unlike the pristine H-ZSM-5 zeolites (Figure 4.5), the desilicated samples show a two-band stretching vibration in the range 3500 - 3800 cm^{-1} (Figure 4.6). The presence of these bands suggests the existence of Brønsted acidity in these zeolites, induced by the desilication treatment. Similar two-band spectra are also reported in the literature [13, 17]. In the hydroxyl

region, the vibration of the bridging OH group from Brønsted acid sites in H-ZSM-5 shows a shift from 3600 to 3612 and 3618 cm^{-1} as SAR increases. The observed shift in peak positions may suggest different acidities in the resulting materials. The extent of this shift to higher wavenumbers corresponds to high SAR (*i.e., high acid strength*) [16]. In line with this statement, the shift observed in Figure 4.6 correlates well with the respective SARs. The band at 3730 cm^{-1} is due to the O-H stretching of the terminal silanol groups located at the external zeolite surface [13 - 15], while that at 3600 cm^{-1} is due to bridging OH groups, which account for the Brønsted acidity of zeolites.

Figure 4.7 shows the FT-IR spectra of hierarchical zeolites synthesised hydrothermally using polyquaternary ammonium surfactants.

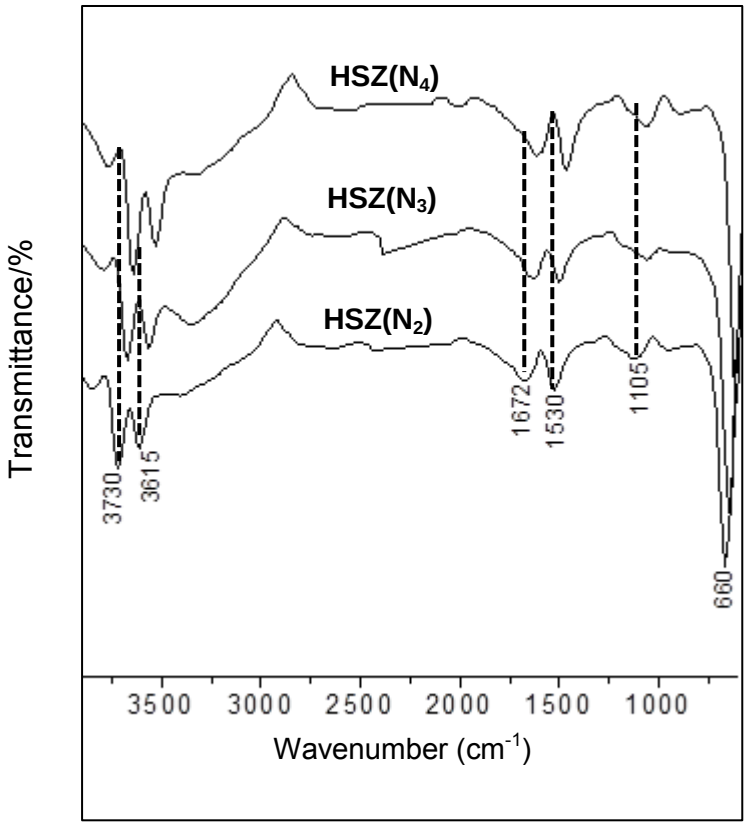

Figure 4.7 Infrared spectra of hierarchical MFI zeolites synthesised at 150 °C for 96 h using polyquaternary ammonium surfactants as templates.

All surfactant-templated zeolites show similar FT-IR features in both framework and hydroxyl regions of spectra. There are striking differences between IR features of conventional and hierarchical zeolites. For example, the most intense peak at 1110 cm^{-1} is lower in intensity compared to the pristine and desilicated zeolites. The peaks

tend to shift to the right (*i.e.*, lower frequencies) as the number of quaternary ammonium centres in the templates increases. This shift of peak positions to lower frequencies is more pronounced in the OH region of the spectra. The highly intense hydroxyl peaks between 3500 and 3800 cm^{-1} suggest the presence of a high content of Brønsted acid sites. It can be inferred (*on the basis of peak intensity*) that hierarchical zeolites synthesised in this work are more acidic than zeolites prepared through a post-synthesis desilication route (Figure 4.6), regardless of their different SARs. Notably, there are two intense bands at 1530 and 1672 cm^{-1}, which can be assigned to H-OH bending vibrations (symmetrical and asymmetrical, respectively) vibration of the "possible" adsorbed water molecules [13]. Another noteworthy infrared feature that marks the difference between conventional MFI and surfactant-templated MFI zeolite is the appearance of OH peaks in the latter, while the former only exhibited these peaks after desilication in alkaline media.

4.2.4 Scanning electron microscopy

Scanning electron microscopy was used to elucidate the morphology of zeolitic materials prepared in this work. The response of the surface morphology to the composition and alkaline-mediated desilication of the pristine zeolites is illustrated by the corresponding SEM micrographs in Figure 4.8.

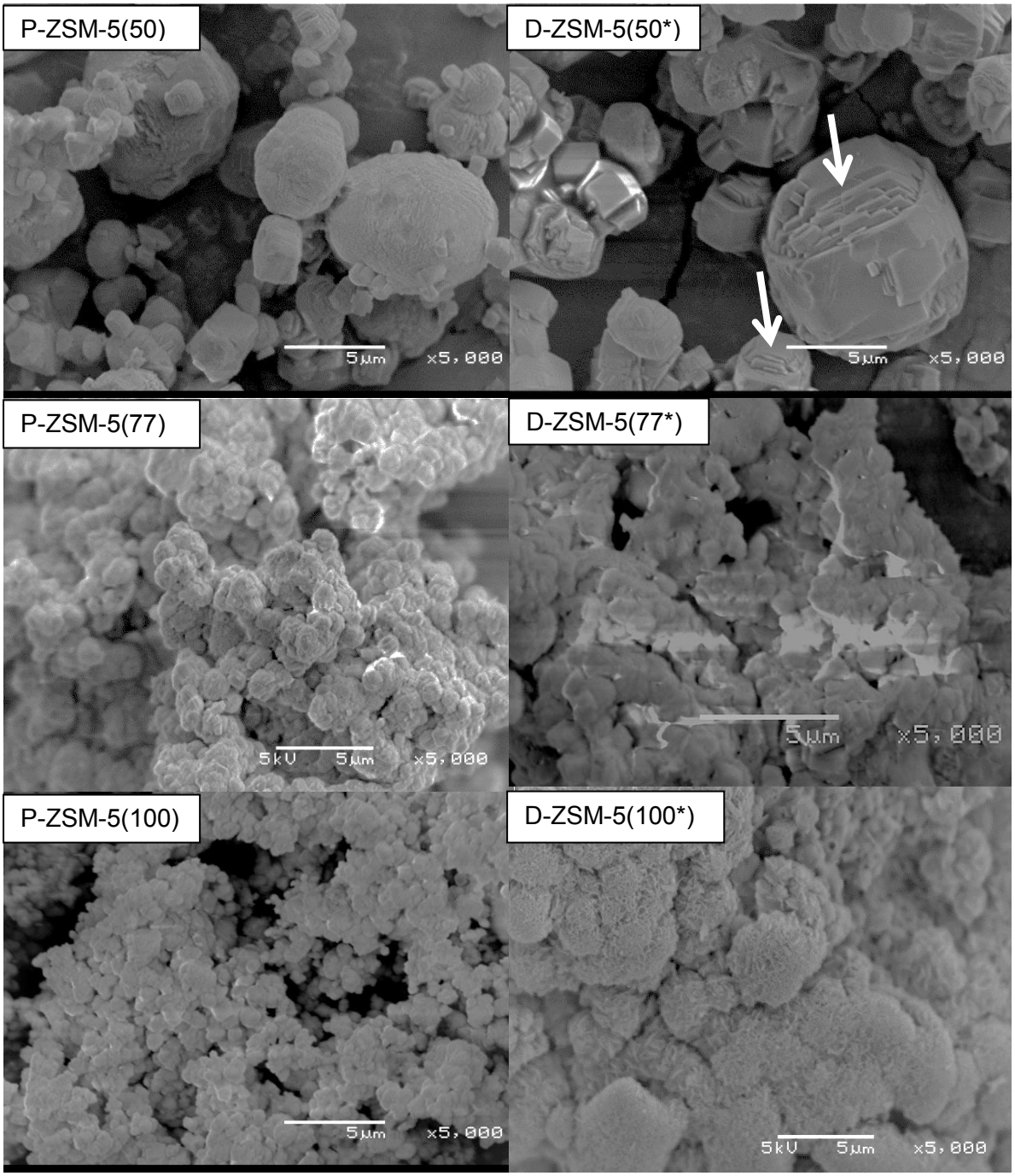

Figure 4.8 SEM images of the pristine ZSM-5 zeolites with different SARs, and their desilicated counterparts. Arrows point at flat slabs stacked vertically inside the “hatched” shell.

The micrograph of the pristine ZSM-5(50) shows a predominant morphology of large and small spheroids, together with some ill-defined cubic shapes, similar to those reported elsewhere [16]. After desilication, the zeolite did not retain the original morphology entirely, showing hexagonal prismatic crystals with twinning occurring in other areas and large spheroids “hatching” to reveal their contents upon treatment.

The contents of these spheroids are flat slabs stacked vertically inside the “hatched” shell [*pointed by the arrows in Figure 4.8, micrograph D-ZSM-5(50*)*]. This may be a result of cleavage of the silica shell of the large spheroids of the pristine zeolite by the alkaline solution used in the desilication treatment. To the best of our knowledge, such an observation has not been reported upon desilication of MFI zeolites. The micrograph of ZSM-5(77) zeolite shows nanocrystals which appear to agglomerate both before and after desilication. Similar to the observation with pristine ZSM-5(77), the morphology of pristine ZSM-5(100) also consists of nanocrystals which appear to agglomerate [4, 6]. Upon desilication of ZSM-5(100), the micrograph of the resulting zeolite shows crystals which grow to larger spheroids held together by an amorphous material phase. It is apparent in Figure 4.8 that the desilicated ZSM-5 derivatives did not completely retain the morphology of the pristine zeolites.

The morphologies of surfactant-templated MFI zeolites are illustrated by SEM micrographs in Figure 4.9.

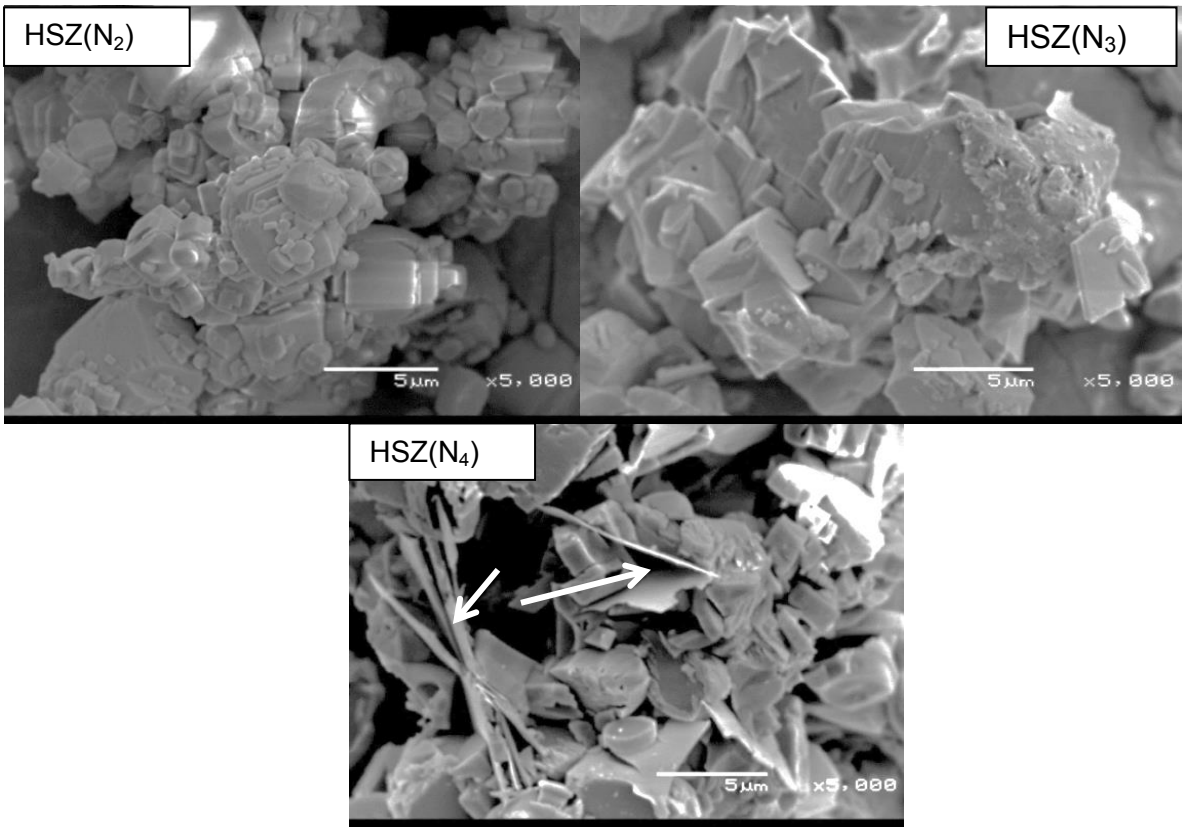

Figure 4.9 SEM of hierarchical zeolites synthesised at 150 °C for 96 h using polyquaternary ammonium surfactants as templates. Arrows in HSZ(N_4) indicate the plate-like morphology in the micrograph.

The micrograph of the hierarchical zeolite synthesised using 18-N_2 as SDA shows a morphology consisting of smaller particles attached to the surface of a larger particle with a mixture of spheroidal, cubic, rectangular and prismic shapes. Crystal twinning or intergrowth is apparent in this zeolite sample. When 18-N_3-18 is used as SDA in place of 18-N_2, the material exhibits a highly irregular morphology with lumps of closely packed crystals, including hexagonal prisms and some flat slabs. The micrograph of 18-N_4-18 surfactant-templated zeolite shows plate-like and irregular micrometre-sized crystals. Similar crystals with very thin plate-like morphology, typical of a nanosheet material, have been observed elsewhere using a different template [18]. However, in this case the morphology is not uniform since some ill-defined cubic crystals are observable

4.2.5 N_2 adsorption analysis

Nitrogen adsorption isotherms of conventional ZSM-5 materials before and after desilication are shown in Figure 4.10.

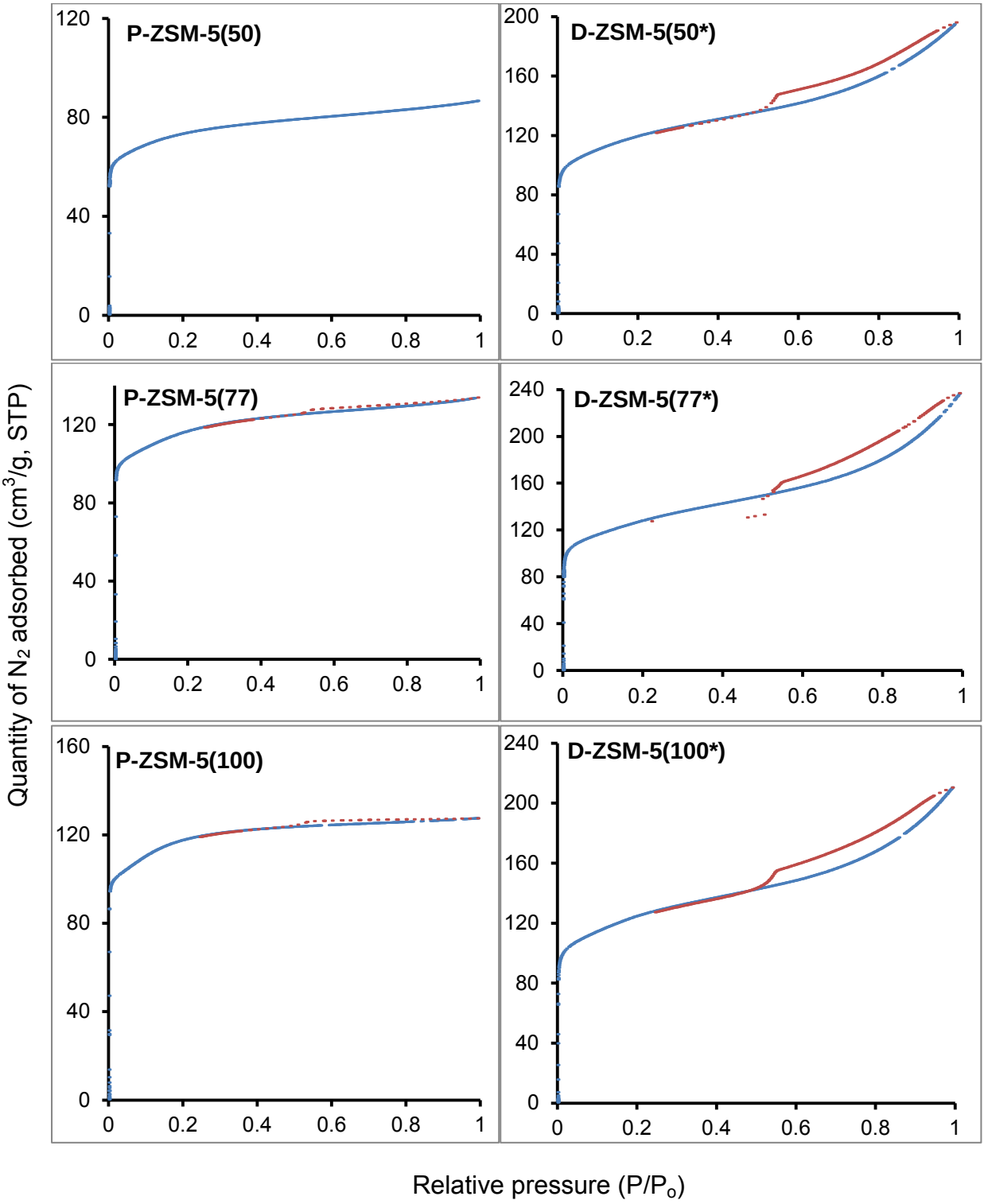

Figure 4.10 N_2 adsorption isotherms of pristine and desilicated ZSM-5 zeolites with different SARs.

All the pristine ZSM-5 materials exhibit a Type I isotherm with a high N_2 uptake at low relative pressures, confirming their microporous character [19]. Interestingly, alkaline treatment of the ZSM-5 zeolites lead to isotherms of both Type I and IV

behaviour. This is illustrated by a remarkable uptake of N_2 at higher relative pressures, accompanied by a hysteresis loop suggesting the simultaneous presence of micro- and meso-pores in the zeolite samples as reported in the literature [19, 20]. Bothe types of zeolites (treated and non-treated) show an increase in nitrogen uptake as SAR varies in the order 50 < 100 < 77. Comparison of the pristine ZSM-5(50) and its derivative ZSM-5(50*) shows that at a low relative pressure ($P/P_o = 0$), the former adsorbs ~60 cm^3/g, while the latter adsorbs up to 98 cm^3/g of N_2. This suggests the ability of the alkaline-treatment to enhance the porosity of the zeolite and consequently increase the adsorption capacity. In contrast, the pristine zeolites with SAR of 77 and 100 showed no significant difference in the quantity of N_2 adsorbed (at $P/P_o = 0$) compared to their derivatives. At $P/P_o \geq 0.5$, the nitrogen adsorption isotherms of the desilicated ZSM-5 materials show distinct hysteresis loops, while the pristine materials show a plateau at higher relative pressures (*the result of uniform micropores and absence of larger pores*). The observed changes in the isotherms confirm that desilication induced mesopores within the microporous zeolite matrix, and therefore, allowed production of hierarchical ZSM-5 by the post-synthesis approach. The desilicated zeolite with SAR of 77* showed the highest N_2 adsorption capacity, giving the order 77* > 100* > 50* for this series. The Further properties of these materials derived from nitrogen adsorption isotherms are summarised in Table 4.3.

Table 4.3 Textural properties of the pristine and their desilicated derivatives

Sample	S_{BET} (m^2/g)	Pore volume (cm^3/g)	Pore diameter (nm)
Pristine zeolites			
P-ZSM-5(50)	114	0.13	2.9
P-ZSM-5(77)	150	0.19	2.6
P-ZSM-5(100)	170	0.21	2.3
Desilicated zeolites			
D-ZSM-5(50*)	378	0.37	4.8
D-ZSM-5(77*)	403	0.30	4.4
D-ZSM-5(100*)	330	0.32	4.4

The surface area of the pristine ZSM-5 materials increases with increasing SAR, as does the pore volume. It is observed that the NaOH-treated zeolites possess higher surface areas and pore volumes compared to their pristine counterparts. This is an indication of enhanced pore properties as a result of NaOH treatment. Therefore, it may be concluded that treating pristine ZSM-5 materials with NaOH, readjusts the pore volume of the zeolite and BET surface area (S_{BET}). Another observed trend in the desilicated zeolites is that as the SAR increases, the pore volume decreases slightly, which is an opposite trend to that observed in the related pore diameter. In general, the textural properties of pristine ZSM-5 are significantly improved by the desilication treatment, which is an interesting finding in view of maximal structural retention after treatment (see XRD patterns in Figures 4.2 and 4.3).

Figure 4.11 shows N_2 adsorption isotherms of surfactant-templated hierarchical ZSM-5 zeolites.

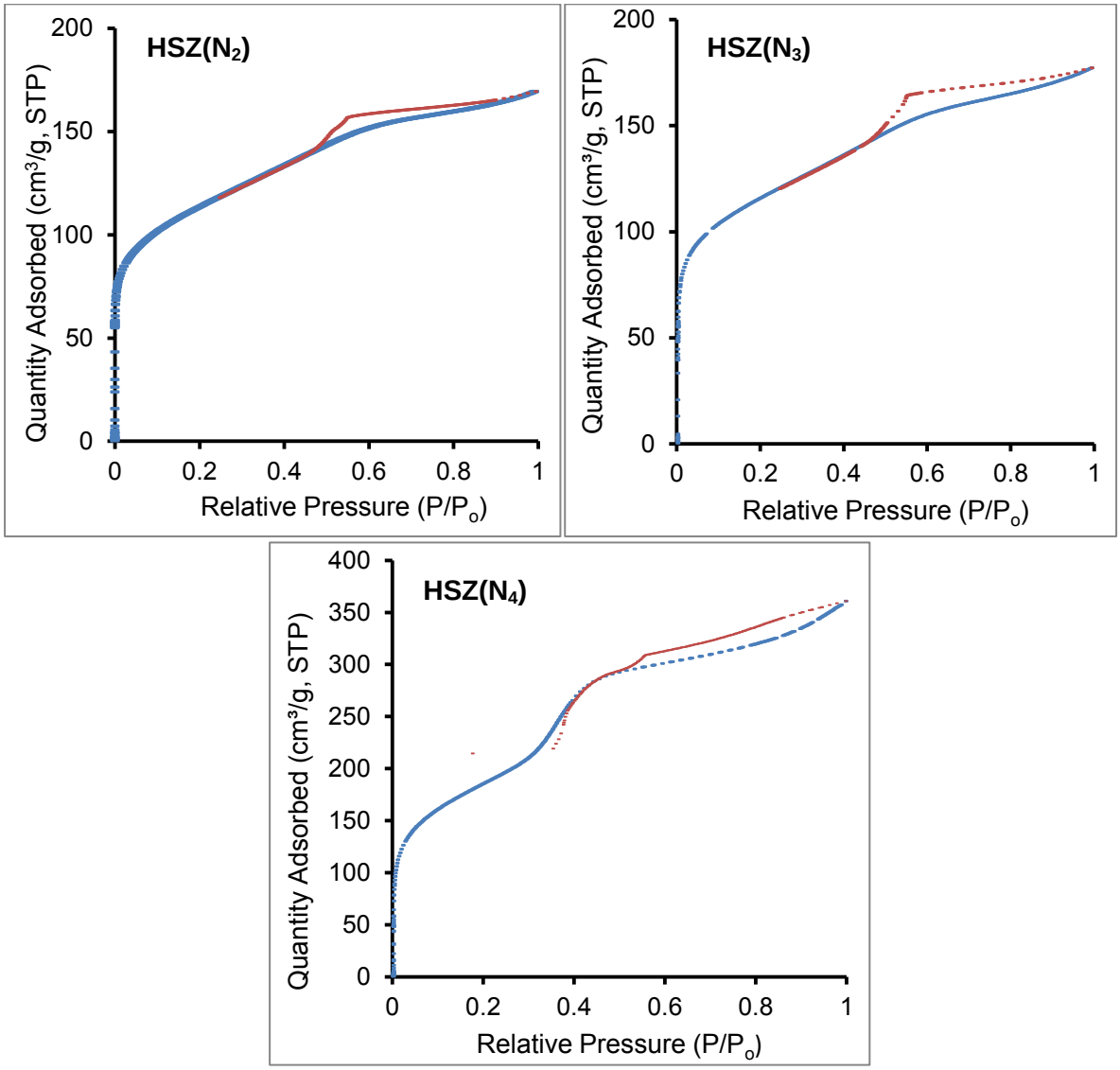

Figure 4.11 N_2 adsorption isotherms of surfactant-templated hierarchical zeolites.

In this figure, the N_2 adsorption isotherms of three hierarchically-structured ZSM-5 zeolites are arranged according to the number of quaternary-ammonium groups present in each surfactant template, *viz*., 2, 3 and 4. The overall observation is that all surfactant-templated hierarchical zeolites show a steep rise in N_2 uptake in the range $0.0 < P/P_o < 0.1$, corresponding to filling of micropores [20]. These three samples show a combination of Type I and IV isotherms, which is characteristic of hierarchical porous systems. It is worth noting the inflections at intermediate relative pressures ($P/P_o = 0.3$ and 0.5) in the isotherm of the HSZ(N_4) material, indicative of capillary condensation of nitrogen in the mesopores [21]. The N_2 adsorption results confirm the presence of both micropores and mesopores in the synthesised hierarchical zeolites. At high relative pressures, the N_2 uptake increases with

increasing number of ammonium centres in the surfactants used as SDAs in the order: HSZ(N_2) < HSZ(N_3) < HSZ(N_4). A summary of the textural properties of these hierarchical zeolites is shown in Table 4.4.

Table 4.4 Textural properties of polyquaternary ammonium surfactant-templated hierarchical ZSM-5 zeolites.

Sample	S_{BET} (m^2/g)	Pore volume (cm^3/g)	Pore diameter (nm)
HSZ(N_2)	140	0.18	3.3
HSZ(N_3)	419	0.26	3.8
HSZ(N_4)	1090	0.57	4.0

The surface areas of the hierarchical zeolites are strongly influenced by the nature of surfactant used in their synthesis. As the data in Table 4.4 shows, an increase in the number of ammonium centres in the surfactant leads to the higher the BET surface area of the resulting zeolitic material. In the case where 18-N_2 was used as the SDA, the surface area is 140 m^2/g, which is closer to that obtained for the bulk ZSM-5 zeolites used in this work. When 18-N_3-18 was used as the SDA, the surface area of the zeolite increased by a factor of 3 (419 m^2/g) from when 18-N_2 was used. Very remarkable is the extremely high BET surface area of the zeolite sample templated using 18-N_4-18, containing 4 ammonium centres, *i.e.*, 1090 m^2/g. This surface area is approximately 7 and 2 times larger than those obtained when 18-N_2 and 18-N_3-18, respectively, were used as templates. The observed S_{BET} when 18-N_4-18 was used as template is consistent with the XRD pattern of this hierarchical zeolite, which confirmed mesoporosity by the appearance of the (100) peak at 3° 2θ. This is analogous to the typical surface area of a mesoporous material (*e.g.*, MCM-41), with ~1000 m^2/g [6]. It is observed that as the surface area of the surfactant-templated zeolites increases, the pore volumes and pore sizes also increase. For these systems, the attractive and catalytically beneficial properties seem to be dependent on the number of ammonium centres in the structure-directing surfactant.

4.3 Catalytic activity test

This research is part of a major project that seeks to enhance the diesel selectivity of the FTS through integration of LTFT and wax hydrocracking into one process unit. However, this dissertation focuses only on the hydrocracking part, under conditions relevant to LTFTS, through the design and synthesis of hierarchical zeolite-based catalysts. The zeolites used and reported in this study were synthesised according to procedures described in Chapter 3. They were subsequently tested for their efficiency as acidic supports for Pd nanoparticles when these systems were used as catalysts in the hydrocracking of *n*-hexadecane as a model LTFT wax component. One of the challenges facing the hydrocracking catalyst under FTS conditions is the co-presence of H_2O and CO [22] in the product stream. Therefore, since the ultimate objective is the hydrocracking of LTFT wax, the influence of co-feeding H_2O and CO as typical by-products of the FTS on the performance of the catalysts was studied. Zeolite-based catalysts were packed into a trickle-bed reactor described in Chapter 3. Two types of experimental runs were carried out, *viz*., standard (Std) hydrocracking (*involving H_2 and n-C_{16} as feedstock*) and non-standard hydrocracking (*involving co-feeding H_2O and CO with the feedstock*). The feedstock conversion data reported in this work represent the steady-state activity of the catalyst system at a specific reactor temperature after repeated runs.

4.3.1 Hydrocracking of *n*-C_{16} over conventional ZSM-5 based catalysts

The catalytic tests were conducted over both pristine and desilicated ZSM-5 based catalysts. The hydrocracking activity of each catalyst is represented by a plot of *n*-C_{16} conversion (χ) against the reactor temperature. To determine if the catalyst exhibits ideal or non-ideal behaviour, the plot of C_4/C_{12} ratio versus χ (*n*-C_{16}) was used. The product distribution profiles, expressed as plots of product selectivity versus carbon number of the specific product, are also used to qualify the catalytic performance. For each catalyst, the chosen product distribution profile from a specific run was taken at the last reactor temperature as representative. In the case of *n*-C_{16} feed used in this work, an ideal hydrocracking behaviour will be characterised by the C_4/C_{12} = 1 and a non-ideal behaviour by the C_4/C_{12} > 1, where the latter is indicative of secondary cracking of products [23]. This concept was arbitrarily defined as the ratio between the mass fraction of the “light” C_4 and “heavy”

C_{12} fragments [3] as encountered during the conversion of *n*-hexadecane. In order to avoid clustering of data points in the plots, the results for each catalyst are plotted and discussed individually, rather than superimposed with their counterparts.

Figure 4.12 shows the plots of χ (*n*-C_{16}) as a function of the reactor temperature and the C_4/C_{12} ratio versus χ (*n*-C_{16}) in the hydrocracking of *n*-C_{16} the over 0.9 wt.% Pd/P-ZSM-5(50) catalyst.

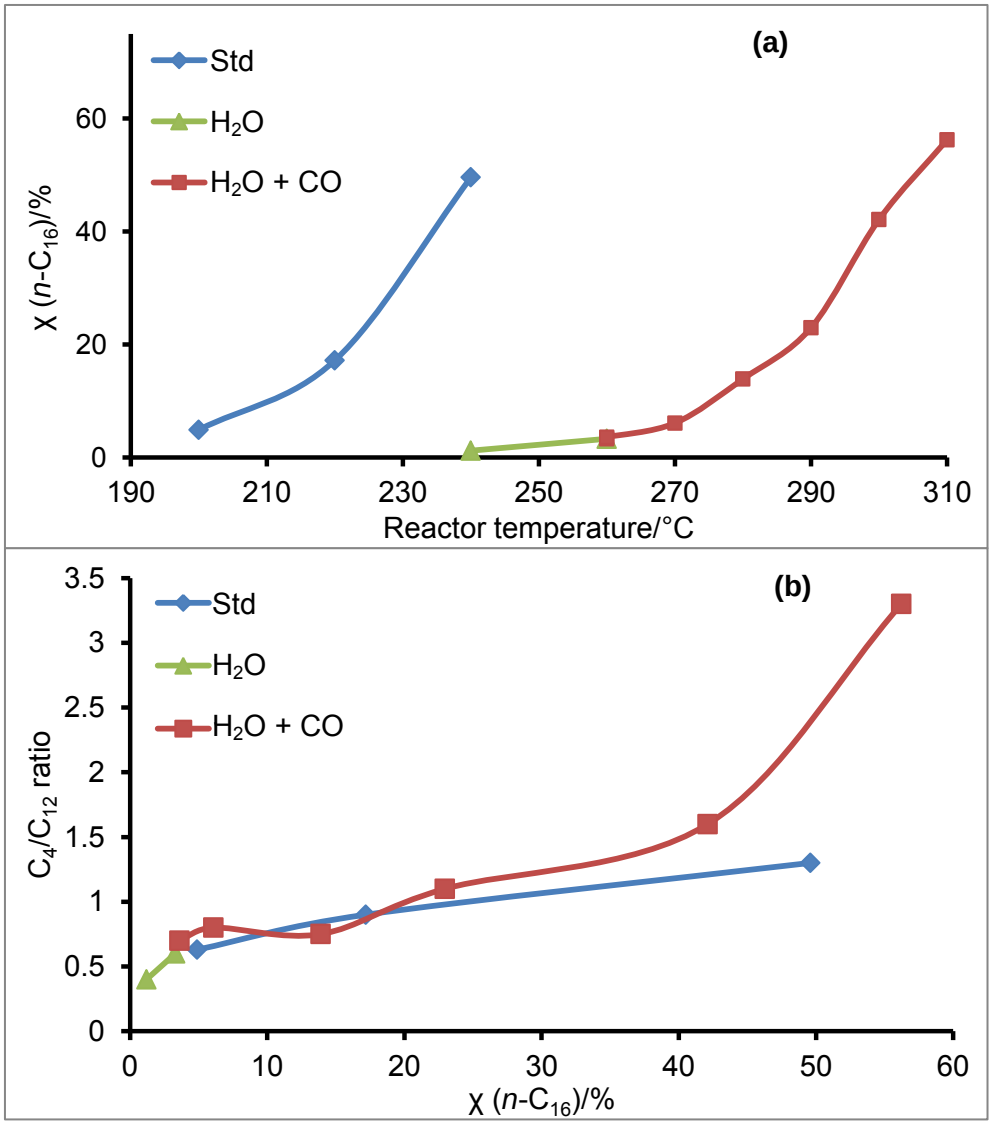

Figure 4.12 The catalytic performance of 0.9 wt.% Pd/P-ZSM-5(50) catalyst in the hydrocracking of *n*-C_{16}: (a) χ (*n*-C_{16}) v/s reactor temperature and (b) C_4/C_{12} product ratio v/s χ (*n*-C_{16}).

The standard run on this catalyst system shows that the conversion increases with reactor temperature [Figure 4.12(a)]. However, within the chosen temperature range

(200 - 240 °C, typifying LTFT range), this catalyst is still far from reaching 100% conversion, only attaining a conversion of 48% at 240 °C, *i.e*., it shows poor catalytic performance for this reaction. Upon co-feeding H_2O and CO after reaching steady state performance at 240 °C, a significant drop in conversion from 48 to 2% was observed. This decrease in conversion after co-feeding H_2O and CO may be attributed to the poisoning effect on the catalyst brought about by the co-fed reactants. In other words, co-feeding H_2O and CO suppresses the catalytic activity of this catalyst system. Notably, the catalytic performance of this catalyst in the presence of H_2O and CO shows an increasing trend with further increases in temperature (thus taking this experiment into the high-temperature FT regime, which is not the focus of this research). This increased conversion at high temperatures may be attributed to contributions from the thermal cracking component, because high temperatures are known to promote thermal cracking [24]. The corresponding plots of the C_4/C_{12} ratio versus *n*-C_{16} conversion [Figure 4.12(b)] show that the catalyst does not show ideal hydrocracking behaviour at each conversion level attained in this experiment, because $C_4/C_{12} \neq 1$. The observed increase in C_4/C_{12} ratio as a function of *n*-C_{16} conversion is more pronounced in the presence of the co-fed reagents than in the standard run, signalling the presence of secondary cracking [24]. Also, the non-ideal behaviour of this catalyst, suggested by $C_4/C_{12} \neq 1$ in Figure 4.12(b), is supported by the product distributions illustrated in Figure 4.13 below.

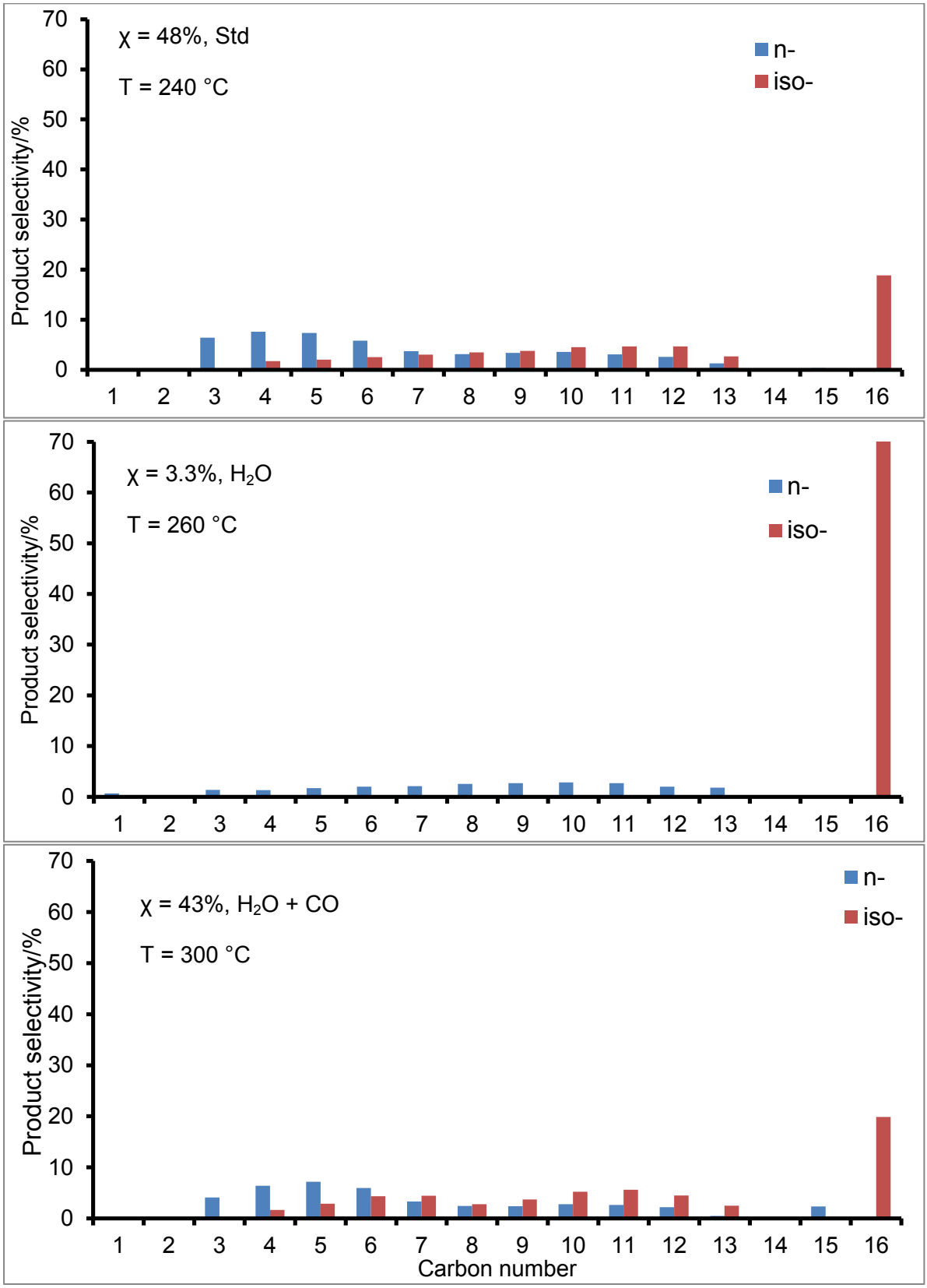

Figure 4.13 The cracked product distributions for standard and non-standard hydrocracking of *n*-C_{16} over the 0.9 wt.% Pd/P-ZSM-5(50) catalyst. The *n*- and *iso*- prefixes denote normal and isomerised products.

The cracked product distribution profiles of Pd-based hydrocracking catalysts derived from pristine ZSM-5 with a SAR of 50 generally showed a dual distribution of paraffinic products, *i.e.,* defines a two-hump profile. However, only the distribution from *n*-C_{16} hydrocracking at 240 °C is shown as representative in Figure 4.13. The dominance of lighter paraffinic products is also an indicator of secondary cracking, thus confirming a non-ideal behaviour implied by the C_4/C_{12} plots in Figure 4.12(b). Interestingly, the *iso*-paraffinic products are skewed to higher carbon numbers, and include relatively significant amounts of *iso*-C_{16}. This can be a desirable feature when diesel is the sought-for product, because *iso*-paraffins improve cold-flow properties of diesel [25]. However, co-feeding FT reactor outlet gases (H_2O + CO) changed the distribution of cracked products as shown for a reactor temperature of 300 °C. While the *n*-paraffins are produced favourably in the lower carbon number range (C_3 - C_8), the *iso*-parrafins show a dual distribution centred around C_8, with the higher carbon number products dominating over their lower counterparts, in addition to *iso*-C_{16}.

A similarly prepared catalyst involving a zeolitic support with a higher SAR than that used above, *viz*., 0.9 wt.% Pd/P-ZSM-5(77), was also investigated for catalytic performance in the hydrocracking of *n*-hexadecane (see Figure 4.14).

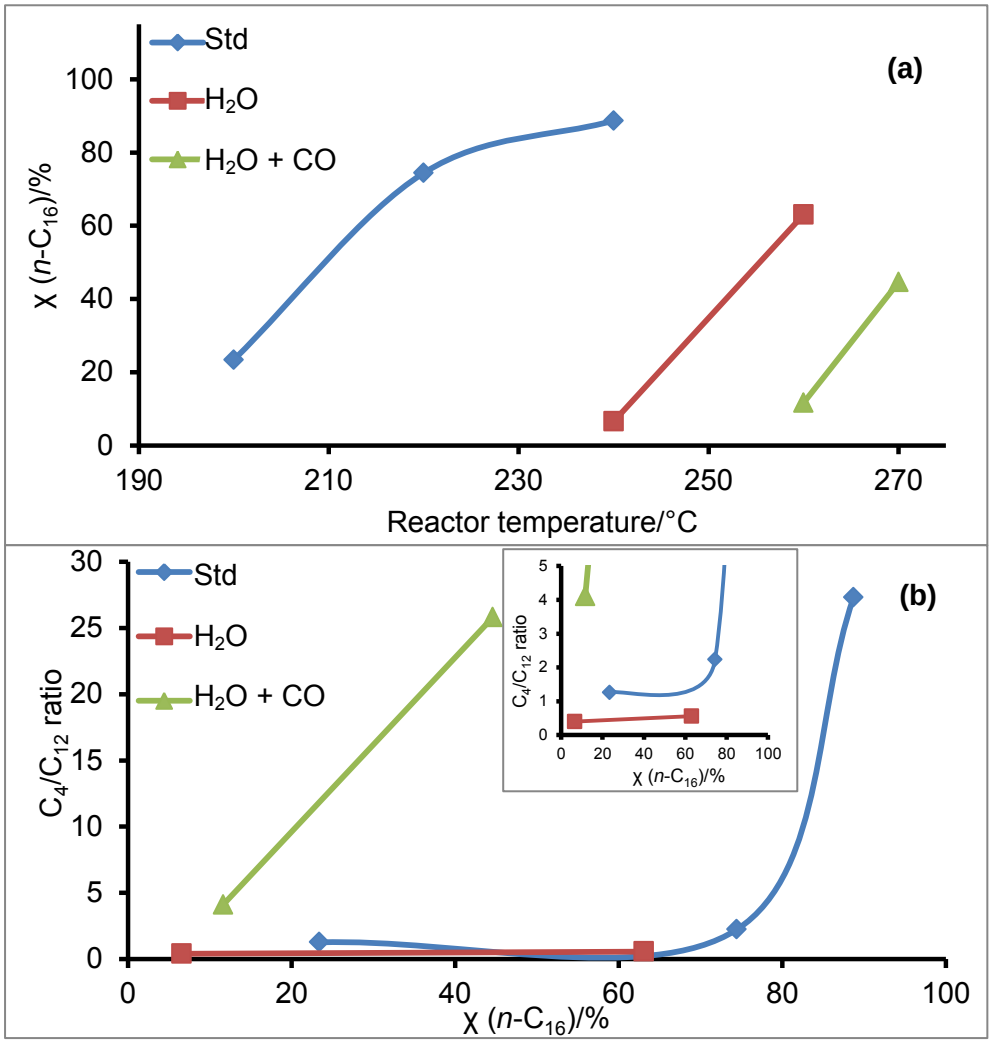

Figure 4.14 The catalytic performance of 0.9 wt.% Pd/P-ZSM-5(77) catalyst in the hydrocracking of *n*-C_{16}: (a) χ (*n*-C_{16}) v/s reactor temperature and (b) C_4/C_{12} product ratio v/s χ (*n*-C_{16}). The inset shows the graphs in (b) at $5 \geq C_4/C_{12} \geq 0$.

The plot of *n*-C_{16} conversion versus temperature for this system in a standard run suggests an increase in conversion followed by levelling-off or a plateau as the reactor temperature is increased. The performance of this catalyst, in terms of *n*-C_{16} conversion, is significantly improved compared to that observed for the catalyst based on P-ZSM-5(50) as support (Figure 4.12). For example, the conversion at 200 °C increased by a factor of 4, that at 220 °C by a factor of 4, while that at 240 °C increased ~2 times upon increasing the SAR of the support to 77. The detrimental effect of co-feeding H_2O and CO on the conversion is also apparent in this case as well. With H_2O alone as a co-feed at 240 °C, the *n*-C_{16} conversion dropped drastically to 6%, and preliminarily showed an increase with reactor temperature

thereafter. A similar trend was seen upon inclusion of CO in the co-feed. The corresponding C_4/C_{12} ratio plots also confirmed non-ideality, with $C_4/C_{12} \neq 1$ [Figure 4.14(b) and the inset]. Very interesting are the product distributions of this catalyst, illustrated in Figure 4.15.

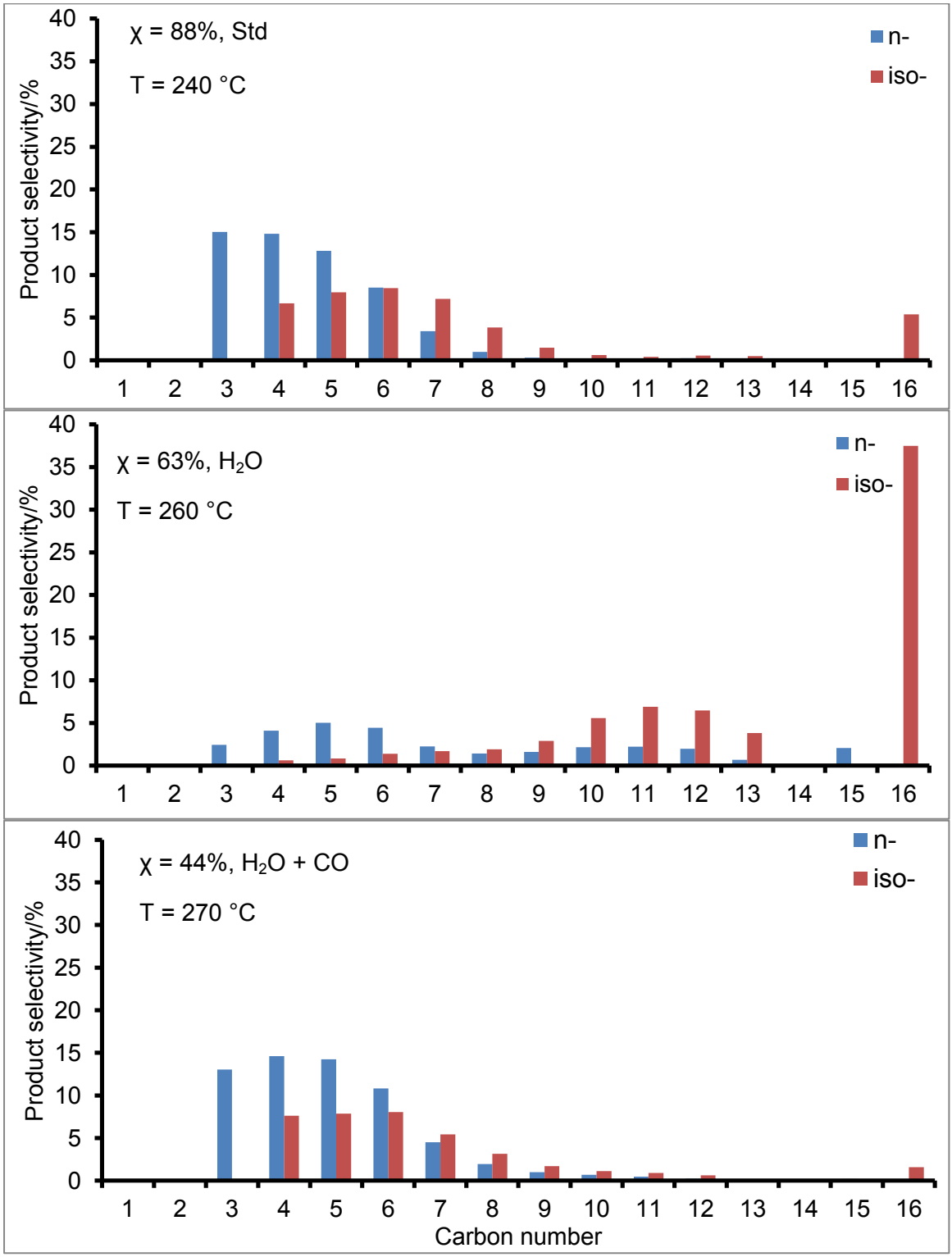

Figure 4.15 The cracked product distributions for standard and non-standard hydrocracking of *n*-C_{16} over the 0.9 wt.% Pd/P-ZSM-5(77) catalyst.

It is seen from Figure 4.15 that the predominant products in the standard run of this reaction are in the carbon number range C_3 - C_7, with little or no products above C_8. This may be an indicator of secondary cracking taking place under the conditions of

this experiment. The *iso*-C_{16} product in this run is formed in small amounts. However, the co-feeding of H_2O changes the trend completely. The product distribution exhibits more isomerised products in the higher carbon number range and approximately a seven-fold increase in the *iso*-C_{16} selectivity. Interestingly, the co-feeding of (H_2O + CO) disrupts the product distribution, which then looks similar to that for the standard run. This shows that the introduction of CO aggravates secondary cracking.

Another similarly prepared hydrocracking catalyst with the support of even higher SAR, (*i.e*., 100), was also explored for efficiency in this process. The results are plotted below (Figure 4.16).

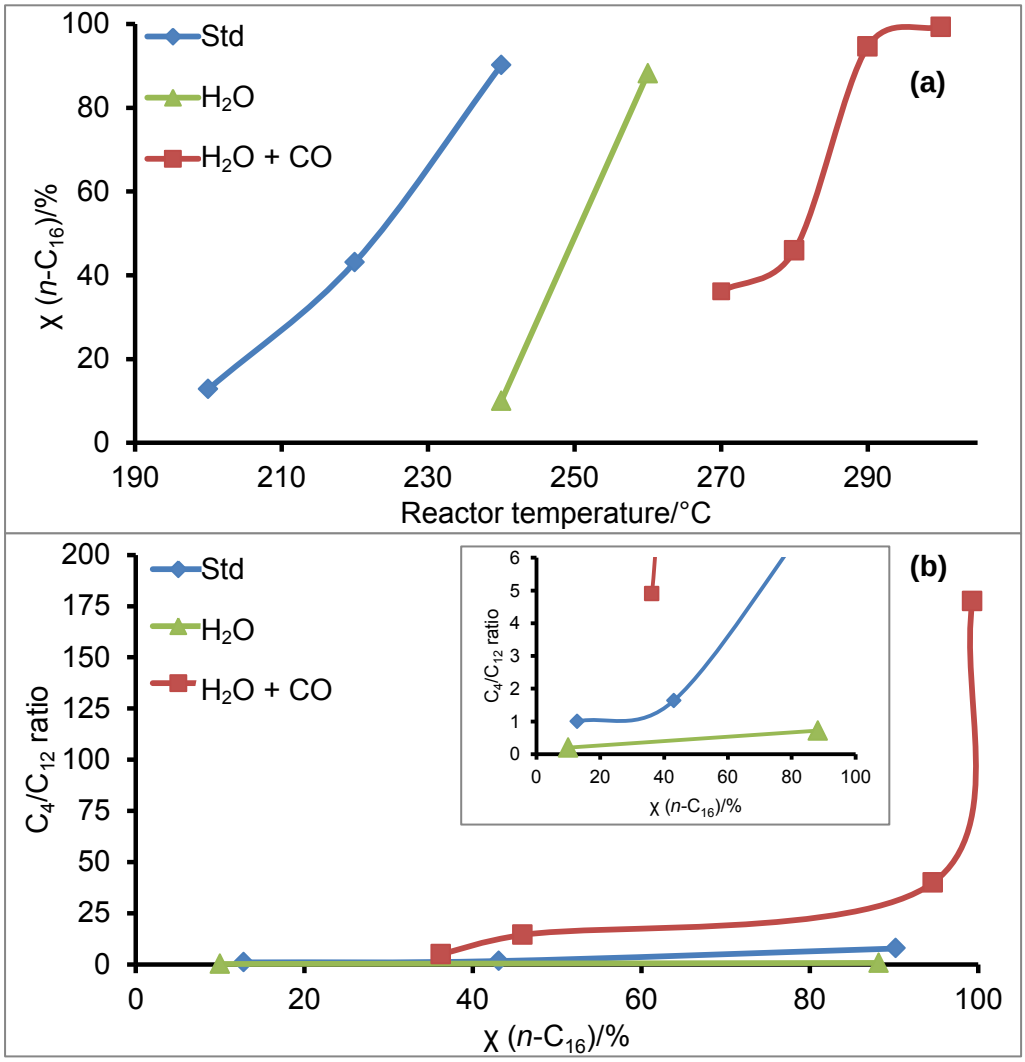

Figure 4.16 The catalytic performance of 0.9 wt.% Pd/P-ZSM-5(100) catalyst in the hydrocracking of *n*-C_{16}: (a) χ (*n*-C_{16}) v/s reactor temperature and (b) C_4/C_{12} product ratio v/s χ (*n*-C_{16}). The inset shows the graphs in (b) at $6 \geq C_4/C_{12} \geq 0$.

A monotonically increasing pattern is shown by the plot of *n*-hexadecane conversion against reactor temperature for the standard run in Figure 4.16. The co-feeding of H_2O takes this reaction to higher reactor temperatures in order to achieve high catalytic activity. Upon inclusion of CO in the H_2O co-feed, the catalytic activity gets suppressed and conversion decreases. A further increase in the reactor temperature shows an *s*-shaped graph which levels off at conversions close to 100%. Interestingly, the catalytic performance observed for this catalyst system is generally inferior to that observed for the 0.9 wt.% Pd/P-ZSM-5(77), though better than 0.9 wt.% Pd/P-ZSM-5(50) under similar conditions. The inset clearly shows that the C_4/C_{12} ratio is far greater than 1 in both the standard and (H_2O + CO) runs. This

indicates that secondary cracking is prevalent with and without the co-feeding of H_2O and CO. The cracked product distributions of this catalyst are shown in Figure 4.17.

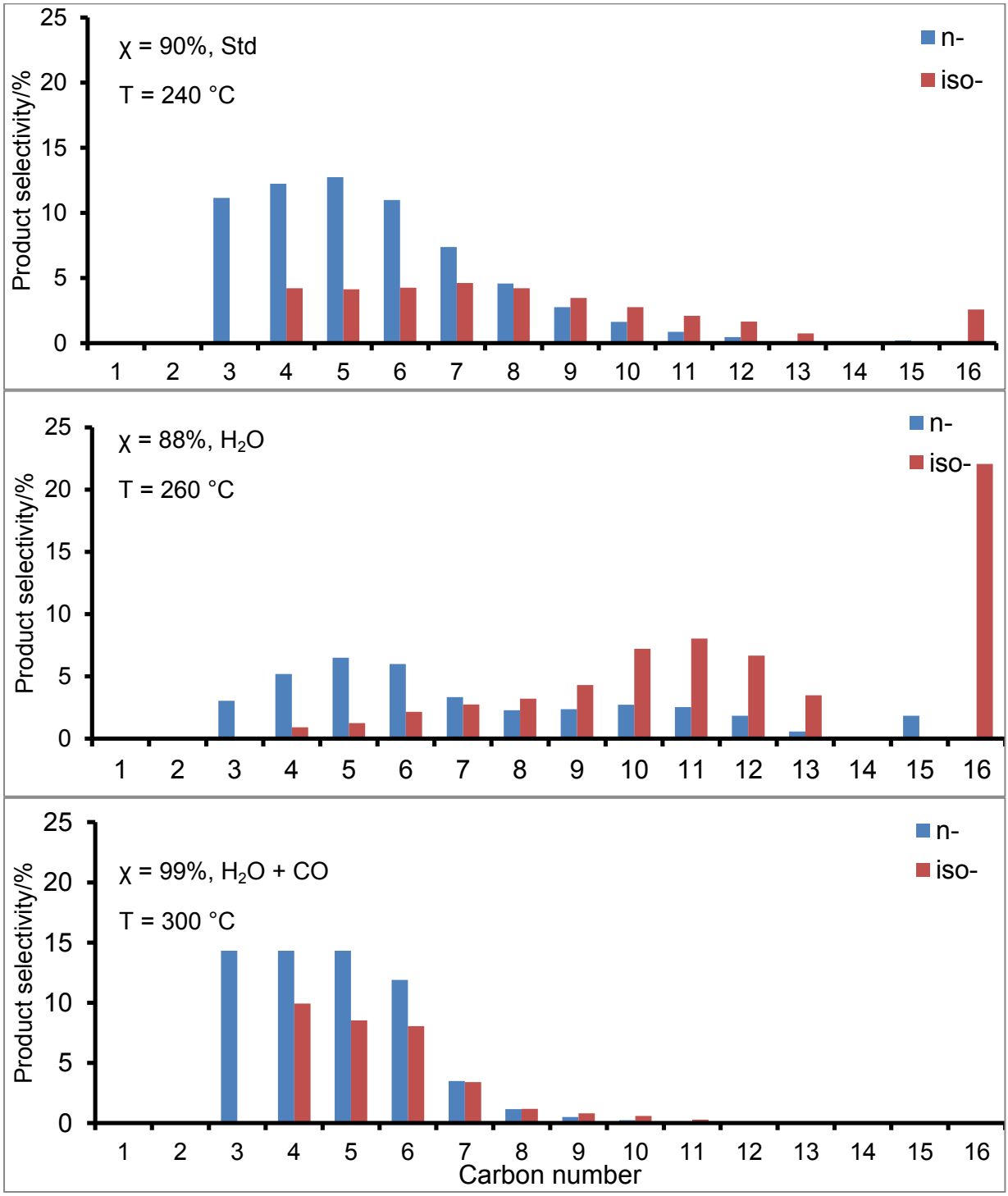

Figure 4.17 The cracked product distributions for standard and non-standard hydrocracking of *n*-C_{16} over the 0.9 wt.% Pd/P-ZSM-5(100).

The cracked product distribution obtained on this catalyst system is similar to those observed over the catalysts with lower SARs (Figure 4.13 and 4.15), where the dominant products lie in the carbon number range C_3 - C_7. The standard run of this catalyst shows that there is secondary cracking occurring. Upon co-feeding H_2O, the distribution of isomerised products shifts to higher carbon numbers followed by a tremendous increase in the selectivity to *iso*-C_{16}. This shows that H_2O serves as a promoter for isomerisation though it seemed detrimental to the conversion. However, co-feeding (CO + H_2O) poisons the catalyst, and existence of extreme secondary is revealed by the dominant lighter products.

The next series of catalyst supports was obtained from each pristine zeolite (*the three zeolites discussed above*), where the zeolite sample was subjected to a post-synthesis desilication treatment in order to induce mesopores within the zeolite matrix (*see detailed procedure in Chapter 3*). The results of this study are presented and discussed below. Figure 4.18 shows the catalytic performance of a 0.9 wt. % Pd/D-ZSM-5(50*) catalyst under both standard and non-standard runs.

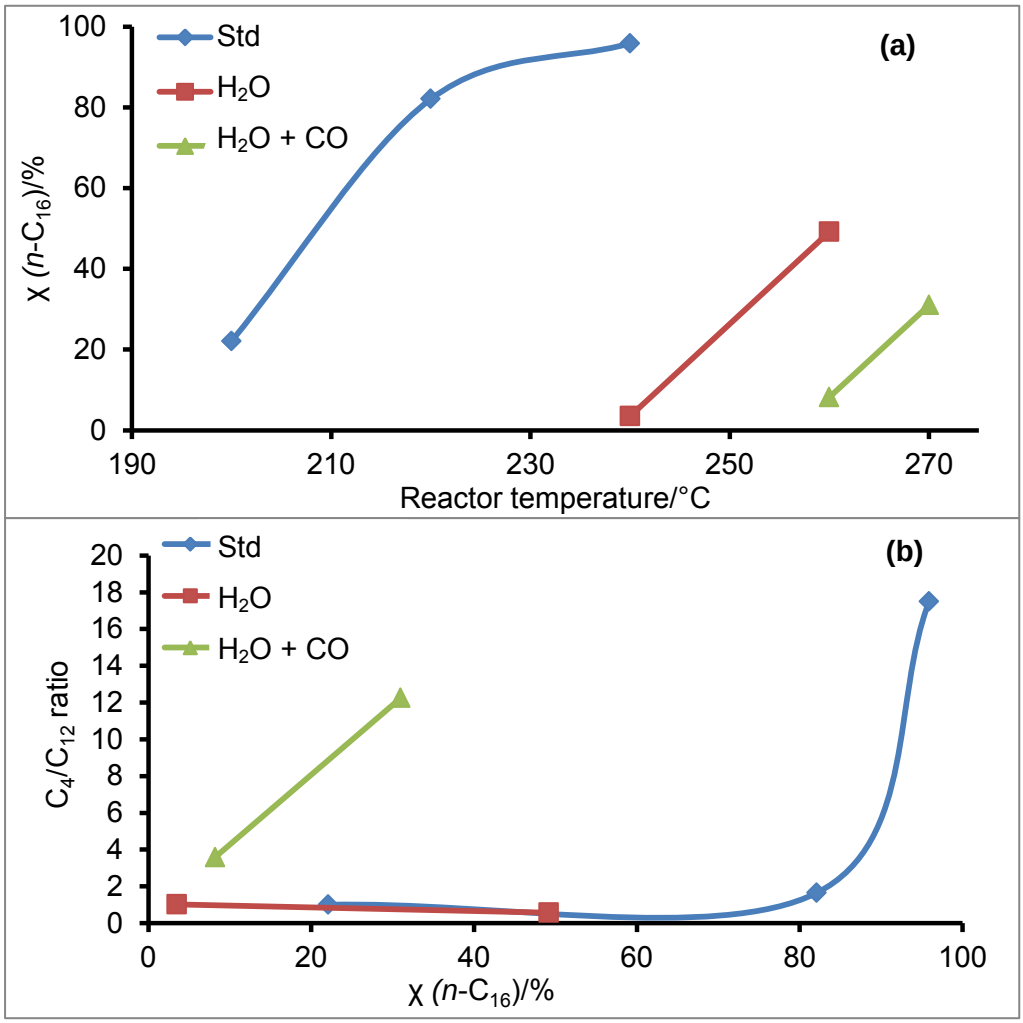

Figure 4.18 The catalytic performance of 0.9 wt.% Pd/D-ZSM-5(50*) catalyst in the hydrocracking of *n*-C_{16}: (a) χ (*n*-C_{16}) v/s reactor temperature and (b) C_4/C_{12} product ratio v/s χ (*n*-C_{16}).

As expected, conversion increases with increasing reactor temperature [9]. The performance of this catalyst has significantly improved compared to that observed for its pristine-form. Under similar conditions, the conversion over 0.9 wt.% Pd/D-ZSM-5(50*) is almost 5 times higher than that over the pristine zeolite-based 0.9 wt.% Pd/P-ZSM-5(50). This catalyst also outperfoms the best-perfoming pristine zeolite based catalyst [*i.e.*, 0.9 wt.% Pd/P-ZSM-5(77)]. The S_{BET} of the current desilicated suppport is also higher than that of the best-perfoming catalyst support from the pristine zeolite series. Four factors can be attributed to the observed improvement in the catalytic performance of the 0.9 wt.% Pd/D-ZSM-5(50*) relative to its pristine counterpart: (i) the readjusted SAR, (ii) the newly generated mesopores (see Figure 4.10), (iii) induced Brønsted acidity (*deduced from FT-IR peaks in the hydroxyl*

region in Figure 4. 6), and (iv) the increased surface areas (see Table 4.3), as a result of the desilication treatment. This catalyst had the S_{BET} of 378 m^2/g, while its pristine-based counterpart had 114 m^2/g. Larger surface areas allow the feed molecule to interact the with surface of the support more efficiently, leading to enhanced catalytic performance observed for the resulting catalyst [26]. Therefore, the beneficial influence of the desilication treatment of the support is clearly demonstrated for this catalyst system. The corresponding C_4/C_{12} ratios indicate the dominance of secondary cracking. This observed secondary cracking may be attributed to the Brønsted acidity suggested by the IR spectrum of the support (Figure 4.6), which suggests that the desilication treatment enhanced acid sites that are responsible for hydrocarbon cracking. The presence of these newly generated acid sites manifests itself in the product distribution profiles illustrated in Figure 4.19 below.

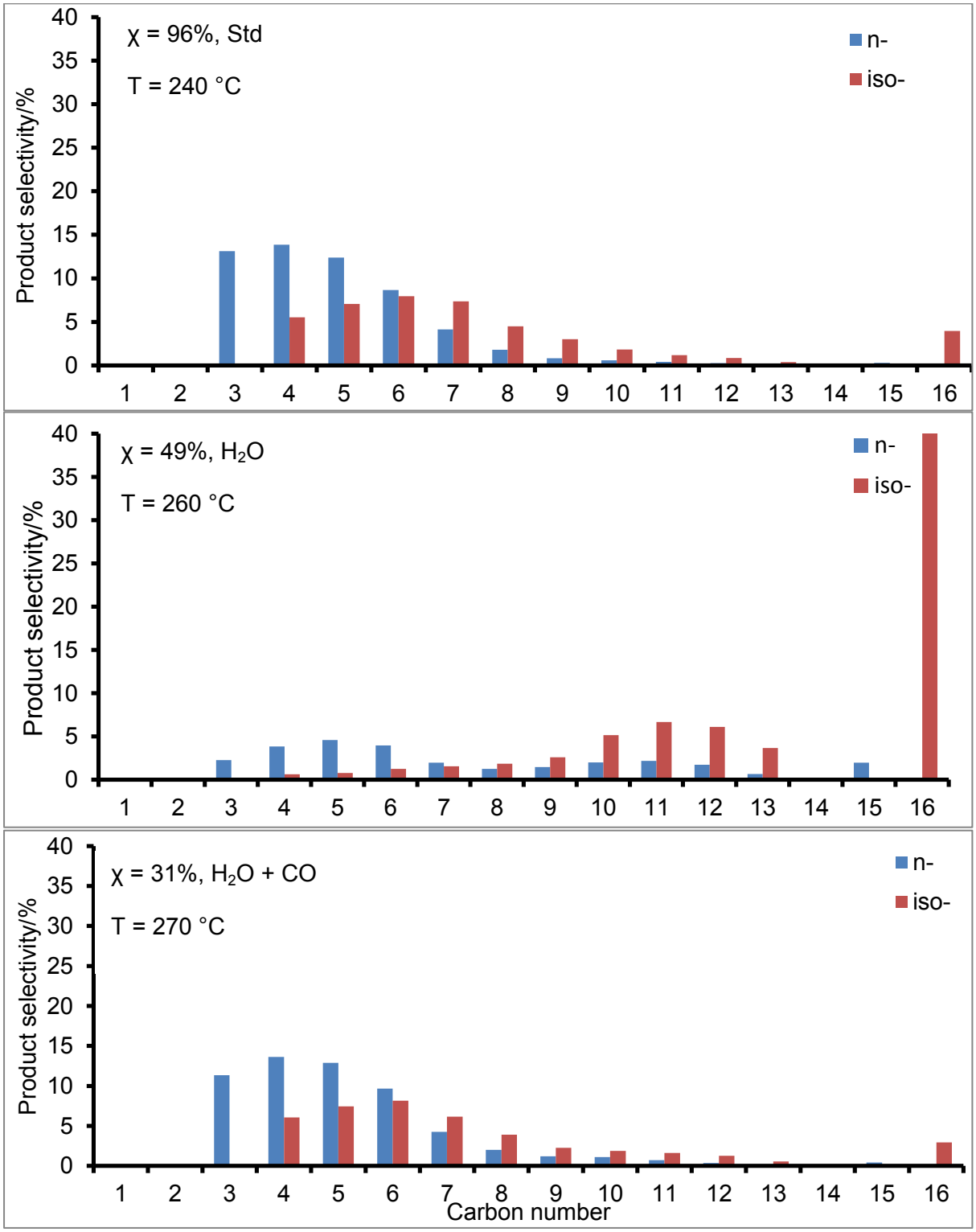

Figure 4.19 The cracked product distributions for standard and non-standard hydrocracking of *n*-C_{16} over the 0.9 wt.% Pd/D-ZSM-5(50*) catalyst.

In the standard run, the product distribution is dominated by hydrocarbons in the range C_3 - C_7 compared to products of a higher carbon number. There is also the presence of isomerised products, including *iso*-C_{16}. The dominance of the normal C_3

- C_7 product stream may be taken as evidence of secondary cracking taking place during this conversion reaction. Comparison of the C_3 - C_7 fraction of the product spectrum on this catalyst with that of its pristine zeolite-based counterpart (Figure 4.13) clearly revealed that the selectivity increases by a factor of 2. This demonstrates increased secondary cracking in the desilication-derived catalyst than the pristine-derived catalyst, and agrees well with the observed Brønsted acidity brought about by desilication treatment (Figure 4.6). Although there is no appreciable conversion in the presence of H_2O alone as a co-feed, the product distribution seems to show a different trend. That is, decreased amount of C_3 - C_7 products and relatively larger amounts of higher hydrocarbon products. Very notable is the substantial amount of the *iso*-C_{16} product formed during this conversion reaction when H_2O is the sole co-feed. Feed isomerisation is desirable for low-temperature flow properties of fuels. Besides the detrimental effect of H_2O on conversion in the standard run, it seems to promote isomerisation in the non-standard run, particularly to higher carbon chain isomers (C_9 - C_{16}).

The catalytic performance of a similarly prepared catalyst involving a zeolitic support with a higher SAR of 77*, *viz*., 0.9 wt.% Pd/D-ZSM-5(77*) is shown in Figure 4.20.

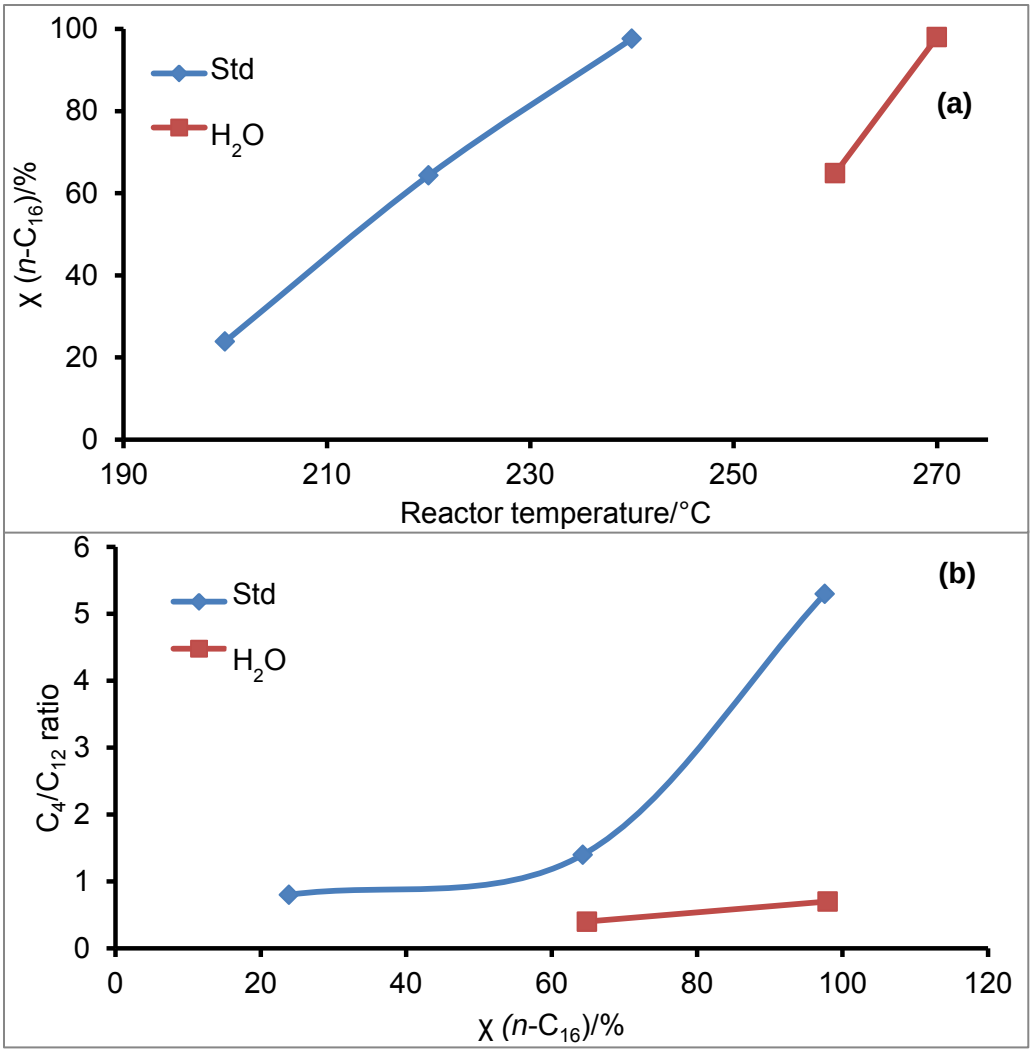

Figure 4.20 The catalytic performance of 0.9 wt.% Pd/D-ZSM-5(77*) catalyst in the hydrocracking of *n*-C_{16}: (a) χ (*n*-C_{16}) v/s reactor temperature and (b) C_4/C_{12} product ratio v/s χ (*n*-C_{16}).

The catalytic behaviour of this catalyst system is generally slightly improved compared to its pristine form in Figure 4.14, with the exception that the conversion at 220 °C over 0.9 wt.% Pd/D-ZSM-5(77*) dropped by 10% relative to that over the pristine zeolite-based, 0.9 wt.% Pd/P-ZSM-5(77). The slight improvement in catalytic activity of this system can be attributed to the readjustment of the SAR, additional mesopores, Brønsted acidity (FT-IR OH region) and S_{BET} enhancement, resulting from desilication. It can be seen that the C_4/C_{12} ratios are lower compared to those of the catalyst based on the pristine support, although still greater than 1. Co-feeding H_2O also proved detrimental to conversion for this catalyst system, shifting it to

higher temperatures. The cracked product distributions from the hydrocracking of *n*-hexadecane under different runs are shown in Figure 4.21.

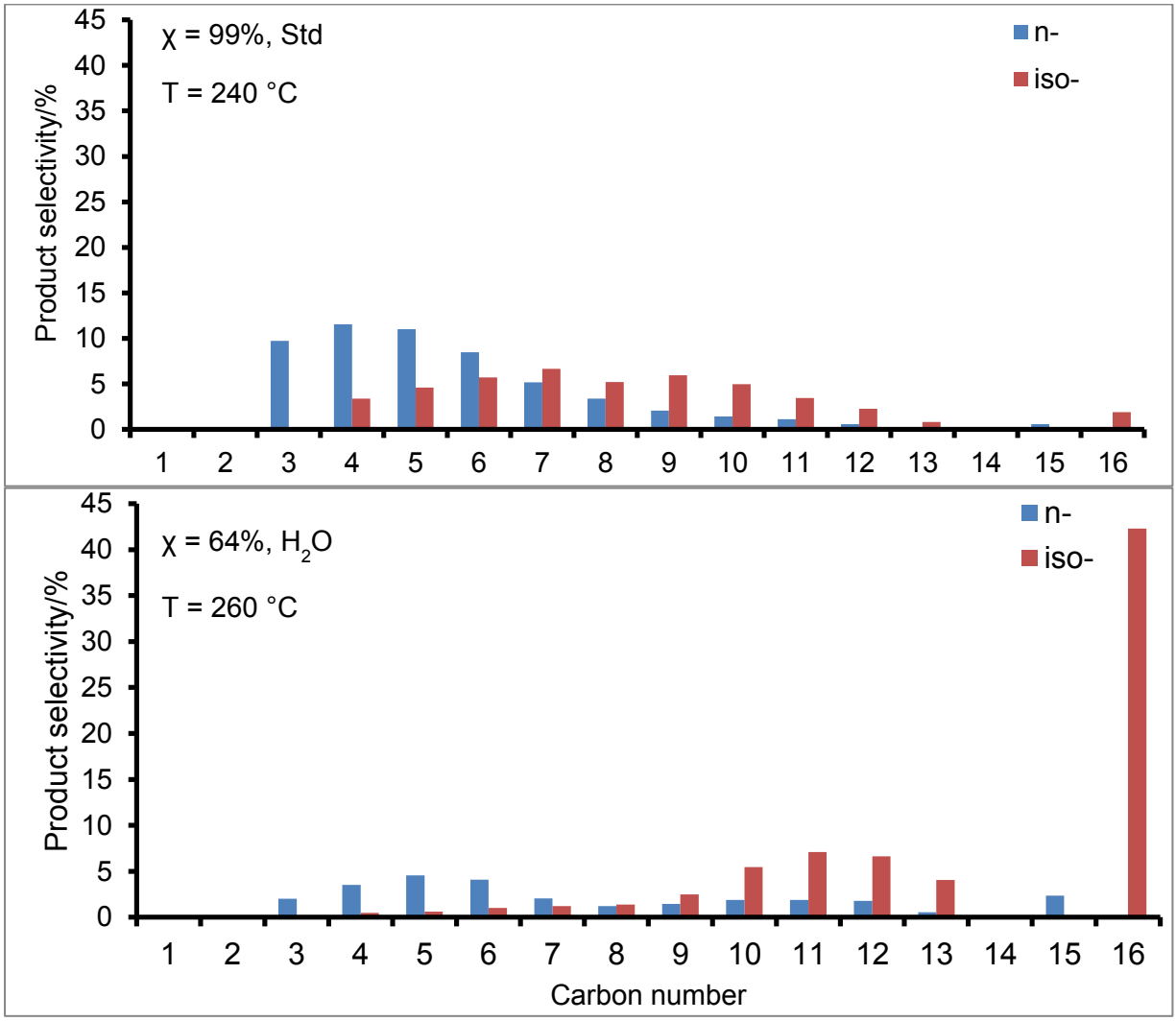

Figure 4.21 The cracked product distributions for standard and non-standard hydrocracking of *n*-C_{16} over the 0.9 wt.% Pd/D-ZSM-5(77*) catalyst.

The distribution of cracked *n*-paraffins has a maximum in the lower carbon numbers (C_3 - C_7), with C_4 selectivity being greater than C_{12} in both runs. Very remarkable is the increased selectivity of *iso*-C_{16} upon co-feeding H_2O, which is 22 times more than in the standard run. Also, selectivity to isomerised products in the higher carbon numbers of the non-standard run is higher than in the standard run. Although there is evidence of secondary cracking, there is an appreciable amount of *iso*-paraffins in the presence of H_2O.

The catalytic performance of the 0.9 wt.% Pd/D-ZSM-5(100*) catalyst is illustrated in the figure below.

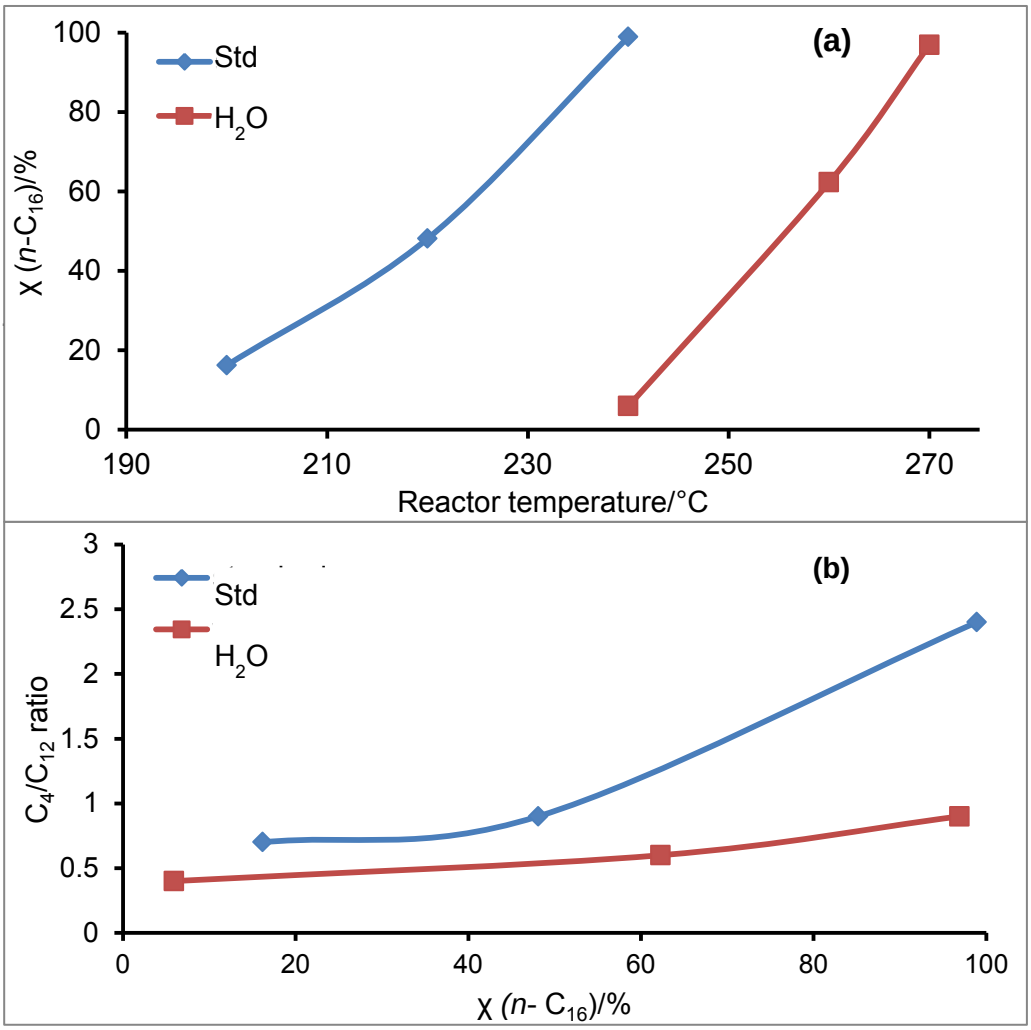

Figure 4.22 The catalytic performance of 0.9 wt.% Pd/D-ZSM-5(100*) catalyst in the hydrocracking of *n*-C_{16}: (a) χ (*n*-C_{16}) v/s reactor temperature and (b) C_4/C_{12} product ratio v/s χ (*n*-C_{16}).

The catalytic behaviour of this catalyst is slightly improved compared to that of the pristine zeolite-based counterpart illustrated in Figure 4.16. Similarly to the other desilicated zeolite-based catalysts discussed above, this improvement in catalytic performance relative to the pristine counterpart can be attributed to reinforced physicochemical properties such as readjustment of SAR, newly-generated mesopores, IR Brønsted acidity and S_{BET}. Zero or negligible conversions are obtained upon co-feeding H_2O, but the activity resumes with further increases in the reactor temperature. It is interesting to note that although co-feeding H_2O poisons

the catalyst and shifts the catalytic activity to high temperatures, it is found to also promote isomerisation reactions. The highest C_4/C_{12} ratio on the 0.9 wt.% Pd/P-ZSM-5(100) catalyst was 7.8 in a standard run, while in this catalyst system this ratio is only 2.4. This observation suggests that the desilicated support exhibits less secondary cracking compared to its pristine form. This contradicts the observation made from the IR spectrum, where more Brønsted acidity was evident in the desilicated zeolite than in the pristine one, and therefore more secondary cracking was expected in the former system. It can also be observed that the co-feeding of H_2O significantly decreases the C_4/C_{12} ratios, thus minimising secondary cracking. Figure 4.23 shows the product distribution over this catalyst.

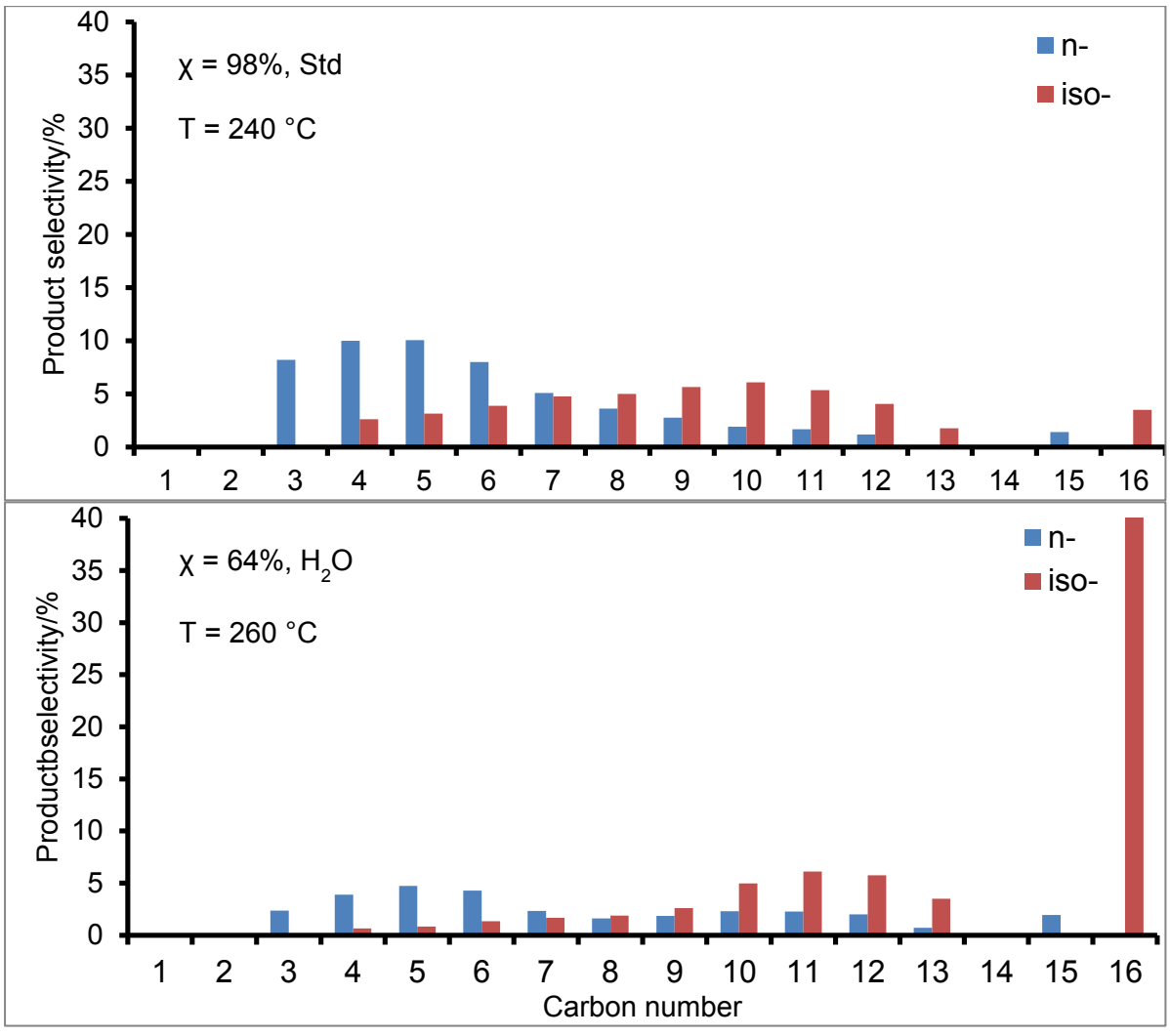

Figure 4.23 The cracked product distributions for standard and non-standard hydrocracking of *n*-C_{16} over the 0.9 wt.% Pd/D-ZSM-5(100*) catalyst.

The product distributions of both runs in Figure 4.23 show that the C_4 selectivity is greater than C_{12}, which is consistent with the C_4/C_{12} ratios in Figure 4.22(b). In the presence of H_2O, the selectivity to *iso*-paraffins in the C_4 - C_9 range decreases, while that to C_{10} - C_{13} slightly increased. An approximately eleven-fold increase in the *iso*-C_{16} is also observed upon co-feeding H_2O. Although H_2O decreased the *n*-C_{16} conversion in Figure 4.22(a), the product distribution shows that selectivity to *iso*-paraffins is enhanced and minimal secondary cracking is taking place.

Figure 4.24 summarises and compares the overall catalytic performances of the above three catalyst systems in their standard runs, by superimposing the corresponding plots [*Figures 4.12(a), 4.14(a) and 4.16(a)*].

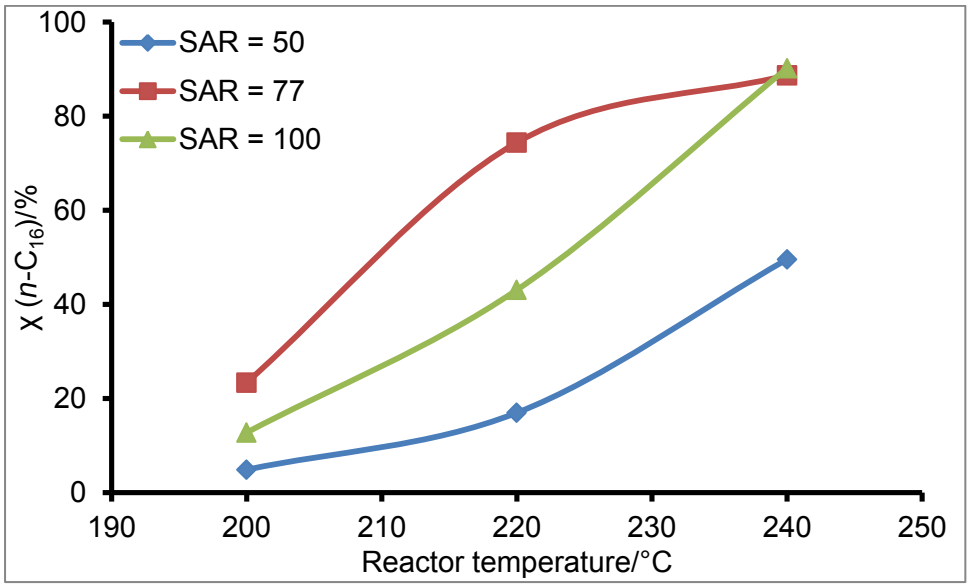

Figure 4.24 Comparison of the catalytic hydrocracking performance of pristine zeolite-based catalysts with different SARs at 0.9 wt.% Pd loading.

The catalytic performance (in terms of *n*-C_{16} conversion) of pristine zeolite-based catalysts follow the order Pd/P-ZSM-5(77) > Pd/P-ZSM-5(100) > Pd/P-ZSM-5(50). Though the high SAR ZSM-5 supports perform better than their low SAR counterpart (SAR = 50), it is important to note the superiority of P-ZSM-5(77) compared to P-ZSM-5(100). This is surprising if one considers the superior physicochemical properties [crystallinity = 100% and S_{BET} = 170 m^2/g of the 0.9 wt.% Pd/P-ZSM-5(100) relative to those of the 0.9 wt.% Pd/P-ZSM-5(77)] catalyst system. The trend illustrated in this figure, *i.e.*, an increase in catalytic performance with increasing

SAR followed by decreased performance with further increase in SAR, suggests the existence of an optimum SAR for this reaction. This optimum SAR is close to 77.

Figure 4.25 summarises and compares the overall catalytic performances of the above three catalyst systems in their standard runs, by superimposing the corresponding plots [*Figures 4.18(a), 4.20(a) and 4.22(a)*].

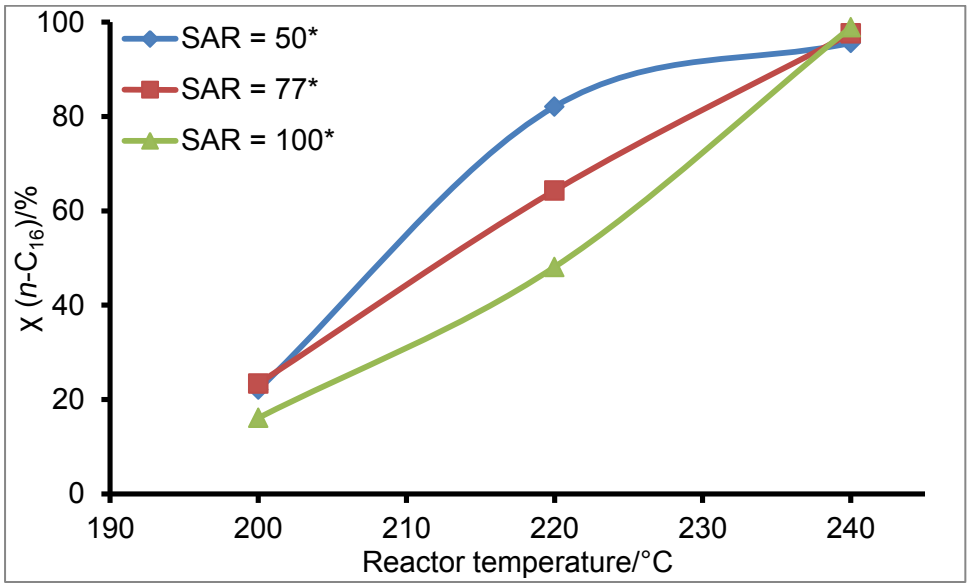

Figure 4.25 Comparison of the catalytic hydrocracking performance of the desilicated zeolite-based catalysts with different SARs at 0.9 wt.% Pd loading.

The catalytic activity of the catalysts improves with increasing Al content, *i.e.*, a decrease in SAR, of the zeolite support in the order Pd/D-ZSM-5(50*) > Pd/D-ZSM-5(77*) > Pd/D-ZSM-5(100*). Besides a clear correlation of catalytic activity with SAR, this order seems to agree with the extent to which the S_{BET} of each zeolite was increased by the desilication treatment to produce these hierarchical supports. That is, 70, 63 and 48% increase in S_{BET} for P-ZSM-5(50), P-ZSM-5(77) and P-ZSM-5(100), respectively. It is interesting to note that the most inferior support in the pristine state has become the most superior after the desilication treatment. Another observation from both pristine and desilicated supports is that the most crystalline materials are actually not the best. From this series of catalysts, it can be concluded that the optimum SAR to perform desilication (*under conditions used in this work*) that produces a promising ZSM-5 zeolite support (with improved catalytic performance) is 50.

4.3.2 Hydrocracking of *n*-C_{16} over surfactant-templated ZSM-5 based catalysts

In addition to the generation of hierarchical porosity in the acidic support through a post-synthesis desilication procedure, this research has also explored the 1-pot synthesis of multiporous MFI-type zeolites using polyquaternary ammonium surfactants as structure-directing templates or porogens. Three types of Gemini surfactants, abbreviated as 18-N_2, 18-N_3-18 and 18-N_4-18, were first synthesised through organic synthesis routes prior to their use as porogens in the synthesis of this class of zeolites. The resulting hierarchical zeolites, containing both micropores and mesopores within the same matrix, were then used as acidic supports for the preparation of Pd-based hydrocracking catalysts which were further investigated for catalytic performance in the hydrocracking of *n*-hexadecane as a model LTFT wax component. The results of this study are presented and discussed below. Figure 4.26 shows the variation of χ (*n*-C_{16}) with reactor temperature, and the C_4/C_{12} ratio as a function of χ (*n*-C_{16}) over the 0.9 wt.% Pd/HSZ(N_2) catalyst.

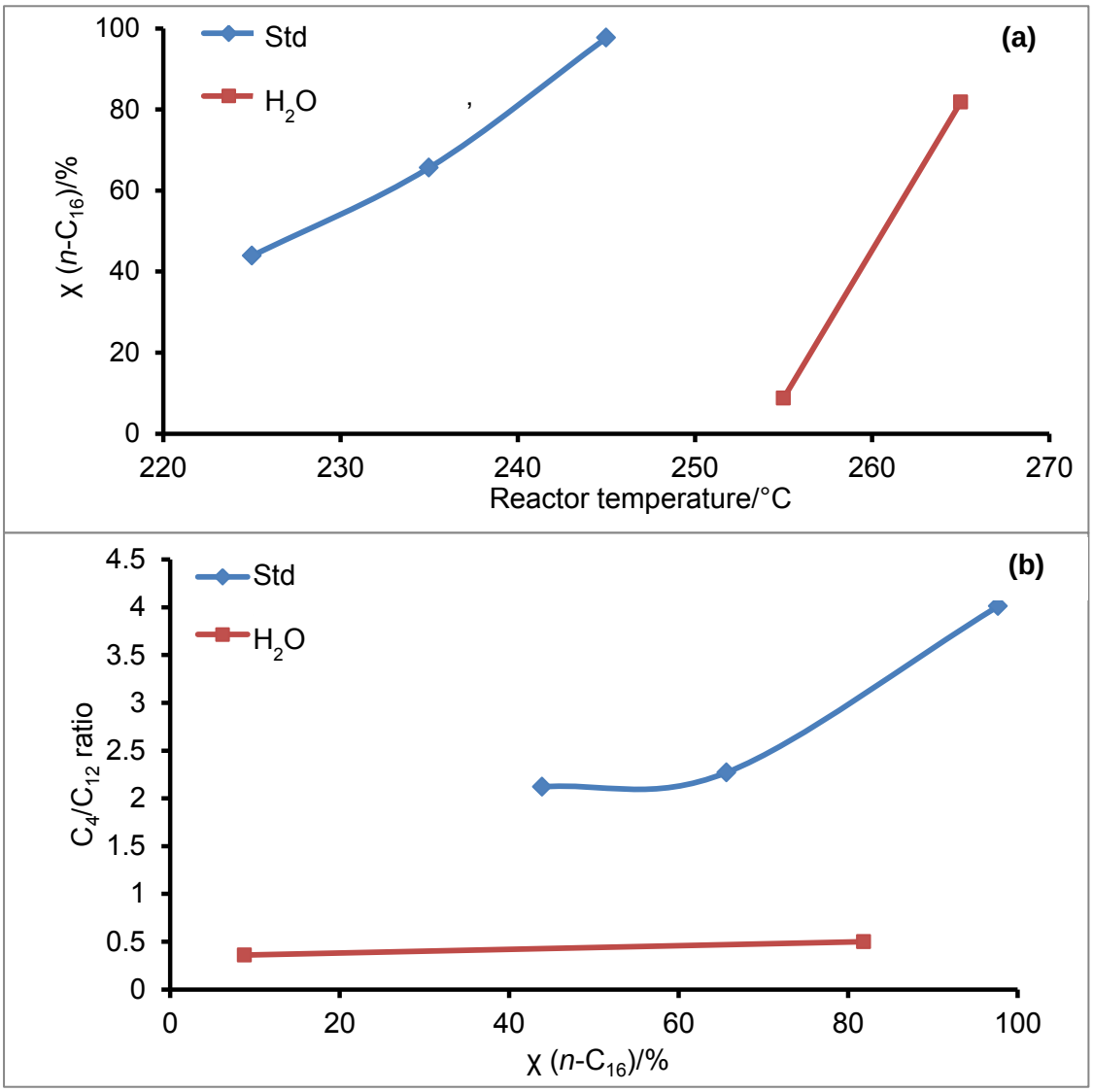

Figure 4.26 The catalytic performance of 0.9 wt.% Pd/HSZ(N_2) catalyst in the hydrocracking of *n*-C_{16}: (a) χ (*n*-C_{16}) v/s reactor temperature and (b) C_4/C_{12} product ratio v/s χ (*n*-C_{16}).

An increase in *n*-C_{16} conversion as a function of reactor temperature is demonstrated by the hydrocracking catalyst based on the hierarchical zeolite synthesised using a surfactant containing two quaternary ammonium centres as SDA. Also demonstrated is the detrimental effect of co-feeding of H_2O with the hydrocracking feedstock after attaining steady-state conversion at a reactor temperature of 245 °C in the standard run [Figure 4.26(a)]. The observed drop in conversion (from 98 to 9%) suggests that H_2O is acting as a poison to the active sites on the catalyst. Interestingly, Figure 4.24(b) shows a non-ideal hydrocracking behaviour for both standard and non-standard runs, with $C_4/C_{12} \neq 1$. The non-ideal hydrocracking behaviour is also

supported by the unsymmetrical distribution of cracked products, as illustrated in Figure 4.27 below.

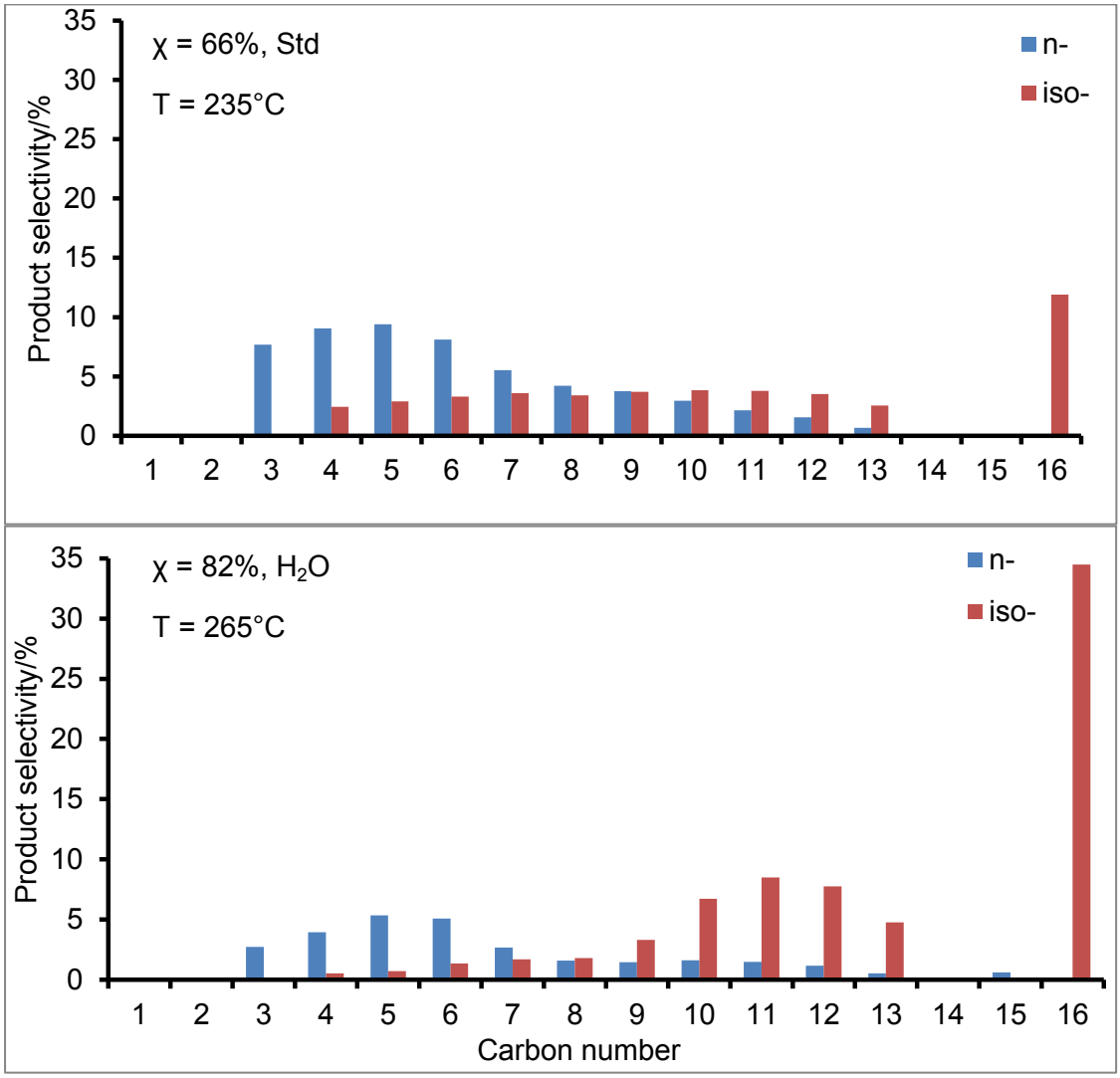

Figure 4.27 The cracked product distributions for standard and non-standard hydrocracking of *n*-C_{16} over the 0.9 wt.% Pd/HSZ($N_{2.}$) catalyst.

The product distributions of this catalyst consist of both normal and isomerised hydrocarbons. It is important to note that *iso*-C_{16} is produced in significant amounts compared to the lower *iso*-products (*in both standard and non-standard runs*). In the standard run, the *n*-alkane products are predominantly in the lower carbon number range, with a maximum at C_5 and tailing off beyond this carbon number. This is again an indicator of repeated cracking. However, the *iso*-products show a relatively flat distribution in the carbon number range C_4 - C_{13}. On the other hand, co-feeding H_2O as one of the FT reactor outlet products changed the product distribution profile

observed in the standard run. This co-feeding caused a significant reduction in the amount of lighter *n*-alkanes and an increase in the C_9 - C_{13} isomerised products (in addition to *iso*-C_{16}). Notably, this co-feeding is also accompanied by a pronounced increase in the selectivity to *iso*-C_{16}. The ability of this catalyst system to produce *iso*-C_{16} from the *n*-C_{16} feed may be taken as a starting point to the design of a diesel-selective catalyst, because this ability to produce isomerised products influences the cold-flow properties of diesel [25]. A similarly prepared catalyst, comprising a hierarchical zeolite support synthesised using a polyquaternary ammonium surfactant containing three ammonium centres, HSZ(N_3), exhibited the *n*-C_{16} hydrocracking performance shown in Figure 4.28 below.

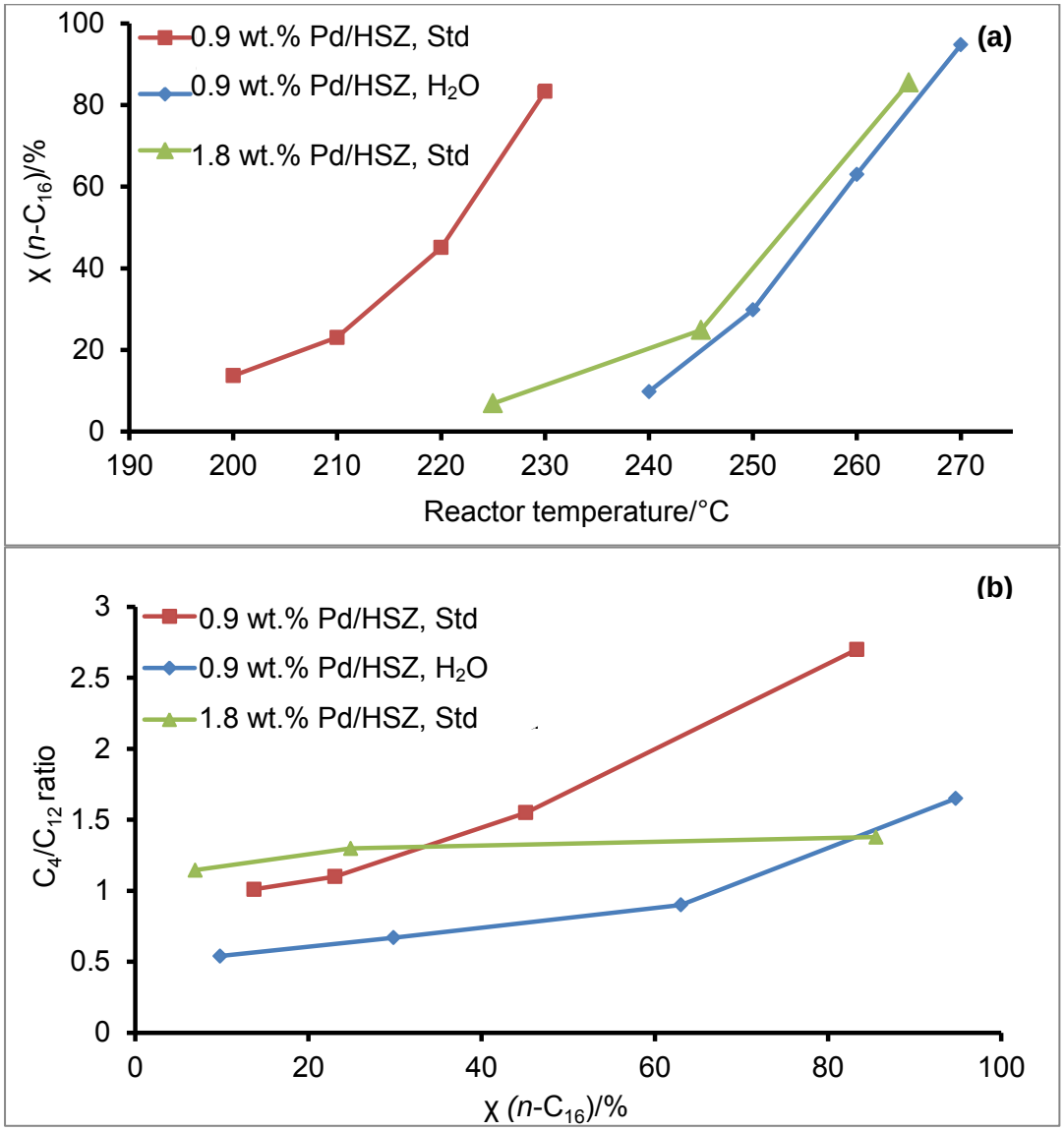

Figure 4.28 The catalytic performance of 0.9 and 1.8 wt.% Pd/HSZ(N_3) catalyst in the hydrocracking of *n*-C_{16}: (a) χ (*n*-C_{16}) v/s reactor temperature and (b) C_4/C_{12} product ratio v/s χ (*n*-C_{16}).

The standard hydrocracking runs on the 0.9 wt.% Pd and 1.8 wt.% Pd supported catalysts showed increasing trends of *n*-C_{16} conversion as a function of reactor temperature [Figure 4.28(a)]. It is important to note the similarity in the effect of doubling the metal loading and co-feeding H_2O. Interestingly, the low-loaded catalyst [0.9 wt.% Pd/HSZ(N_3)] showed superior catalytic performance in terms of low-temperature activity compared to the higher-loaded catalyst [1.8 wt.% Pd/HSZ(N_3)], whose catalytic activity shifted to higher reactor temperatures [Figure 4.28(a)]. Therefore, increasing the Pd loading on this support produced a catalyst with poor catalytic activity. As seen before, co-feeding H_2O poisons the active sites on the

catalyst and shifts the activity to higher reactor temperatures as shown in Figure 4.28(a). The corresponding plots of C_4/C_{12} ratios versus χ (*n*-C_{16}) also confirm the occurrence of secondary cracking and a non-ideal hydrocracking behaviour of these catalyst systems, though the 1.8 wt.% Pd catalyst stays closer to ideality within the conversion range studied [Figure 4.28(b)]. The deviation of this catalyst system from ideality is also demonstrated by the product distribution profiles in Figure 4.29.

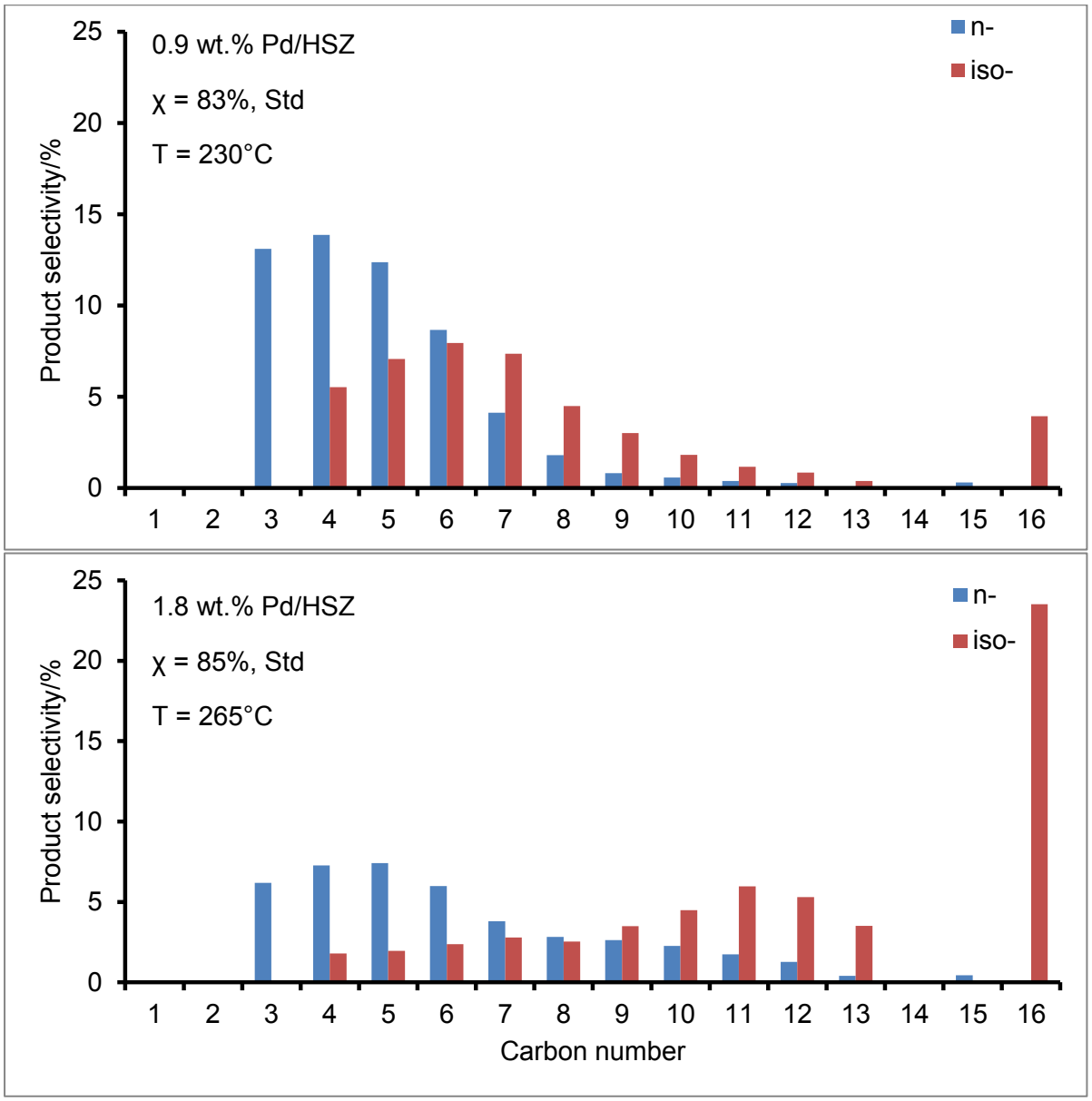

Figure 4.29 The cracked product distributions for standard hydrocracking of *n*-C_{16} over the 0.9 and 1.8 wt.% Pd/HSZ(N_3) catalyst.

In this figure, secondary cracking manifests itself by the dominance of shorter chain products (<C_8) on the 0.9 wt.% Pd/HSZ(N_3) catalyst. This can suggest the presence

of more acid sites than metal sites. Doubling the metal loading leads to the reduction in the amount of *n*-alkane products and an increase in the isomerised C_9 - C_{13} content. This is accompanied by an approximately six-fold increase in *iso*-C_{16}. It is clear that the 1.8 wt.% Pd/HSZ catalyst exhibits minimal secondary cracking and may be tuned to maximise the diesel yield from the hydrocracking of LTFT wax. A third member of this series of soft-templated hierarchical MFI zeolites was synthesised using a surfactant containing four quaternary ammonium centres. Figure 4.30 shows plots summarising the behaviour of this system as a hydrocracking catalyst.

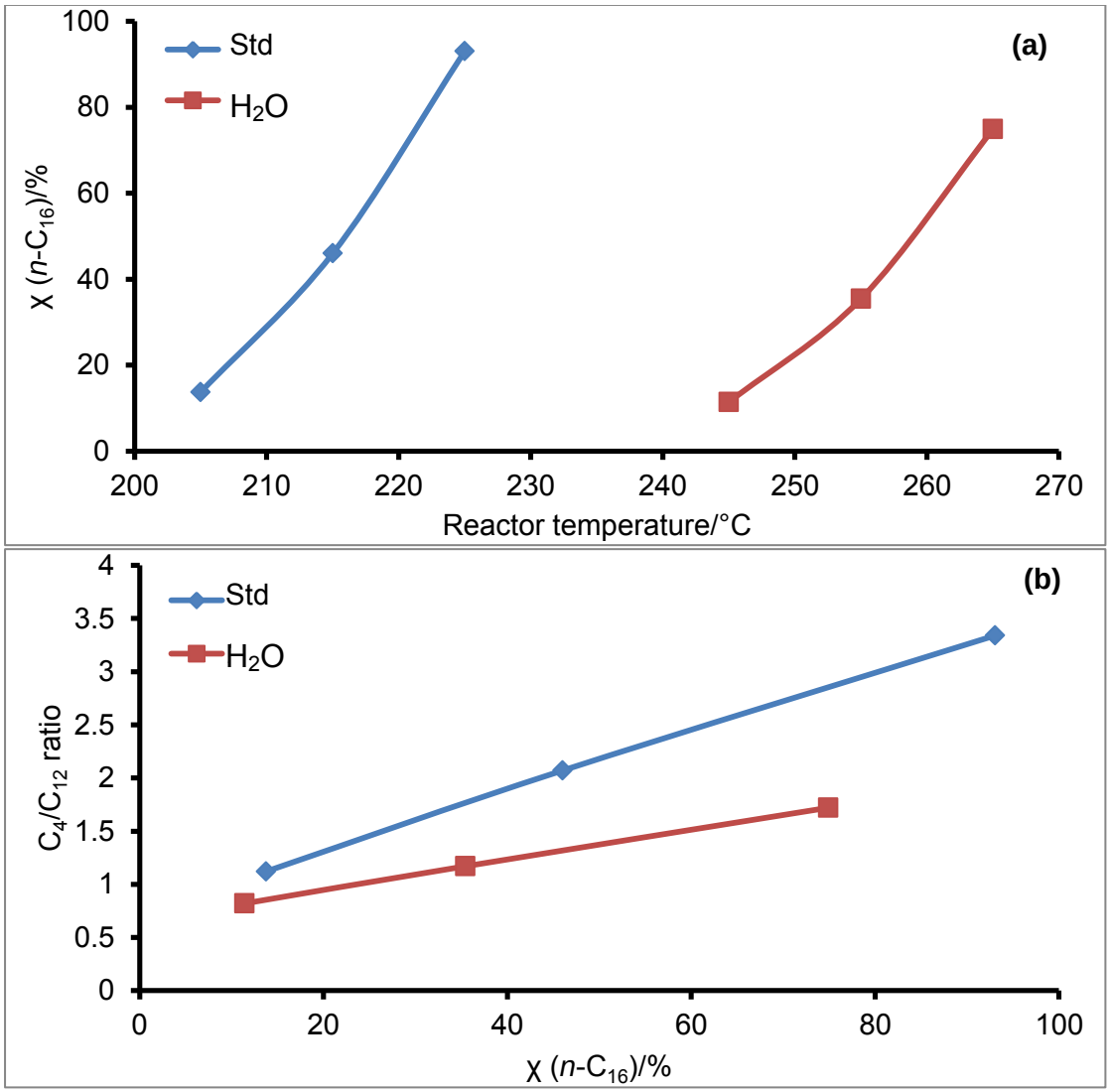

Figure 4.30 The catalytic performance of 0.9 wt.% Pd/HSZ(N_4) catalyst in the hydrocracking of *n*-C_{16}: (a) χ (*n*-C_{16}) v/s reactor temperature and (b) C_4/C_{12} product ratio v/s χ (*n*-C_{16}).

As in other catalysts supported on hierarchical zeolites based on soft-templated synthesis, this catalyst system shows an increase in *n*-C_{16} conversion as a function of reactor temperature, under both the standard run and that involving the co-feeding of H_2O [Figure 4.30(a)]. The catalytic activity of this catalyst is shifted to higher reactor temperatures, T ≥ 245 °C, in the presence of H_2O, again signalling the poisoning effect of H_2O on the zeolite active sites. As the corresponding C_4/C_{12} ratio versus χ (*n*-C_{16}) plots illustrate [Figure 4.30(b)], this catalyst does not behave ideally because C_4/C_{12} is never equal to 1. Further evidence for the non-ideal hydrocracking behaviour of this system is shown by the cracked product distribution profiles in Figure 4.31 below, which favour lighter hydrocarbon products rather than heavier products.

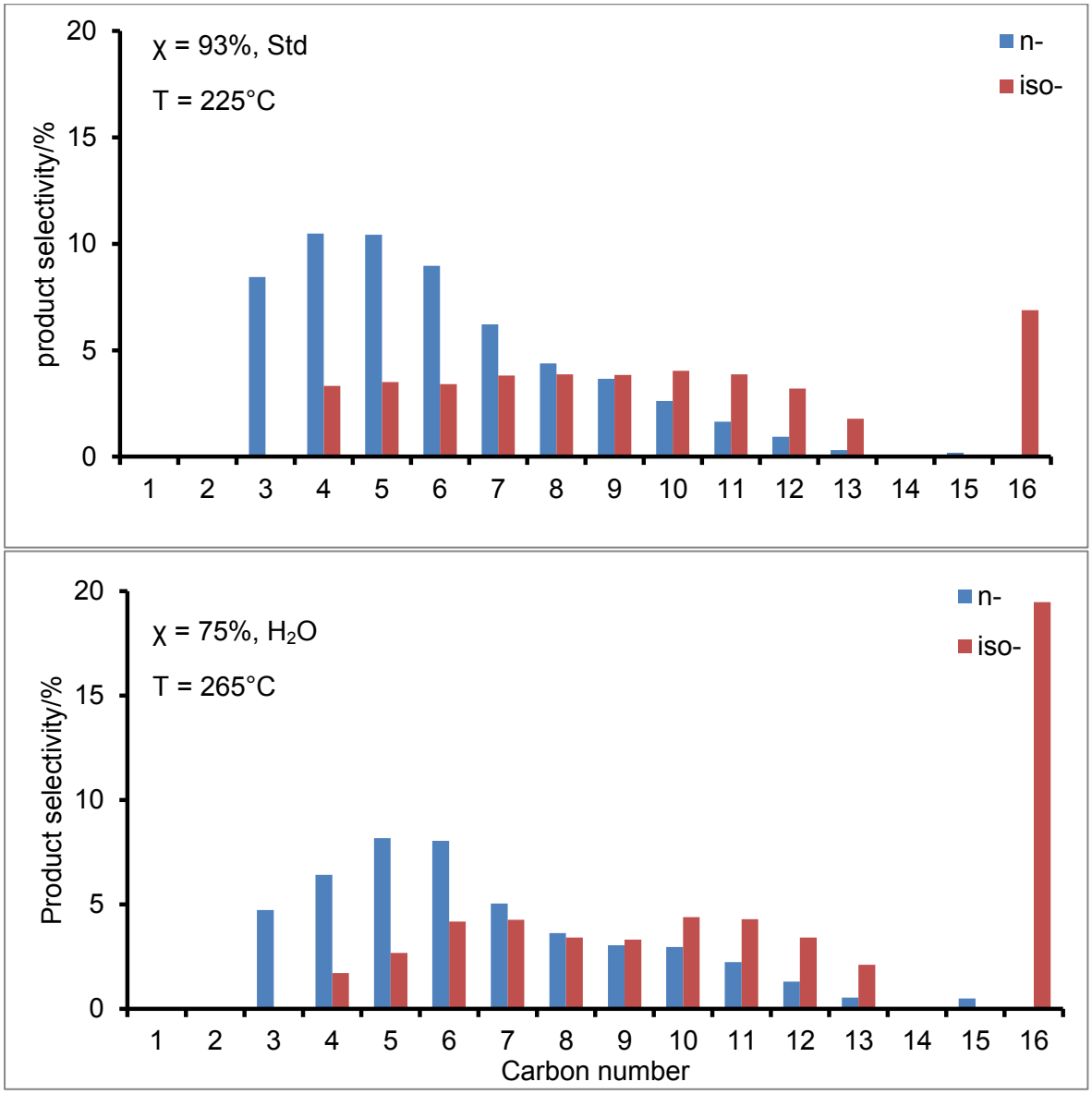

Figure 4.31 The cracked product distributions for standard and non-standard hydrocracking of *n*-C_{16} over the 0.9 wt.% Pd/HSZ(N_4) catalyst.

Also interesting to observe is the isomer content of the product spectrum, which includes the isomerised feed. This isomer content seems to improve upon co-feeding H_2O with *n*-C_{16}. Note the remarkable enhancement of the *iso*-C_{16} selectivity as a consequence of co-feeding H_2O. This observation suggests that these catalyst systems can be further refined or tuned for diesel-selective hydrocracking, with the high *iso*-paraffin content leading to improved cold-flow properties of the fuel. It is also interesting to note that the dominant ≤C_8 *n*-paraffin products undergo a decrease in selectivity when H_2O was co-fed into the hydrocracking reactor together with *n*-C_{16}, culminating in enhanced *iso*-paraffin selectivity.

Figure 4.32 summarises and compares the overall catalytic performance of the above three catalyst systems in their standard runs, by superimposing the corresponding plots [*Figures 4.26(a), 4.28(a) and 4.30(a)*].

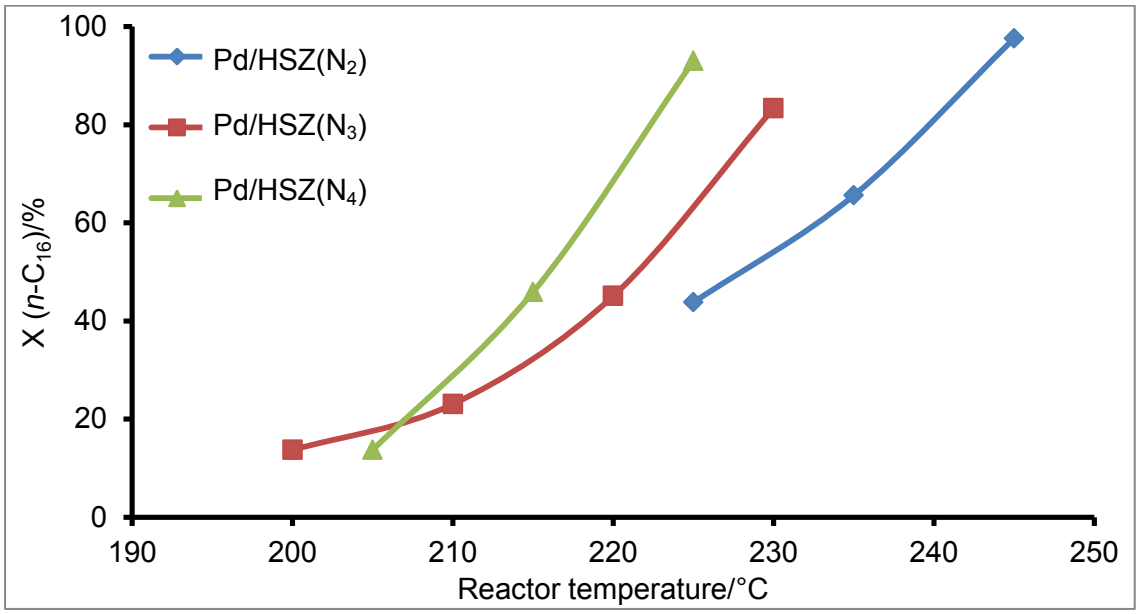

Figure 4.32 Comparison of catalytic performance of three 0.9 wt.% Pd loaded catalyst based on surfactant-templated hierarchical zeolites as acidic supports.

It can be clearly seen from this figure that the 0.9 w t.% Pd/HSZ(N_4) catalyst is most active of the three catalyst systems studied. The catalytic performance of these catalysts follows the order HSZ(N_2) < HSZ(N_3) < HSZ(N_4), in terms of the supports at temperatures above 205 °C. Because the three catalyst supports have the same nominal SAR and consequently solid acidity, the difference in their catalytic performance may be attributed to their different surface areas (*see Table 4.4*), which also follow the same order. This trend suggests that a higher surface area allows a better dispersion of metal particles which is important for catalytic hydrocracking reactions [26]. In terms of the structure of the structure-directing surfactant-template, it can be concluded that the beneficial properties of these hierarchical zeolites depend on the number of quaternary ammonium centres contained in the surfactant template used for synthesis, *i.e.*, the more ammonium centres, the better the catalytic and physicochemical characteristics.

Figure 4.33 shows the catalytic activities of the best performing catalyst systems derived from the bulk and surfactant-templated zeolites.

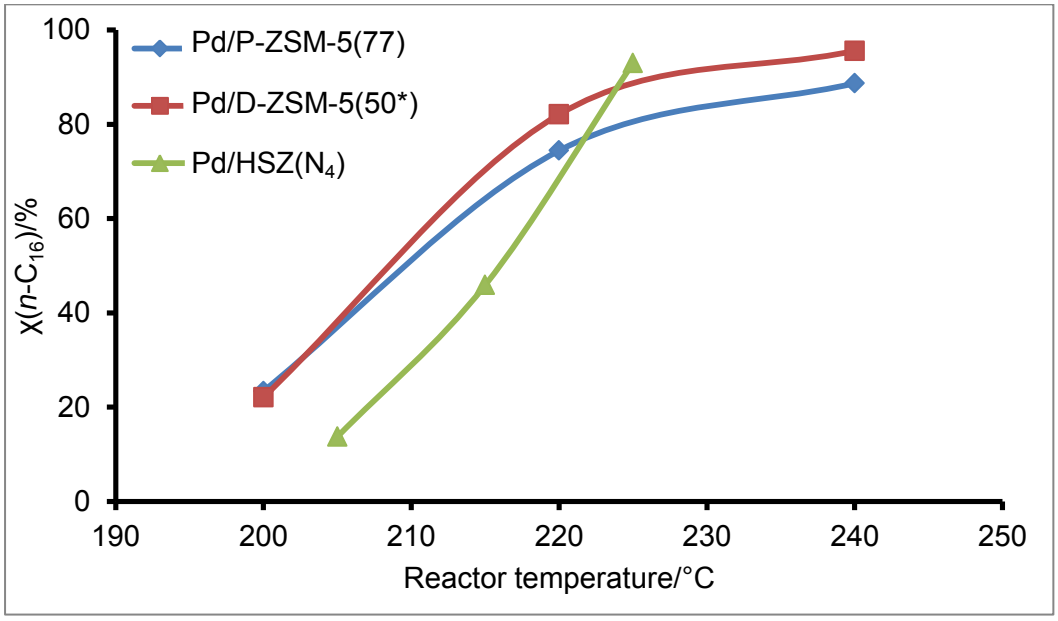

Figure 4.33 Comparison of the catalytic hydrocracking performance of the best performing catalysts from the three series.

The general trend in the catalytic activity is Pd/D-ZSM-5(50*) > Pd/P-ZSM-5(77) > Pd/HSZ(N_4). That is, the bulk and desilicated zeolite-based catalysts perform better than their surfactant-templated zeolite-based counterpart. This is despite the extremely high S_{BET} of the HSZ(N_4)-based zeolite. It is clear that the latter zeolite needs further refinement and fine-tuning in order to achieve acceptable performance as hydrocracking catalyst supports.

4.4 References

[1] K. Na, C. Jo, J. Kim, K. Cho, J. Jung, Y. Seo, R. J. Messinger, B. F. Chmelka, R. Ryoo, Directing zeolite structures into hierarchically nanoporous architectures, *Science*, **333** (2011) 328 - 332.

[2] R. J. Argauer, G. R. Landolt, Crystalline zeolite HSZM-5 and method of preparing the same, US Patent 3702886 (1972).

[3] S. S. Rayalu, J. S. Udhoji, S. U. Meshram, R. R. Naidu, S. Devotta, Estimation of crystallinity in fly ash-based zeolite-A using XRD and IR spectroscopy, *Current Science*, **89** (2005) 2147 - 2151.

[4] P. B. Ramatsetse, Synthesis and characterisation of zeolites ZSM-5 and Ferrierite, PhD thesis, University of Limpopo, South Africa (2003).

[5] N. H. Tamer, Synthesis and characterization of zeolite beta, MSc. Thesis, The Graduate School of Natural and Applied Sciences of Middle East Technical University, Turkey (2006).

[6] S. Octaviani, Y. K. Krisnandi, I. Abdullah, R. Sihombing, The effect of alkaline treatment to the structure of ZSM-5 zeolites, *Makara Journal of Science,* **16** (2012) 155 - 162.

[7] X. S. Zhao, G. Q. Lu, G. J. Millar, Advances in Mesoporous Molecular Sieve MCM-41, *Industrial and Engineering Chemistry Research*, **35** (1996) 2075 - 2090.

[8] B. Liu, C. Li, Y. Ren, Y. Tan, H. Xi, Y. Qian, Direct synthesis of mesoporous ZSM-5 zeolite by a dual-functional surfactant approach, *Chemical Engineering Journal*, **210** (2012) 96 - 102.

[9] G. Coudurier, C. Naccache, J. C. Vedrine, Uses of I.R. spectroscopy in identifying ZSM zeolite structure, *Journal of the Chemical Society*, *Chemical Communications*, (1982) 1413 - 1415.

[10] R. G. Bell, R. A. Jackson C. R. A. Catlow, Löwenstein's rule in zeolite A: A computational study, *Zeolites*, **12** (1992) 870 - 871.

[11] A. R. Ruiz-Salvador, R. Grau-Crespo, A. E. Gray, D. W. Lewis, Aluminium distribution in ZSM-5 revisited: The role of Al-Al interactions, *Journal of Solid State Chemistry*, **198** (2013) 330 - 336.

[12] I. R. Shaikh, R. A. Shaikh, A. A. Shaikh, J. A. War, S. P. Hangirgekar, A. L. Shaikh, P. R. Shaikh, R. R. Shaikh, H-ZSM-5 zeolite synthesis by sourcing

silica from the wheat husk ash: characterization and application as a versatile heterogeneous catalyst in organic transformations including some multicomponent reactions, *Journal of Catalysts*, **2015** (2014) 4 - 5.

[13] J. C. Moreno-Piraján, V. S. Garcia-Cuello, L. Giraldo, Synthesis of HMOR and HZSM-5 and their behaviour in the catalytic conversion of methanol to propylene (MTP), *Journal of Thermodynamics and Catalysis*, **1** (2010) 1 - 9.

[14] P. A. Jacobs, R. von Bellmoos, Framework hydroxyl groups of H-ZSM-5 zeolites, *Journal of Physical Chemistry*, **86** (1982) 3050 - 3052.

[15] E. Van Steen, L. H. Callanan, Recent Advances in the Science and Technology of Zeolites, Part 3, *Studies in surface science and catalysis*, **154** (2004) 2332 - 2333

[16] T. Armaroli, L. J. Simon, M. Digne, T. Montanari, M. Bevilacqua, V. Valtchev, J. Patarin, G. Busca, Effects of crystal size and Si/Al ratio on the surface properties of H-ZSM-5 zeolites, *Applied Catalysis A: General*, **306** (2006) 78 - 84.

[17] M. Guisnet, P. Ayrault, C. Coutanceau, M. F. Alvarez, J. Datka, Acid properties of dealuminated beta zeolites studied by IR spectroscopy, *Journal of the Chemical Society-Faraday Transactions*, **93** (1997) 1661 - 1665.

[18] W. Park, D.Yu, K. Na, K.E. Jelfs, B. Slater, Y. Sakamoto, and R. Ryoo, Hierarchically structure-directing effect of multi-ammonium surfactants for the generation of MFI zeolite nanosheets, *Chemistry of Materials*, **23** (2011) 5131 - 5137.

[19] Y. Tao, H. Kanoh, L. Abrams, K. Kaneko, Mesopore-modified zeolites: preparation, characterization, and applications, *Chemical Review*, **106** (2006) 896 - 910.

[20] G. Leofanti, M. Padovan, G. Tozzola, B. Venturelli, Surface area and pore texture of catalysts, *Catalysis Today*, **41** (1998) 207 - 219.

[21] K. Egeblad, M. Kustova, S. K. Klitgaard, K. Zhu, C. H. Christensen, Mesoporous zeolite and zeotype single crystals synthesized influoride media, Microporous and *Mesoporous Materials*, **101** (2007) 214 - 223.

[22] T. Y. Yan, the effect of water in hydrocracking, *Journal of Catalysis*, **25** (1972) 204 - 211.

[23] C. Ndimande, Ideal Hydrocracking Catalysts for the Conversion of FT wax to diesel, MSc. thesis, University of Cape Town, South Africa (2012).

[24] S. Mehla, Synthesis, characterization and evaluation of zeolites for hydro-isomerization of model feed *n*-hexadecane, MSc. thesis, Indian Institute of Technology - Madras, India (2012)

[25] J. Hancsok, S. Magyar, A. Hollo, Importance of Isoparrafins in the crude oil refining industry, Chemical Engineering Transactions, **11** (2007) 41 - 43

[26] O. A. Larson, D. S. Maciver, H. H. Tobin, Effects of platinum area and surface acidity on hydrocracking activity, *I & EC Process Design and Development,* **4** (1964) 300 - 304

CHAPTER 5

Summary and Conclusions

The aim of this work was to synthesise and characterise hierarchically-structured MFI zeolites, as well as test them for potential use as supports for Pd in the hydrocracking of *n*-hexadecane. Two preparative approaches were used to synthesise multiporous or hierarchical zeolites having an MFI framework topology. One method included a 2-step approach involving prior synthesis of microporous ZSM-5 to three levels of silica-to-alumina ratio (SAR) in the range 50 - 100, under hydrothermal conditions, using tetrapropylammonium bromide as a structure-directing template, followed by a desilication treatment using a dilute aqueous solution of NaOH. The second method involved prior synthesis of Gemini or polyquaternary ammonium surfactants through synthetic organic chemistry approaches, followed by the use of these surfactants as templates in the direct one-pot synthesis of hierarchical MFI zeolites containing both micropores and mesopores in the same matrix. Successful synthesis of these different classes of MFI zeolites was immediately confirmed by XRD patterns, while successful synthesis of polyquaternary ammonium surfactants was confirmed by their ^{1}H NMR spectra, as well as their ability to direct the production of the expected MFI structures (as confirmed by XRD).

For the conventional microporous zeolites, the % XRD crystallinity was found to increase with the SAR in their pristine state, with a similar trend observed for their desilicated counterparts. There was also a gradual decrease in average crystallite size for the pristine materials, while the crystallite sizes of their desilicated counterparts remained constant within experimental error. The scanning electron micrographs of conventional ZSM-5 showed well-defined shapes only at SAR of 50, while other SARs exhibited agglomerated particles. Strangely, the IR spectra of all pristine ZSM-5 only showed bands in the framework region, and nothing in the hydroxyl (OH) region. This may suggest the absence or diminished Brønsted acid

sites in the pristine zeolites, although the hydrocracking results proved otherwise. However, upon alkaline treatment these materials developed two reasonably-intense OH peaks at ~3600 and 3730 cm^{-1}. Therefore, desilication enhanced Brønsted acidity of these materials (*in addition to minor structural readjustments evidenced by slight shifts in XRD peak positions*). Nitrogen adsorption isotherms confirmed the introduction of mesopores in the intrinsically-microporous zeolites by the desilication treatment, as demonstrated by two-step adsorption isotherms with hysteresis. Another piece of evidence of mesoporosity is provided by the BET surface area and porosity data in Table 4.3, which improved remarkably in response to desilication. The catalytic performance of the pristine zeolite-based catalysts followed the order Pd/P-ZSM-5(77) > Pd/P-ZSM-5(100) > Pd/P-ZSM-5(50). That is, catalysts based on high SAR supports (*i.e*., >50) showed high catalytic performance, though SAR = 100 showed inferior performance compared to SAR = 77, suggesting the optimum SAR to lie around 77. In contrast, the catalytic activity of the catalysts derived from desilicated supports improved systematically with a decrease in SAR of the support in the order Pd/D-ZSM-5(50*) > Pd/D-ZSM-5(77*) > Pd/D-ZSM-5(100*). It is interesting to observe the superior catalytic performance of the catalysts based on the zeolite with SAR of 50*, since it was the most inferior in its pristine form. This shows that the induced Brønsted acidity, newly-introduced mesopores, and increased surface area resulting from desilication, played a major role in the catalytic hydrocracking performance of the desilicated zeolite-derived catalysts. Another observation from both pristine and desilicated supports is that the most crystalline materials are actually not the best.

The % XRD crystallinity of the surfactant-templated zeolites, increased in order of the number of quaternary ammonium centres contained in each template, *i.e*., 3 > 4 > 2. These zeolites were generally more crystalline than conventional ZSM-5 materials [*all of which were referenced using P-ZSM-5(100)*]. This was suggested to be due to longer crystallisation period used for these zeolite materials, in addition to the presence of multiple zeolite structure-directing quaternary ammonium groups in surfactant templates. Their crystallite sizes also increased as the number of quaternary ammonium centres in the surfactants increased. A spectacular feature was observed in the use of 18-N_4-18 surfactant as template, which produced an MFI-type zeolite whose XRD pattern included a prominent (100) peak, signalling the

presence of mesoporosity by analogy with MCM-41. However, this feature was absent in zeolites synthesised with 18-N_2 and 18-N_3-18 surfactant templates.

The highly intense hydroxyl peaks in IR spectra between 3500 and 3800 cm^{-1} suggest the presence of a high content of Brønsted acid sites in these materials. The SEM images of these hierarchical zeolites showed irregular morphologies with varied shapes. The micrograph of the hierarchical zeolite synthesised using 18-N_2 as SDA showed a morphology consisting of smaller particles attached to the surface of a larger particle with a mixture of spheroidal, cubic, rectangular and prismic shapes. When 18-N_3-18 was used as SDA in place of 18-N_2, the material exhibited a highly irregular morphology with lumps of closely packed crystals, including hexagonal prisms and some flat slabs. The micrograph of 18-N_4-18 surfactant-templated zeolite showed plate-like and irregular micrometre-sized crystals. The presence of dual porosity in the three surfactant-templated zeolites was confirmed by Type IV isotherms. It was also observed that increasing the number of quaternary ammonium centres in the surfactant template was accompanied by increased BET surface area, pore volume and pore diameter of the resulting zeolite.

The catalytic performance of the catalysts based on surfactant-templated supports followed the order Pd/HSZ(N_2) < Pd/HSZ(N_3) < Pd/HSZ(N_4). Because the three catalyst supports have the same nominal SAR, and consequently the same solid acidity, the difference in their catalytic performance may be attributed to their different BET surface areas, which also follow the same order of ammonium content. In terms of the framework composition of the structure-directing surfactant-templates, the beneficial properties of these hierarchical zeolites correlated with the number of quaternary ammonium centres contained in the surfactant template used for synthesis, *i.e*., the higher the number of ammonium centres, the better the catalytic and physicochemical characteristics.

The standard runs for the catalytic tests of the three series of zeolites (*pristine zeolite-based, desilicated zeolite-based and surfactant-templated zeolites-based*), exhibited secondary cracking, evidenced by $C_4/C_{12} \neq 1$. This was also supported by the corresponding product distribution profiles, which showed dominant C_3 - C_7 *n*-paraffins in the product stream. The co-feeding of H_2O with *n*-C_{16} into the reactor was detrimental to the *n*-C_{16} conversion, but decreased the selectivity towards the

undesired lower carbon number products (C_3 - C_7). On the other hand, H_2O was also observed to promote the selectivity to *iso*-paraffins in the product spectrum, which is a desired feature for the production of the diesel with improved cold-flow properties. Simultaneous co-feeding of H_2O and CO into the reactor aggravated secondary cracking.

Amongst the pristine ZSM-5 zeolite-based catalysts, Pd/P-ZSM-5(77) showed the best catalytic performance. Upon desilication, the performance order changed to favour Pd/D-ZSM-5(50*). For the surfactant-templated supports, Pd/HSZ(N_4) showed the most superior hydrocracking performance. Comparison of catalytic activities of the best-performing catalyst systems derived from the bulk and surfactant-templated zeolites follow the order Pd/D-ZSM-5(50*) > Pd/P-ZSM-5(77) > Pd/HSZ(N_4). That is, the pristine and desilicated zeolite-based catalysts perform better than their surfactant-templated zeolite-based counterpart. This is despite the extremely high S_{BET} of the HSZ(N_4)-based zeolite support in this catalyst. It is clear that the latter zeolite needs further refinements to achieve acceptable performance as hydrocracking catalyst support. In summary, the three best best-performing catalysts are potential candidates for diesel-selective catalysis and require further refinements.

Recommendations

Further studies will be required to improve the three catalysts namely, Pd/P-ZSM-5(77), Pd/D-ZSM-5(50*) and Pd/HSZ(N_4). These catalysts showed potential in the hydrocracking of *n*-hexadecane, although secondary cracking was a challenge. In order to curb secondary cracking occurring over these catalysts the following readjustments or modifications need to be considered:

(i) Preparation of Pd/P-ZSM-5(77) and Pd/D-ZSM-5(50*) catalysts at Pd loadings >0.9 wt.% in order to obtain the enhanced metal-to-acid site balance to achieve ideal hydrocracking.
(ii) Dealuminate P-ZSM-5(77) and HSZ(N_4) catalyst supports in order to fine-tune their acidity and obtain the viable SAR for ideal hydrocracking, or synthesise HSZ(N_4) support at higher SARs, *i.e.*, > 40. This will help reduce the total acidity of the support that causes secondary cracking.

It will be important to characterise the resulting catalysts in order to rationalise the catalytic performances in relation to their physicochemical properties (*note that only supports were characterised in this work*).

APPENDICES

The raw data from the results are appended in this section.

A1: The NMR spectrum of 18-N2

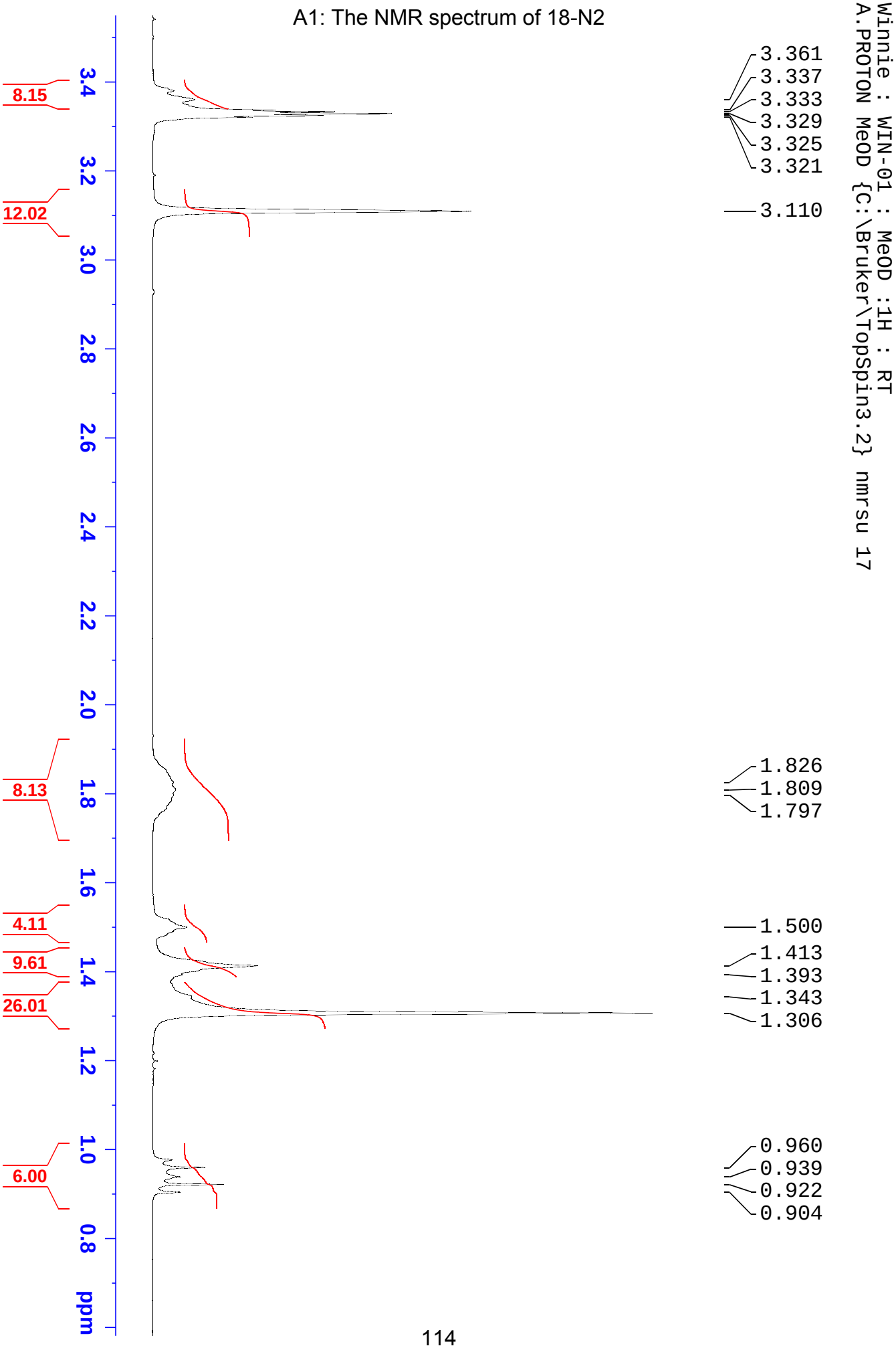

A2: The NMR spectrum of 18-N3-18

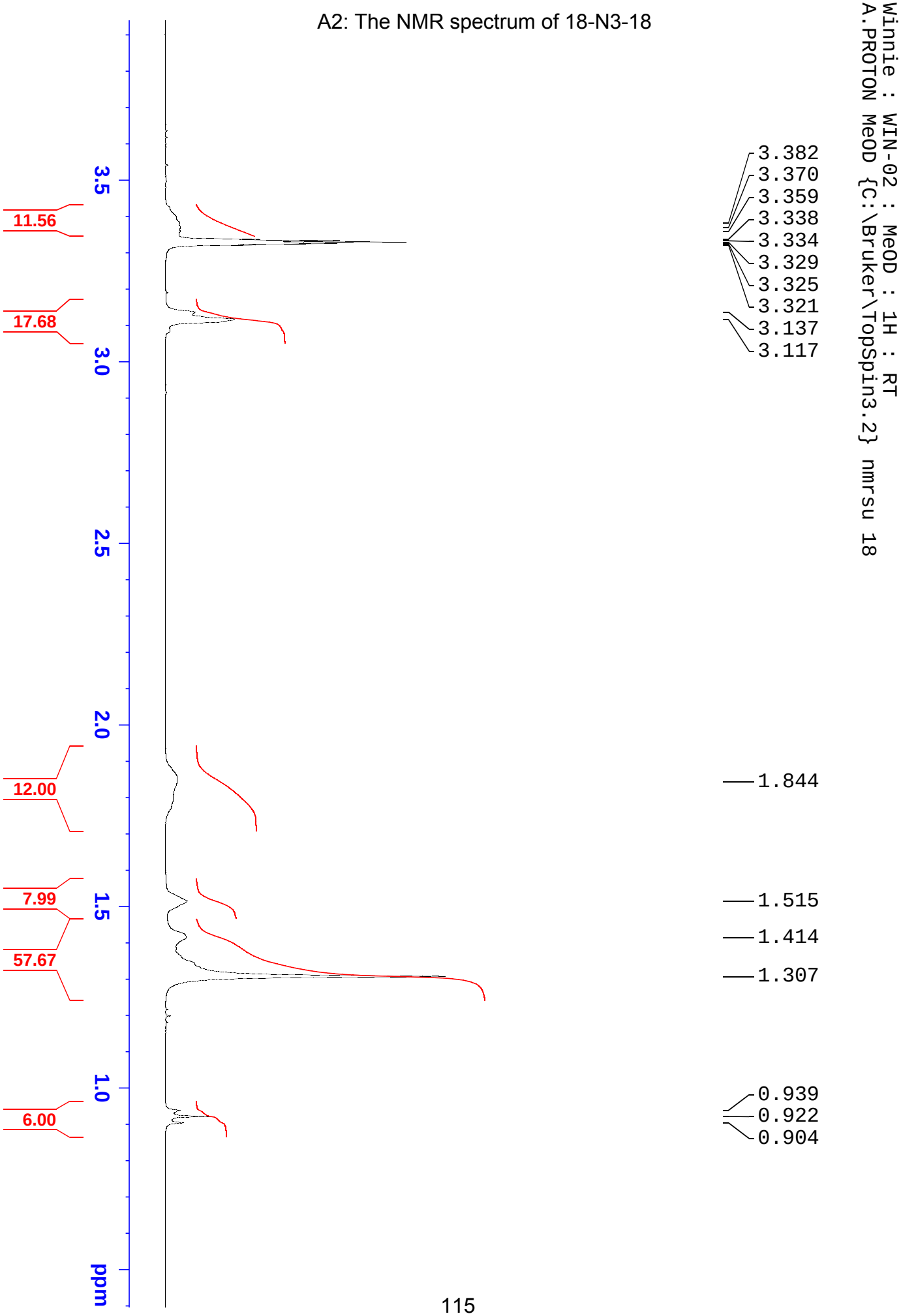

A3: The NMR spectrum of 18-N4-18

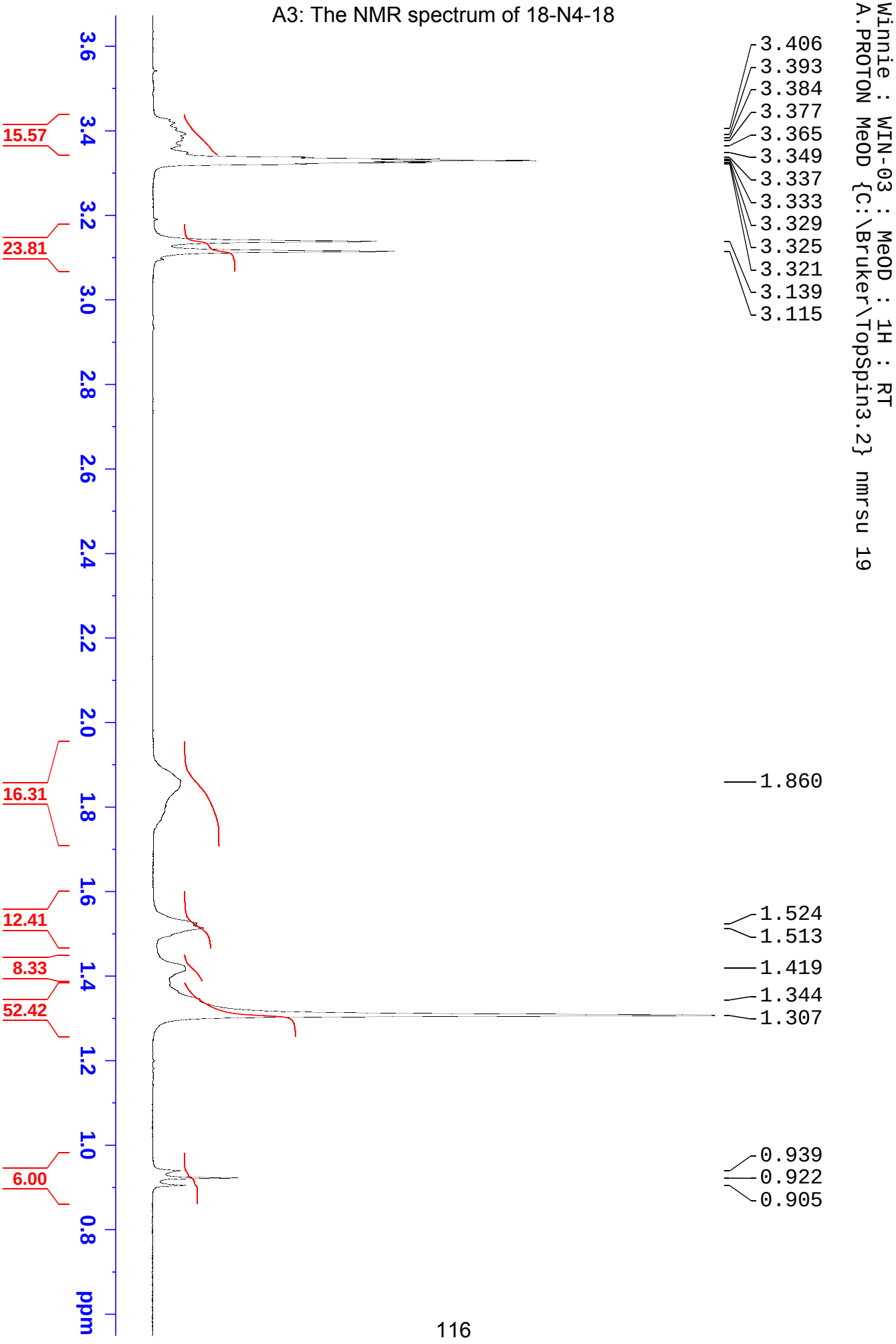

A4: Influence of desilication on peak positions of the MFI XRD characteristics peaks

Pristine zeolites					
	Characteristic peak indices (Miller)				
SAR	**(101)**	**(020)**	**(332)**	**(033)**	**(313)**
50	9.83	10.32	27.00	27.43	28.00
77	9.72	10.32	27.20	27. 80	28.01
100	9.46	10.11	26.87	27.40	27.81
Desilicated zeolites					
50*	9.74	10.29	26.90	27.19	27.86
77*	9.66	10.27	26.81	27.00	27.60
100*	9.59	10.28	26.81	27.03	27.62